

EXPERIMENTAL INVESTIGATION INTO THE AERODYNAMICS OF  
SMALL AIR VEHICLES WITH THIN FLEXIBLE WINGS

by

TIMOTHY CRAIG WITUSHYNSKY

Submitted in partial fulfillment of the requirements

For the degree of Master in Science

Thesis Advisor: Dr. Roger Quinn

Department of Mechanical & Aerospace Engineering

CASE WESTERN RESERVE UNIVERSITY

August, 2008

**CASE WESTERN RESERVE UNIVERSITY**

**SCHOOL OF GRADUATE STUDIES**

We hereby approve the thesis/dissertation of

\_\_\_\_\_ Tim Witushynsky \_\_\_\_\_

candidate for the \_\_\_\_\_ Masters \_\_\_\_\_ degree \*.

(signed) \_\_\_\_\_ Dr. Roger Quinn \_\_\_\_\_  
(chair of the committee)

\_\_\_\_\_ Dr. Iwan Alexander \_\_\_\_\_

\_\_\_\_\_ Dr. Yasuhiro Kamotani \_\_\_\_\_

\_\_\_\_\_

\_\_\_\_\_

\_\_\_\_\_

(date) \_\_\_\_\_ 05/15/08 \_\_\_\_\_

\*We also certify that written approval has been obtained for any proprietary material contained therein.

## TABLE OF CONTENTS

|  |    |
|--|----|
| Table of Contents.....                   | 1  |
| List of Tables.....                      | 5  |
| List of Figures.....                     | 6  |
| List of Abbreviations.....               | 9  |
| Abstract.....                            | 10 |
| Chapter 1 - Introduction.....            | 11 |
| 1.1    General.....                      | 11 |
| 1.2    Goals of Thesis.....              | 13 |
| 1.3    Thesis Outline.....               | 14 |
| Chapter 2 - Background Research .....    | 16 |
| 2.1    General.....                      | 16 |
| 2.2    UAV Technology.....               | 18 |
| 2.2.1    Predator.....                   | 18 |
| 2.2.2    Silver Fox.....                 | 18 |
| 2.3    MAV Technology.....               | 19 |
| 2.3.1    Black Widow.....                | 19 |
| 2.3.2    Microbat.....                   | 20 |
| 2.3.3    UF MAV Development.....         | 21 |
| 2.4    Balance Systems.....              | 22 |
| 2.5    MAV Wind Tunnel Testing.....      | 24 |
| Chapter 3 – Design and Fabrication ..... | 29 |
| 3.1    General.....                      | 29 |

|                                  |   |    |
|----------------------------------|---|----|
| 3.2                              | Wing and Aircraft Designs.....          | 29 |
| 3.3                              | Sting Design.....                       | 33 |
| 3.4                              | Adapter Designs.....                    | 36 |
| 3.5                              | Camera Mount.....                       | 37 |
| Chapter 4 – Testing Methods..... |   | 40 |
| 4.1                              | General.....                            | 40 |
| 4.2                              | Balance Calibration and Coupling.....   | 40 |
| 4.3                              | Initial Testing.....                    | 43 |
| 4.4                              | Sting Modifications.....                | 44 |
| 4.4.1                            | Rubber Inserts.....                     | 45 |
| 4.4.2                            | Damper.....                             | 45 |
| 4.5                              | Dashpot Testing.....                    | 47 |
| 4.6                              | Wing Curvature Testing.....             | 49 |
| 4.6.1                            | Image Analysis Technique 1.....         | 50 |
| 4.6.2                            | Image Analysis Technique 2.....         | 51 |
| 4.6.3                            | Image Analysis Technique 3.....         | 52 |
| 4.7                              | Picture Testing Methods.....            | 55 |
| 4.7.1                            | Black Light Testing.....                | 55 |
| 4.7.2                            | Ambient Light, Perspective Testing..... | 56 |
| 4.8                              | Final Experimental Procedure.....       | 58 |
| Chapter 5 – Data Analysis.....   |   | 60 |
| 5.1                              | Tested Wings and Aircraft.....          | 60 |
| 5.2                              | Data Analysis: Matlab Conversions.....  | 61 |

|  |   |    |
|--|---|----|
| 5.3                                      | Data Coefficients.....                            | 63 |
| 5.4                                      | Flat Plate Testing.....                           | 66 |
| Chapter 6 – Error Analysis.....          |   | 68 |
| 6.1                                      | General.....                                      | 68 |
| 6.2                                      | Instrumentation Errors.....                       | 68 |
| 6.3                                      | Data Coefficient Errors.....                      | 70 |
| 6.4                                      | Angle of Attack Errors.....                       | 74 |
| 6.5                                      | Error Results and Contributions.....              | 75 |
| Chapter 7 – Discussion.....              |   | 79 |
| 7.1                                      | General Results.....                              | 79 |
| 7.2                                      | Drag Comparison: Wing and Aircraft.....           | 80 |
| 7.3                                      | Video Analysis: UF Data.....                      | 81 |
| 7.4                                      | Select Coefficient of Lift versus Alpha Data..... | 88 |
| 7.5                                      | Sting and Adapter Deflections.....                | 90 |
| 7.6                                      | Electronics.....                                  | 91 |
| 7.7                                      | Equation Fits for Results.....                    | 92 |
| Chapter 8 – Conclusion.....              |   | 95 |
| 8.1                                      | General.....                                      | 95 |
| 8.2                                      | Highlighted Results.....                          | 96 |
| Chapter 9 – Future Work.....             |   | 97 |
| 9.1                                      | Sting and Testing Considerations.....             | 97 |
| Appendices.....                          |   | 99 |
| Appendix A – Wing and Aircraft Data..... |   | 99 |

|                                       |     |
|---------------------------------------|-----|
| Appendix B – Error Analysis Data..... | 109 |
| Appendix C – Matlab Code.....         | 113 |
| Appendix D – Technical Drawings.....  | 122 |
| Appendix E – Equations.....           | 126 |
| Appendix F – Wing Pictures.....       | 130 |
| References.....                       | 132 |

## LIST OF TABLES

|           |  |    |
|-----------|--|----|
| Table 5.1 | Wing and aircraft designations.....                            | 61 |
| Table 5.2 | Sting flow effects.....  | 63 |
| Table 6.1 | Pressure change versus tested velocity.....                    | 69 |
| Table 7.1 | Instrumentation specifications.....                            | 92 |
| Table 7.2 | Linear equation fits for lift and parabolic fits for drag..... | 94 |
| Table 7.3 | Parabolic equation fits for lift coefficient.....              | 94 |

## LIST OF FIGURES

|            |   |    |
|------------|---|----|
| Figure 1.1 | Gust load on flexible wing.....           | 12 |
| Figure 2.1 | Reynolds number for various aircraft..... | 17 |
| Figure 2.2 | Black Widow MAV.....                      | 20 |
| Figure 2.3 | UF 6 inch MAV.....                        | 22 |
| Figure 2.4 | Notre Dame MAV data.....                  | 25 |
| Figure 2.5 | UF 6 inch MAV data.....                   | 26 |
| Figure 2.6 | University of Arizona MAV data.....       | 26 |
| Figure 3.1 | Tested wing planforms.....                | 31 |
| Figure 3.2 | Elliptical thin wing design.....          | 31 |
| Figure 3.3 | MAV fuselage & tail sections.....         | 33 |
| Figure 3.4 | Sting apparatus.....                      | 35 |
| Figure 3.5 | Sting lift deflection.....                | 36 |
| Figure 3.6 | Sample sting adapter pieces.....          | 37 |
| Figure 3.7 | Camera mount SolidWorks design.....       | 38 |
| Figure 3.8 | Camera mounting wind tunnel position..... | 39 |
| Figure 4.1 | Sting strain gauge placement.....         | 40 |
| Figure 4.2 | Sting calibration orientations.....       | 41 |
| Figure 4.3 | Final test apparatus.....                 | 47 |
| Figure 4.4 | Dashpot testing results.....              | 49 |
| Figure 4.5 | Wing section test piece.....              | 52 |
| Figure 4.6 | Wing curvature image analysis.....        | 54 |
| Figure 4.7 | SolidWorks perspective view testing.....  | 58 |

|            |  |    |
|------------|--|----|
| Figure 5.1 | Force body diagram for wing.....                         | 62 |
| Figure 5.2 | Designated Wing 4 lift coefficient versus AoA.....       | 64 |
| Figure 5.3 | Assembled CW0 designated MAV.....                        | 65 |
| Figure 5.4 | Designated aircraft BW0 lift coefficient versus AoA..... | 66 |
| Figure 5.5 | Flate Plate lift coefficient versus AoA.....             | 67 |
| Figure 6.1 | Centered wing on apparatus.....                          | 77 |
| Figure 6.2 | Offset wing on apparatus.....                            | 77 |
| Figure 6.3 | Yawed wing on apparatus.....                             | 78 |
| Figure 7.1 | Drag comparison: wing & aircraft.....                    | 80 |
| Figure 7.2 | Designated Wing 2 drag coefficient versus AoA.....       | 83 |
| Figure 7.3 | Video analysis: wing thread attachment.....              | 84 |
| Figure 7.4 | Video analysis: visualization of flow over UF wing.....  | 85 |
| Figure 7.5 | Laminar Separation Bubble.....                           | 88 |
| Figure 7.6 | Drag equation fit to designated Wing 0.....              | 93 |

## Acknowledgements

To my parents for taking me to a local airport to watch planes take off and land when I was young. Also for those legos, eventually leading me to engineering.

Dr. Roger Quinn for allowance and introduction to the Biologically Inspired Robotics Laboratory and support throughout my time in the lab. Also for that wonderful trip to Switzerland (A country that I may never be allowed to return to).

Richard Bachmann for support in many engineering projects and introduction to the machine shop.

Dr. Edward White for allowance to use the Case Western Reserve University graduate low speed wind tunnel.

Jim Berilla for insight to balance design and assistance in balance construction and assembly.

Brian Taylor for engineering insight and introduction to many papers on MAV technologies.

Biorobotics Lab for their support and good humor, or at least putting up with me.

## LIST OF ABBREVIATIONS

|      |                           |
|------|---------------------------|
| AoA  | Angle of Attack           |
| LE   | Leading Edge              |
| TE   | Trailing Edge             |
| AR   | Aspect Ratio              |
| HAR  | High Aspect Ratio         |
| LAR  | Low Aspect Ratio          |
| UF   | University of Florida     |
| PTFE | Polytetrafluoroethylene   |
| MAV  | Micro Air Vehicle         |
| UAV  | Unmanned Aircraft Vehicle |

# Experimental Investigation into the Aerodynamics of Small Air Vehicles with Thin Flexible Wings

Abstract

by

TIMOTHY CRAIG WITUSHYNSKY

Unmanned aircraft vehicles have inspired the creation of smaller, lighter aircraft, capable of the same mission requirements. To aid these micro air vehicles in maintaining a stable flight, a flexible fabric is used on the wing to absorb gust loads and provide passive adaptive washout. While these features are desirable for longer, more stable flights, a performance evaluation would provide information for an improved micro air vehicle platform. This inspired the testing of thin wings, and aircraft to determine the aerodynamic characteristics of lift, drag and aerodynamic pitching moment, and then evaluate the options for improving aircraft performance. This thesis describes the designs and methods used to capture these characteristics, quantifies the data and error in the setup, and evaluates the best options for a micro air vehicle based upon the wings and aircraft tested.

# CHAPTER I

## INTRODUCTION

### 1.1 General

Micro air vehicles are defined as 15 cm. wing span, 25 mph maximum speed aircraft by DARPA (Waszak et al 2001). These aircraft have received much attention in recent years for several reasons. They are small and therefore virtually undetectable, lightweight, and relatively inexpensive, depending on the included sensors and systems onboard. The typical Reynolds numbers to which they operate in flight are  $10^4$  to  $10^5$ , seen as a transition range for flight mechanics and aerodynamics in general (Nechyba and Ifju 2002). In this region of Reynolds numbers birds and insects rely more upon wing flapping and warping, to maintain stable flight (Mueller 1999; Ifju et al. 2002). It is necessary then that MAVs have a way of coping with this transition region for maintaining flight.

There are many existing UAVs that are capable of aerial surveillance, sensing, and tracking from high altitudes. Although these aircraft have a longer maximum flight duration, they require some base or airfield to which they must takeoff and land on. A strong point for a MAV is that it may be hand launched for brief and rapid reconnaissance missions through difficult terrains. They will still be able to provide the same information for surveillance, chemical detection, or otherwise specified missions. Unlike a larger UAV, a MAV may be more expendable due to low cost requirements.

As the Reynolds number for typical flight operation is lower than that of most aircraft, this makes the aircraft more difficult to control, especially in adverse weather

conditions. In order to add some passive stability to a micro air vehicle, flexible membrane wings are used, taken from the biological inspiration of bats, insects, and other animals (Mueller 1999; Ifju et al. 2002). These animals employ their flexible membrane wings to avoid stalling through passive angle of attack reductions, reach higher angles of attack, and adapt to gust loads for a more stable flight. In addition, the flexible wing allows for passive adaptive washout from gust loads, reducing the induced drag on the wing (Waszak et al 2001). A change in the velocity from the gust would further deform the wing such that the total lift would not change as much as on a rigid wing.

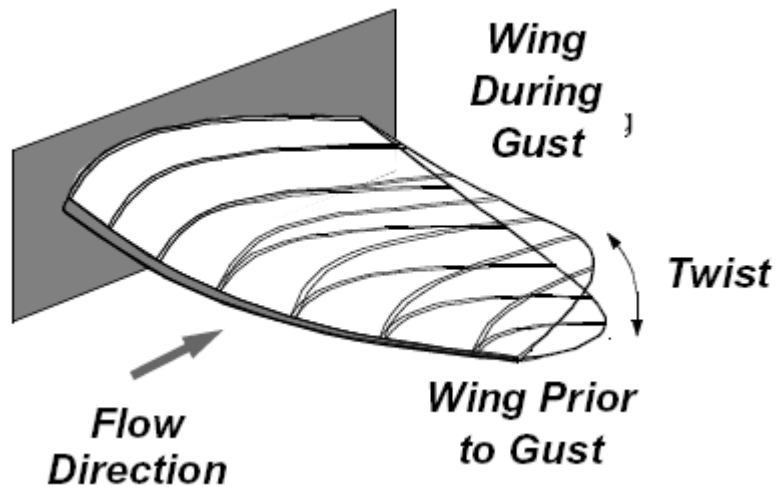


Figure 1.1 – Change in angle of attack on flexible wing due to gust load (Nechyba and Ifju 2002)

As the flight velocities for micro air vehicles are on the same order of magnitude as some gusts, the flexible wing is almost essential for a MAV to adapt to various weather conditions. They were thus used for the current MAV technologies at Case Western Reserve University based on the University of Florida (UF) (Ifju et al. 2002) construction, using pre-impregnated carbon fiber rigid structures built around a flexible membrane.

As the fuselage structure was changed based upon the systems and sensors required for missions, an experimental evaluation of the flexible wings was needed in order to improve upon the aerodynamic performance of the developed MAV platforms.

## 1.2 Thesis Goals

An experimental aerodynamic analysis for micro air vehicles is important for the purpose of evaluating the vehicle performance in order to enhance its capabilities. MAV mission requirements will change depending upon location and environment, stipulating varying payloads and systems on the vehicle. The included systems may be GPS and autopilot systems for autonomous control, a wing folding mechanism, or a ground mobility system, among others (Waszak et al 2001). With a performance evaluation of the wings and aircraft, MAVs may be optimized as per mission requirements. In conjunction with the optimization of the missions, the basic aircraft components may be changed for improved flight duration and mobility.

The goals for this project include the design and construction of an experimental apparatus capable of recording two dimensional aerodynamic characteristics for both thin, flexible wings, and micro air vehicles. Flexible wings with varying planforms were to be tested and comparisons drawn to a thin flat plate. The best wing aerodynamic performances would subsequently be tested on several MAV platforms for a final evaluation. The full scope of this thesis is to provide insight into improving the MAV platform aerodynamically through flexible wing selection.

Although the small air vehicles developed at Case Western Reserve University are larger than the DARPA MAV specification, they are referred to as Micro Air

Vehicles for consistency and because they fall into the category of low Reynolds number aerodynamics.

### 1.3 Chapter Topics

Chapter one, this chapter, introduces the inspiration for micro air vehicles and testing for improved performance. It highlights some of the unique capabilities of the aircraft, including low Reynolds number flight and gust load reduction via flexible wing technology.

Chapter two reviews the existing literature of apparatus' and testing setups for MAV platforms as well as the aerodynamic performances of flexible wing aircraft from low speed wind tunnel testing. It discusses the development of unmanned aircraft vehicles in general as well as recent micro air vehicles. This chapter also reviews low Reynolds number aircraft with other aircraft and flying animals for aerodynamic comparison.

Chapter three develops and reviews the designs and manufacturing for the main sting apparatus as well as other setups required for the experiments. This includes the flexible wings and micro air vehicles tested, and a camera mount for qualitative flow analysis. The method for angle of attack change of the flexible wing or MAV was also developed and manufactured.

Chapter four discusses the methods used for all data collection, image analysis, and experimental procedures. It reviews the calibration for the balance system and initial testing of flexible wings. This chapter discusses the problems with the experimental setup and how they were overcome.

Chapter five introduces the methods for data analysis and examines the core results for lift, drag, and moment characteristics. It develops the equations for the coefficients of lift, drag, and moment for data comparisons at all tested velocities. This chapter also shows some problematic data that is discussed in chapter seven.

Chapter six develops the methods used for error analysis, discusses the ramifications thereof, and compares the differences between all data. This chapter analyzes the primary factors in the error and suggests areas of improvement for the experimental setup. It shows more problematic data that is discussed and solved for in chapter seven.

Chapter seven discusses the results of the completed data collection. It solves the data in question through qualitative flow analysis and review of theoretical bases. This chapter also develops equation fits of the data in order to provide analytical functions for micro air vehicle redesigns.

Chapter eight draws conclusions from the results and recommends the best performing wings and aircraft that were tested. This provides insight to the current flexible wing designs and a basis for further testing.

Chapter nine suggests future work for changes in the apparatus and methods of data collection for better quality, and more advanced data. The material selection and overall dimensions are discussed for a better evaluation of the balance system. A new method for automatic angle of attack adjustment is also discussed for a faster data collection process.

## CHAPTER II

### BACKGROUND RESEARCH

#### 2.1 General

Before conducting testing of flexible wing and MAV platforms a literature survey was done to gain an understanding of current UAV and MAV technologies, capabilities, and previous testing. Many currently existing MAVs have relatively short flights, anywhere from several minutes to an hour (Morris 2002; Torres and Mueller 2000), as well as little to no payload capacities for other onboard sensors and equipment. A certain barrier for these aircraft is the inherent aerodynamic instability, due to the small size, creating a challenge for controlled flight.

As all these features are desired on a MAV, there were several improvements to be considered. A lightweight aircraft will aid in the payload capacity and duration of flight for a MAV, however the drawback is a low moment of inertia, adding to the aerodynamic instability of the vehicle (Waszak et al 2001). The flexible wing will aid in maintaining the stability of the aircraft by reducing the apparent angle of attack, however in some cases large angles of attack are required for the necessary lift for steady flight (Waszak et al 2001; Ifju et al. 2002). At these extremes, the vehicle drag is much higher than desired, requiring more power from an onboard battery and decreasing the maximum flight duration.

In light of a MAVs' apparent aerodynamic instability, comparisons have been drawn between MAV technologies, flying animals, and larger aircraft, showing the Reynolds number at which flight is achieved (See figure 2.1).

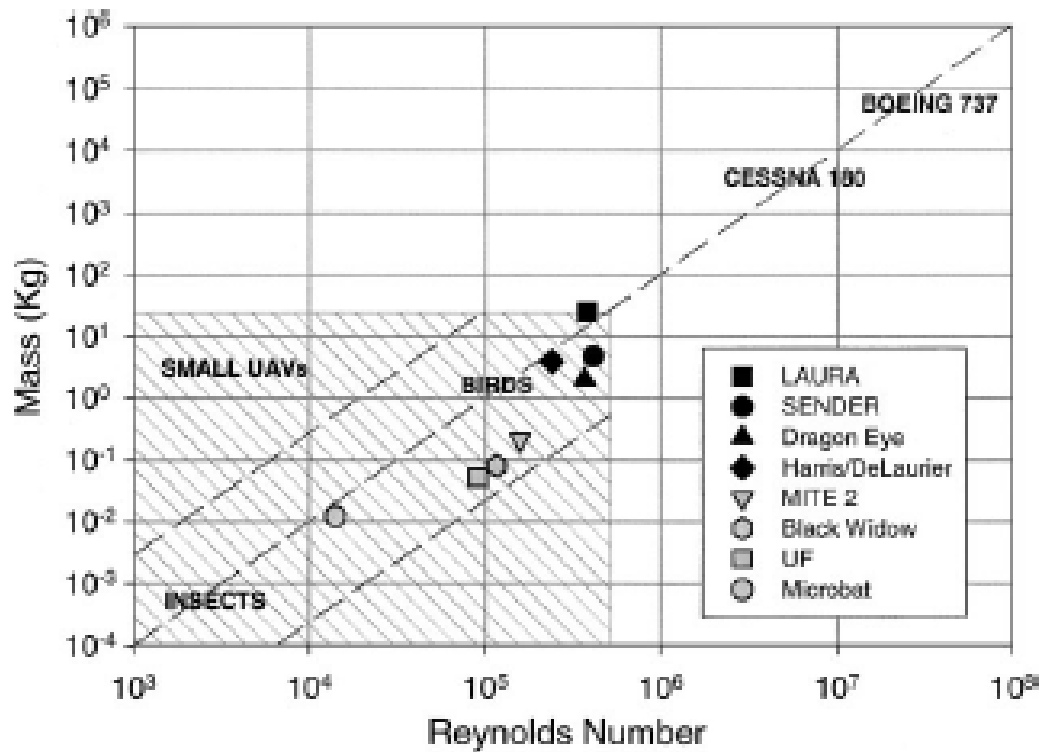


Figure 2.1 – Mass vs. Reynolds Number for various aircraft and flying animals (Mueller and DeLaurier 2003)

This graph shows that most MAVs will fall into a region where flight is achieved by many animals by gliding and flapping their chord-wise compliant wings (Mueller 1999; Ifju et al. 2002). For this reason even propeller driven MAVs employ the use of flexible membrane wings for passive stability and control during flight, adapting to gust loads and stalling effects.

In this chapter, several UAVs and MAVs are explored for their desired capabilities and construction methods. These features will provide insight to improving the aerodynamic performance of current MAV platforms.

## 2.2 UAV Technology

In several ways UAVs were the first step to developing MAVs. These aircraft have been used since the 1940's (Morris 2002) and with the development of GPS systems in the 1980's they were capable of autonomous control, flight durations of up to several days, and gathering vital information through sensors and other onboard equipment. Two of the better known UAVs currently used are General Atomics Aeronautical Systems' Predators (General Atomics 2008) and Advanced Ceramic Researches' Silver Fox (A. Ceramics Research 2006).

### 2.2.1 Predator

The Predator was first developed in 1994 and has since been used for target acquisition and reconnaissance among other missions (General Atomics 2008). Both Predators A and B have maximum flight durations of at least 30 hours, and maximum payload capacities of 500 and 3000 lbs (230-1360 kg.), respectively. These aircraft have typical flight velocities of 240 knots (275 mph), are 32 feet long (9.75 m.) with 64 feet (19.5 m.) wing spans, and weigh up to 6400 lbs (2900 kg.). Although not on the same scale, the long flight durations and high payload capacities are desirable features for MAV platforms.

### 2.2.2 Silver Fox

The Silver Fox, developed by Advanced Ceramics Research, is a lighter and smaller UAV capable of being launched from a catapult system (A. Ceramics Research

2006). This aircraft has a typical flight speed of 55 knots (65 mph), weighs 26 lbs (12 kg.), and has a payload capacity of 5 lbs (2.3 kg.). It has a wingspan of 94 inches (2.4 m.) and is 58 inches long (1.5 m.). Although the payload capacity percentage is not as high as the predator, one greatly desired feature is the catapult launching system; all MAVs require no runway and very little space to reach a desired altitude, as they are all hand launched. The Silver Fox is able to achieve this as well as maintain flights up to 8-10 hours for surveillance missions.

## 2.3 MAV Technology

In recent years smaller UAVs called micro aerial vehicles or MAVs have been developed for similar purposes as that of the larger aircraft, providing surveillance and data through autonomous control. This has been made possible due to the development of smaller onboard components such as GPS and autopilot navigation systems, servos, motors, and for some MAVs, lithium polymer batteries for a power supply. The use of lightweight flexible plastics and fabrics for the wing aid in the aircraft stability, while plastic, spring steel, or carbon fiber shells (among other materials) compose the main structure of the vehicle. Several successful MAVs are described below.

### 2.3.1 Black Widow

The Black Widow is an electric, propeller driven MAV with a 6 inch (15 cm.) wingspan, weighing approximately 80 grams. The foam structure allows for this vehicle to maintain a total flight time of approximately 30 minutes. Also attached to this MAV is a small, two gram video transmitter that allowed for aircraft control and ground

surveillance. This aircraft was one of the first MAVs that proved several points in UAV technology (Grasmeyer and Keennon 2001). It showed that small aircraft are capable of being airworthy, sustaining flight for a reasonable duration of time, and transmitting vital data for civilian and military missions.

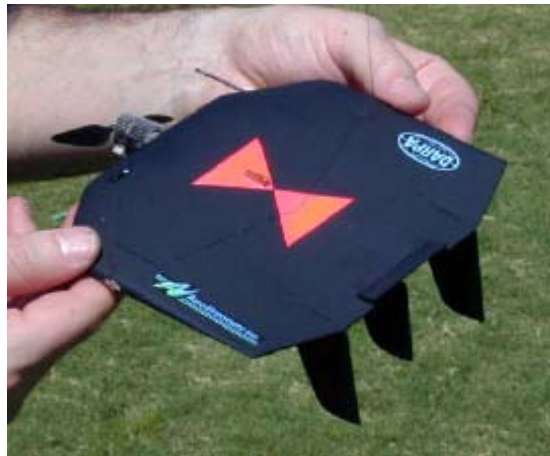


Figure 2.2 – Black Widow MAV built by AeroVironment Inc. (Grasmeyer and Keennon 2001)

### 2.3.2 Microbat

The Microbat was developed by AeroVironment Inc. and the California Institute of Technology and is a 12.5 gram ornithopter capable of flight durations of up to 42 seconds (Pornsirak et al. 1999; Morris 2002). It contains a three gram Ni-Cad battery that powers the flapping wings for this sustained flight. Thin Mylar film and carbon fiber rods are used for the main structure while a small transmission controls the wing flapping. The aerodynamic region to which it operates is much the same as many flapping insects and small birds and is notable for its stable flight at a low Reynolds number of  $10^4$ .

### 2.3.3 UF MAV Development

More recent developments have been made by the University of Florida for a lighter, more robust MAV capable of similar flight duration to the Black Widow while erring to a slightly lower Reynolds number, between that of the Black Widow and Microbat. This 6 inch (15 cm.) aircraft flies at anywhere between 15-25 mph and maintains flight times of 30 minutes. The robust construction of flexible latex film and carbon fiber makes the vehicle virtually indestructible upon landing (Ifju et al. 2002), a highly desired quality for all MAVs. These vehicles can also be constructed within five hours time with the necessary components at hand.

In addition to the innovative construction methods, the UF MAVs were more stable in relation to gust loads. On a typically calm to mild day, the winds are approximately 5-10 mph; with aircraft flight speeds anywhere between 15-25 mph, a normal rigid wing would likely see a 50% increase in lift at any given time due to a gust load. A large benefit was drawn from the flexible fabric wing which absorbed much of the lift that would naturally be generated on its rigid counterpart. The micro air vehicle could thus sustain a more stable, controlled flight.

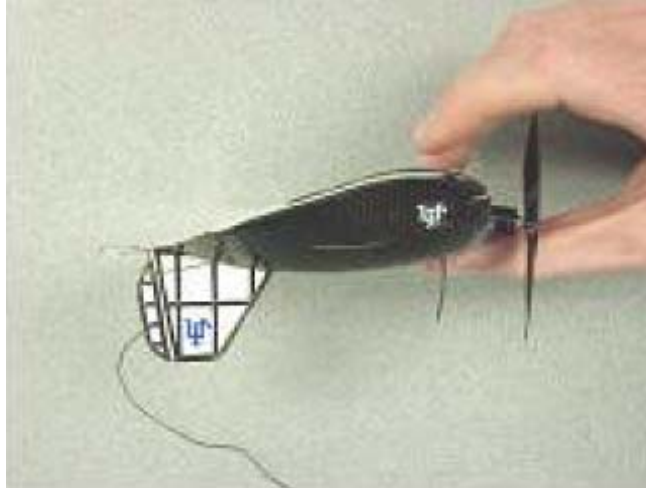


Figure 2.3 – UF 6 inch wingspan MAV built by University of Florida department of Mechanical and Aerospace Engineering, Micro Air Vehicle Laboratory (Ifju et al. 2002)

## 2.4 Balance Systems

A test stand was needed that would be able to read the same aerodynamic measurements for two different specimen types, and as such, sting setups for wind tunnels were investigated.

The most common modern balance systems in use are 6-component internal force measurement gauges. The 6-components for aircraft measurements include, lift, drag, and side force, and pitch, yaw, and roll moments. Due to the wide variety of testing conditions, specimens, and wind tunnels, many balance systems are custom made (Drouin and Girard 1996).

There are many types of balance designs that can be considered for low speed testing, including external and internal systems. As control surfaces were not specifically tested and the MAVs too small for internal balances, these were not considered. Most external systems use a strut for 1: Mounting the test specimen, and 2: Providing a guide to a linkage system for load detection (Rae and Pope 1984). There are several types of

linkage systems such as a platform, yoke, and pyramidal balance which will vary based on testing needs and expected loads. These systems are illustrated in Rae and Pope (1984). The primary concern with the strut mounting approach is the thin wing attachment and avoidance of adverse flow fields around the specimens. Many of the other systems are typically used for large loads.

Some manufactured stings are made of a single piece of material to add to the stiffness of the apparatus. High repeatability for strain gauge responses as well as avoiding hysteresis can be achieved by constructing a balance through this method (Drouin and Girard 1996). Other methods necessary for good results include full Wheatstone bridges for strain gauges, strain gauge placements on symmetrically bending regions (Drouin and Girard 1996), and careful balance of expected forces to prevent large sting deflections. A rather large safety factor should also be considered for the balance to avoid any possible yielding and subsequent plastic deformations that would destroy the apparatus (Drouin and Girard 1996). In most cases the balance system is attached through the base of the wind tunnel or inside, and generally centered such that the specimen remains in the center of the airflow.

Some methods of construction and design are to be avoided in the sting balance such as using screws (Drouin and Girard 1996), as they are typical sources of mechanical displacement that may be difficult to impossible to account for during testing. Coupling is to be avoided between force measurements as this will often lead to more inaccurate data.

Internal strain gauge balances are seen as particularly difficult to integrate as they are limited by the strength needed for the system and the allowable space in the tunnel to

avoid wall effects (Drouin and Girard 1996). Depending on the test specimen, the balance may also require that the force sensing equipment is within, or an integral part of the test piece. This would be difficult because of the small size of MAVs.

Because of the high cost of these balances from commercial manufacturers, a custom sting is generally designed and built to accommodate the testing required for the experiment.

## 2.5 MAV Wind Tunnel Testing

Micro air vehicle wind tunnel testing has been conducted for several different platforms. The University of Florida, the University of Notre Dame, and the University of Arizona have contributed to MAV aerodynamic data. Testing has also been completed by Pelletier and Mueller on thin cambered airfoils (Pelletier and Mueller 2000), and on NACA airfoils by Jacobs and Sherman (Jacobs and Sherman 1939), among others.

The University of Notre Dame testing was for a single MAV platform on multiple wings of aspect ratios 1 and 2 and no camber. These specimens were tested at Reynolds numbers of  $7 \cdot 10^4$ ,  $1 \cdot 10^5$ , and  $1.4 \cdot 10^5$  and were based on the chord of the wing, approximately 4 inches, and a presumed flight velocity of 25 mph (Torres and Mueller 2000). The tested aircraft structure was made out of mostly balsa and fiberglass cloth, with patches of carbon fiber for structural supports.

Testing on the lower aspect ratio wings resulted in achievable angles of attack up to 25 degrees without stalling, with lift coefficients peaking at approximately 1.0 (Fig. 2.5). Stall was not achieved for these wings. The wings with aspect ratios of 2 showed stalling characteristics at 12 degrees with maximum lift coefficients of 0.7. These lift

coefficients of either wing set are not relatively large due to the low aspect ratios and no included camber.

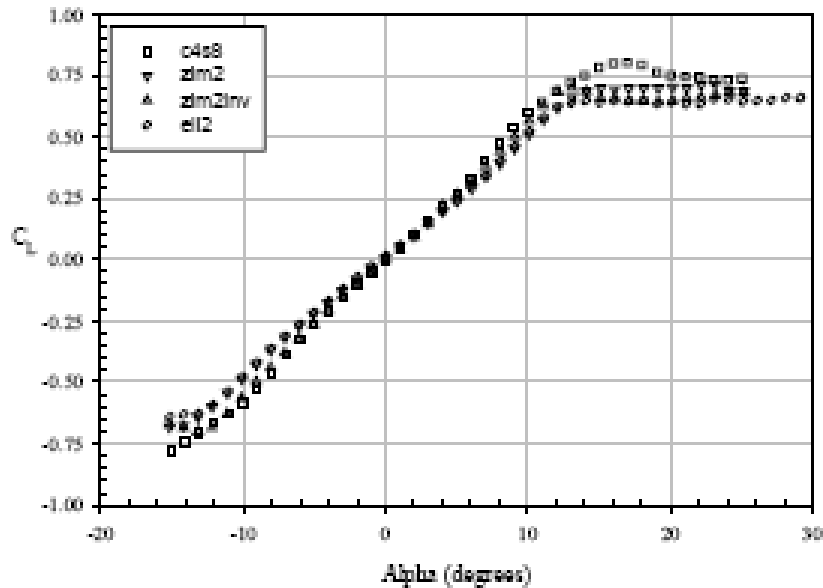


Figure 2.4 – University of Notre Dame MAV Data:  
Aspect Ratio of One (Torres and Mueller 2000)

The MAVs used by the University of Florida contain wings made of a combination of carbon fiber, to maintain the basic wing shape, and a flexible latex fabric, to provide passive stability in flight. A number of wing structures with an aspect ratio near unity and chords of 6 inches were tested at a Reynolds number of  $6 \cdot 10^4$  (Ifju et al. 2002). This testing showed that a higher angle of attack could be achieved without stall through the use of flexible fabric wing structures.

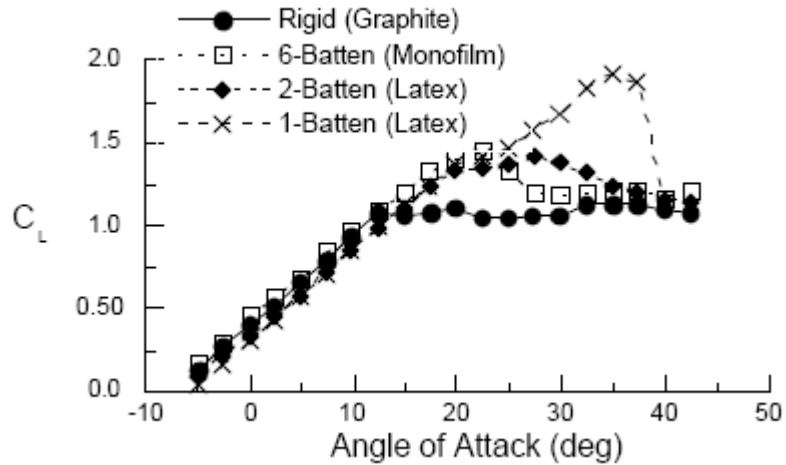


Figure 2.5 – Sample Data from UF MAV Testing completed by University of Florida Mechanical and Aerospace Engineering Laboratory (Ifju et al. 2002)

A Zimmerman style, 25 cm. wingspan planform made of Kevlar cloth and epoxy was used for the University of Arizona MAV testing (Olson et al. 2005). The 1.7 aspect ratio, 3 percent cambered winged MAV was tested at a Reynolds number of  $5 \times 10^4$ . The stall angle was approximately 20 degrees with a coefficient of lift of 0.9 (Fig. 2.6).

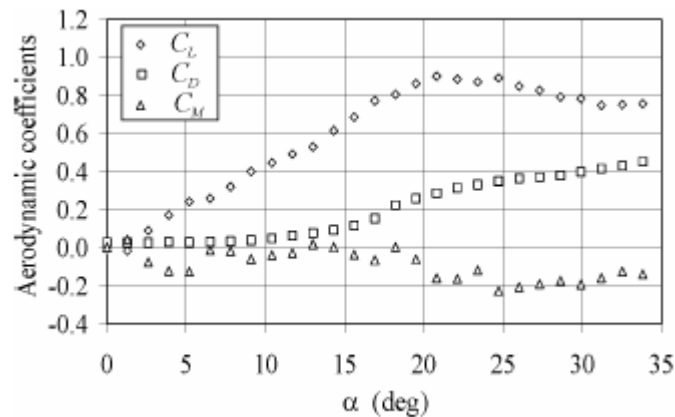


Figure 2.6 – University of Arizona MAV Testing Data (Olson et al. 2005)

Similar characteristics seen for flexible wing MAVs are also seen for rigid thin wings and flat plates. Low Reynolds number testing through  $6 \times 10^4$  to  $3 \times 10^5$  from

Pelletier and Mueller show larger AoA ranges before reaching stall, and likewise for the AoA stall range (no sharp stall curve seen) for the aspect ratios tested of 0.5 to 3.0 (Pelletier and Mueller 2000). The resulting flat plate data showed that the lift curve slopes did not match the two dimensional theoretical values although the lift intercept remained at zero degrees.

As the majority of MAVs have LAR wings, it was important to draw comparisons to HAR or essentially infinite aspect ratio wings. Under NACA wind tunnel testing, various fixed wings of HAR were tested at various speeds, with Reynolds numbers ranging on orders of magnitude of  $10^4$  to  $10^6$  (Jacobs and Sherman 1939). It was first noted that many of the NACA wings tested had wing thicknesses of 9 to 18 percent of the chord length, in comparison to 1 to 2 percent for typical MAVs. Camber characteristics were relatively equivalent in terms of magnitude; 3 to 4 percent was typical for all wings.

Looking at NACA 0009 and 0012 symmetric wings, the sharp differences in the lift and drag coefficients with respect to the magnitude of the Reynolds number was immediately apparent (Jacobs and Sherman 1939). It was noted that the higher Reynolds numbers (with magnitudes of  $10^6$ ) showed higher overall lift coefficients but sharper stall curves, whereas the lower Reynolds numbers of  $10^4$  and  $10^5$  displayed lower coefficients but much more elongated stall curves over angle of attack. The NACA 4412 and 6412 show similar results as well as more parabolic stall curves, even at the higher Reynolds numbers (Jacobs and Sherman 1939).

The typical lift coefficients for either LAR or low Reynolds number wings and MAVs ranged from 0.8 to 1.4 depending on specific aspect ratios, wing thicknesses, and camber. Low values of lift to drag ratios were seen for MAVs, typically 3 to 8 (Morris

and Holden 2000; Lian et al. 2003; Waszak et al 2001) and were primarily due to the LAR wings. Should higher aspect ratios greater than one be considered, higher lift to drag ratios would be expected.

These wind tunnel tests showed that flexible wings can achieve AoA up to 30-40 degrees before stall effects were seen; these high angles were taken into consideration for the sting design described in the next chapter. The data comparisons would indicate that for single, fixed wing structures, the stall angles of attack are much lower with sharper drops in the coefficient of lift. Flexible wings as well as some fixed wings such as the NACA 8318 are able to attain sometimes higher lift coefficients, and parabolic stall curves (Jacobs and Sherman 1939). These parabolic lift curves are seen in some of the low aspect ratio, flexible wing MAVs and as such are fitted to a second order equation as is typical for LAR wings (Olson et al. 2005; Torres and Mueller 2000).

The wing flexibility, achievable angle of attack before stall, aspect ratio, and wing construction method were all taken into account when designing the test specimens for the current MAV platforms being developed. The high angles of attack achieved by some flexible wing designs was desired, however the low lift to drag ratios was a certain drawback. A slightly larger aspect ratio would improve upon this characteristic.

## CHAPTER III

### DESIGN and FABRICATION

#### 3.1 General

Components were designed and fabricated for flexible wing and MAV testing. Parts needed included wings and aircrafts, the sting, the method used for angle adjustments, and a camera mount for video recording.

#### 3.2 Wing and Aircraft Designs and Construction

Ten wings were designed and constructed all with a 16 inch wing span and 6 inch root chord. These wings had two airfoil shapes; a predefined University of Florida airfoil and the mean camber line for the NACA 8300 airfoil. The aspect ratios for these wings ranged from 2.1 to 2.7, and are considered LAR wings. Ideally for thin wings there is no thickness; the constructed specimens had a thickness of 1.4 percent of the root chord length.

The fabrication process for the wings consisted of using pre-impregnated carbon fiber and a lightweight flexible fabric called Icarex<sup>tm</sup>. High density blue foam molds were machined with the wing contours for the wing layout. A Teflon film, PTFE, was adhered to the mold and the wing design laid out on top of that. Another layer of PTFE was adhered on top of this, upon which carbon fiber and the flexible fabric were placed to constitute the wing. A final layer of PTFE covered the wing and the entire piece placed in a vacuum bag in preparation for baking. The PTFE layers made for an easy wing release from the mold after the wing was hardened from baking. The bag was sealed,

held at zero pressure, and baked for several hours while the epoxy in the carbon fiber spread and hardened. After baking, the wing was then taken off the mold and sanded down as needed. This process was initially developed by the University of Florida (Ifju et al. 2002) to be further used and adapted by Case. The same process was used to create the all carbon fiber fuselage shells and tail pieces.

The five types of wings made for this project all had specific distinctions; two wings had fully elliptical planforms, with a major axis of eight inches and a semi-major axis of three inches. Two wings had a rectangular planform for maximum wing area and potentially higher total lift. Winglets one inch high and two inches long were placed on two elliptical wings in order to reduce the induced drag on the wing. A rigid wing comparison was also made by making two all carbon fiber rectangular wings.

A concern for the thin flexible wings was the knife edge at the leading edge of all the wings. With this sharp edge there was a possibility that a clear stagnation point could not be created at the leading edge. For the last two wings, an eighth inch carbon fiber tube was baked onto the wing and wrapped with additional carbon fiber. The LE was sanded down to create a small teardrop, eliminating any sharp edges and providing a clearer location for the stagnation point. These two wings were created with this rounded leading edge; one with a UF tapered planform and one with an 8300 rectangular planform. All planforms tested are shown in figure 3.1, below.

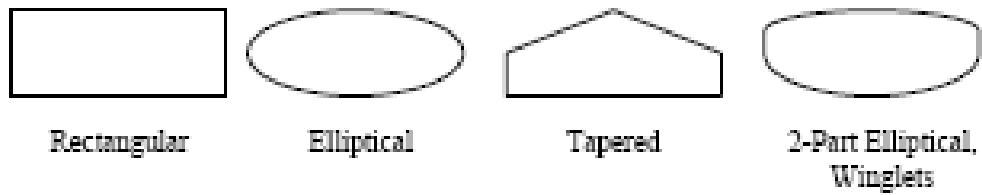


Figure 3.1 – Tested Wing Planforms

A tab was added to the back ends of all the wings, 1.5 by 1.5 inches, with two 8-32 clearance holes on the centerline for an attachment point onto the testing apparatus. For all eight flexible wings the baton structure was kept the same, with five on each side. The purpose of the batons was to maintain the wing structure while still allowing for some flexibility if subjected to a gust load. The angles and distances between the batons with respect to the leading edge was kept the same while the lengths were modified based on the wing planform to reach the outer edge of the fabric (Fig. 3.2). The root chord leading edge was approximately one inch wide for all wings.

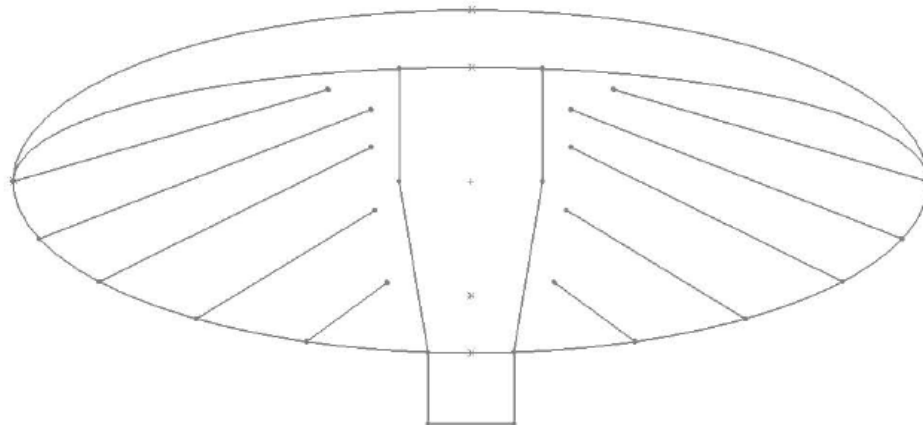


Figure 3.2, Elliptical wing baton structure, design

Four layers of carbon fiber were used for all sections on the wings, as this was the current method for all wings in flight preparation. This amounted to an approximately

0.040 inches thick wing, with the exceptions of the baton structure, with 0.020 inch thick sections, and the flexible fabric, less than 0.010 inches. For the fuselages, the entire shell consisted of two layers of carbon fiber, with several extra layers placed at the nose of the fuselage to simulate one ready for flight testing, in case of a hard landing. Each layer of carbon fiber used was approximately 0.010 inches thick. Pictures of all wings used in testing can be seen in appendix F.

For aircraft testing there were two fuselages used, one with the frontal areas narrow and tall, designated fuselage B, and the other short and wide, designated fuselage C. Fuselage B had a frontal area of  $1 \frac{3}{4}$  by  $1 \frac{7}{8}$  inches tall while fuselage C was  $2 \frac{1}{8}$  by  $1 \frac{1}{2}$  tall. The tail was 6 inches wide,  $5 \frac{5}{8}$  inches long and  $1 \frac{3}{4}$  inches tall. Both fuselages were 13 inches long with placements in the rear for the tail attachment. These fuselages were specifically machined for component and system placements inside the shell. Two 8-32 clearance holes were placed at the back of the tail for the adapter attachment. The tail and wing were then tied securely to the fuselage using thin Kevlar thread, such that they could easily be substituted with another part. Figure 3.3 shows the fuselages and tail used for the aircraft testing.



Figure 3.3 – Fuselage B (Top Left) and C (Top Right), Uni-tail (Bottom)

### 3.3 Sting Design and Setup

The sting was designed to detect changes in lift, drag and pitching moment on a wing or aircraft specimen. Roll, yaw, and side force on the specimen were not considered for testing, as it would add complexity to the sting design, and these aerodynamic characteristics did not claim high importance here as control surfaces were not tested. A major concern for the sting design was that it did not contribute significantly to the airflow around the specimen. A disruption in the airflow around the wing or MAV would adversely affect the forces on the sting, yielding incorrect results. The specimen also needed to be placed near the center of the wind tunnel test section, so no boundary layer or pressure difference effects would be detected from any side of the wind tunnel.

One design consideration included a mount directly below the specimen, a strut mount, and has been used in other testing scenarios (Rae and Pope 1984; Drouin and

Girard 1996), yet this would affect the flow around the specimen. Although this design would result in a smaller resultant moment on the apparatus, it was determined that the mounting system would be large in comparison to the specimens tested and thus not feasible. The other design considered was that of an inverted L that either went through the wind tunnel test section or was mounted to the tunnel. This design was ultimately chosen as it would place the test specimens centrally in the wind tunnel and not affect the flow around the piece.

The sting design (Fig. 3.4), made in SolidWorks (SolidWorks Corp, Concord MA, USA), includes two dog-bone cutout sections with strain gages for lift and drag detection and an instrumented necked section forward of the lift dog-bone cutout for bending moment detection. The one piece L shaped sting was made out of 6061 aluminum and attached to a mounting plate that would connect the apparatus to the wind tunnel test section using two ¼-20 screws at the front of the mounting base. The inverted L was approximately 10 inches high and 6 inches long, with 8-32 threaded holes forward of the necked section for adapter attachments that would change the angle of attack of the mounted test piece. The sting was ½ inch by ½ inch thick to provide enough strength in the apparatus during testing. The entire apparatus was made using a HURCO VM1 CNC machine (HURCO Companies Inc, Indianapolis IN, USA). Drawings of the sting can be found in appendix D.

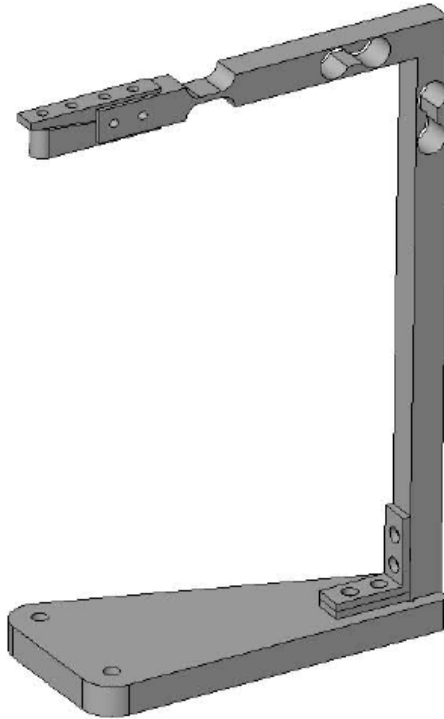


Figure 3.4 – Initial sting design with mounting plate, horizontal angle adapter included

This design allowed for moment, lift, and drag forces to be measured independently of one another. A positive force at the end of the sting would therefore affect only the lift and moment by deflecting the lift dog-bone cutout at the top of the sting, and provide a bending moment about the necked section (Fig. 3.5).

The design also made possible the attachment of horizontally and vertically oriented test specimens. Many of the early aircraft used a single vertical stabilizer down the back center of the tail and required a vertical clamp, while the wings required a horizontal clamp. This did require the use of screws for an attachment method, which is discouraged (Drouin and Girard 1996). However, as the testing was for low speeds while those referenced were for transonic or supersonic speeds, hysteresis would most likely be negligible or non-existent.

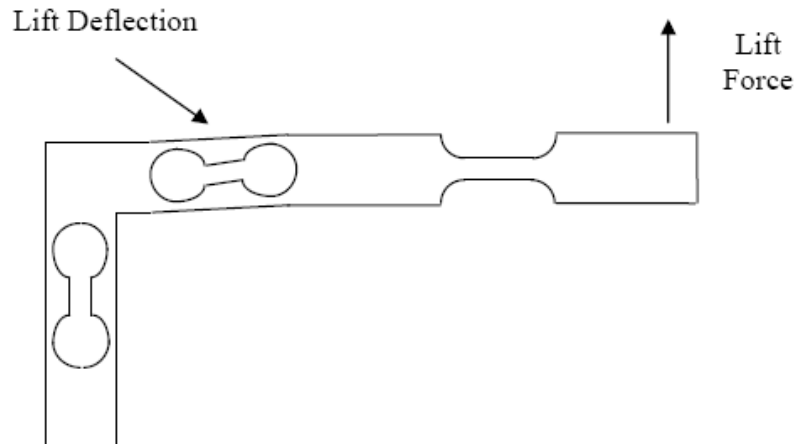


Figure 3.5 - Sting deflected with lift force

### 3.4 Adapter Designs and Methods of Attachment

The two types of adapters, horizontal and vertical clamps, were made out of 6061 aluminum for specimen attachments. The horizontal clamps were to be used for holding onto the back tab of a wing using 8-32 button head screws, while the vertical clamps were used for holding onto the vertical stabilizer of an aircraft.

Vertical clamps were machined at every three degrees, from negative six to twelve, while the horizontal clamps were machined at every degree, from zero to twenty five degrees. The vertical clamps were used for preliminary tests on aircraft with single, centralized vertical stabilizers. Based on the flexible wing MAV data from the University of Florida (Waszak et al 2001), angles of attack of thirty degrees or higher could be achieved without reaching stall. Thus more adapters would be made if stall was not seen using the current adapters. Figure 3.6 shows the design for the horizontal and vertical adapters for a positive six degree incline.

The tail section for the aircraft was later redesigned to accommodate two vertical stabilizers at the sides of the tail, so the horizontal clamps were used for all testing. The

horizontal adapters were 2 inches long, with a back tab that attached to the sting 1/8 inch thick and 1 inch long. There was a 0.030 inch gap between the two pieces when attached to the sting; Spacers were also made in order to increase the gap size to up to 0.080 inches. This allowed the specimens to slide more easily into the adapter mount due to slight changes in the specimen thicknesses.



Figure 3.6 - Vertical (Left) and horizontal (Right) adapters

### 3.5 Camera Mount

A camera mount was made in order to take video or picture data if necessary during testing. This mount was designed to slide onto an outer section of the wind tunnel and remain in that location for consistent video capturing and stills. It was placed such that the camera view would show the wing airfoil or aircraft side. The two pieces were made out of delrin, with 45 degree cuts that allowed the camera or camcorder appendage to slide easily onto the camera mount piece (Fig. 3.7 – 3.8).

The top portion of the mount consisted of the U-bracket with the three 45 degree cuts for the camera or camcorder and was 3/8 inch high, 3 inches wide and 5 inches long. The bottom lip was manufactured to connect to the top portion as well as hold the mount onto the side of the wind tunnel using two 8-32 button head screws. This piece was 3 inches wide, 3 inches long and 1/4 inch high with an extra 1/4 inch thick protruding lip. Figure 3.8 shows the attachment location onto the wind tunnel side. The camera position could be adjusted on the appendage to ensure a head on view of the test specimen. Pieces were machined manually on a Bridgeport Series 1, 2 hp (Hardinge Inc, Elmira NY, USA).

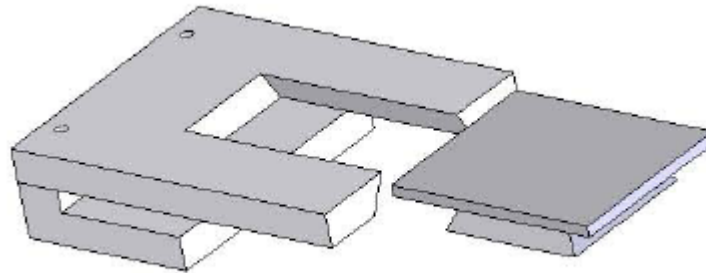


Figure 3.7 – Camera mount design



Figure 3.8 – Camera mount attached to wind tunnel side

## CHAPTER IV

### TESTING METHODS

#### 4.1 General

With all parts for the experiments fabricated, methods for testing were needed to ensure correct and accurate data collection.

#### 4.2 Balance Calibration and Coupling

Strain gauge sets were used for force and moment detection on the sting-balance. Full Wheatstone bridges were used for lift and drag along each of the dog-bone cutouts, while a half bridge was used for the bending moment detection. Figure 4.1 shows the strain gauge placements on the sting.

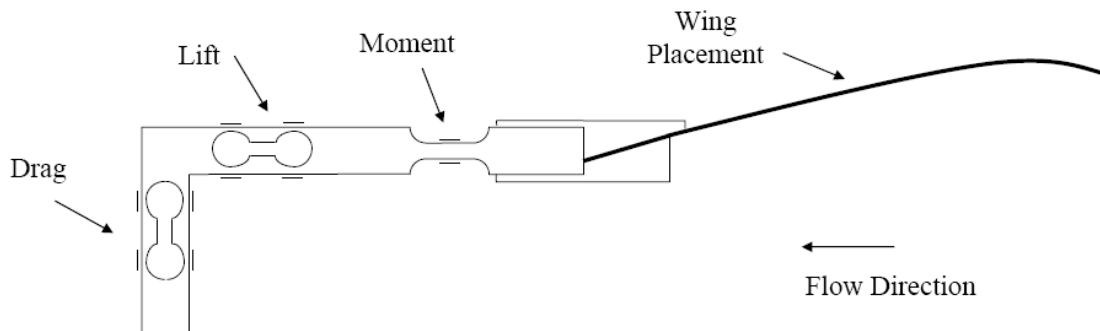


Figure 4.1 - Strain gauge placement for sting apparatus

The sting was calibrated in two different orientations, using a set of masses of 50, 100, 200, and 500 grams. Voltage values were recorded for lift, drag, and moment for all masses, including zero mass, for both orientations, shown below in figure 4.2.

Orientation 1 was the sting position used for wind tunnel testing. For the sting calibration a linear fit was made between voltage and force for all sets of strain gauges assuming that the sting operated only in the linearly elastic range.

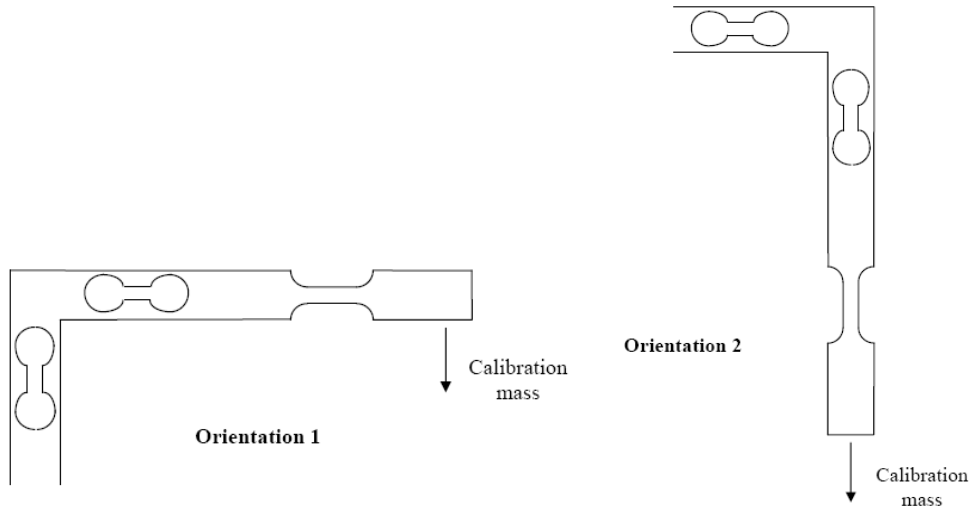


Figure 4.2 - Sting calibration orientations 1 (Left) and 2 (Right)

Lift and bending moment were gathered from orientation 1 strain gauge readings, while the drag calibration line information came from orientation 2 strain gauge readings. The lift and moment calibration for orientation 2 revealed a constant voltage versus force line, meaning that a force applied in this direction did not affect the lift and moment values. This was expected as the strain gauges for lift and moment were only in tension in this orientation and the change in resistances should be equal on either side. In orientation 1 the drag was slightly influenced by the lift, which coupled the drag calibration. This was accounted for in the drag calibration line by adding the slope multiplied by the lift force into the drag force calibration line (See equation 3).

A linear least squares fit was performed for each calibration line and it was determined that the correlation coefficient,  $R$ , was approximately one in all cases,

representing a good fit. This also confirmed that the sting under these loads was in the linearly elastic range and would not be subject to permanent deformation. The calibration line for lift in volts is

$$V_L = X_L * .0042 - .7771 \quad (1)$$

where  $V_L$  is the voltage and  $X_L$  is the mass in grams for lift. The moment calibration is

$$V_M = X_M * (-.0013) + 1.4929 \quad (2)$$

where  $V_M$  is the voltage and  $X_M$  is the mass in grams. The drag calibration is

$$V_D = (X_D * .0043) + 5.8424 - \left( .0001 * \frac{L_{Tot}}{g} \right) \quad (3)$$

where  $V_D$  is the voltage and  $X_D$  is the mass in grams and the coupling due to lift is

$-\left( .0001 * \frac{L_{Tot}}{g} \right)$ .  $L$  was defined as lift of the wing alone, without the weight included so,

$$L_{Tot} = (X_L - X_{L_{v=0}}) * g \quad (4)$$

where  $L_{Tot}$  is the net lift,  $X_L$  is the lift generated in grams, and  $X_{L_{v=0}}$  is the weight.

The equations for the voltage were then resolved for the mass of lift, drag and moment. Matlab code, included in appendix C, was developed to back out the mass values for the forces and moment for all wings and aircraft tested. The resolved equations were

$$X_L = \left( \frac{V_L + .7771}{.0042} \right) \quad (5)$$

$$X_M = - \left( \frac{V_M - 1.4929}{.0013} \right) \quad (6)$$

$$X_D = \left( \frac{V_D - 5.8424 + .0001 * \frac{L_{Tot}}{g}}{.0043} \right) \quad (7)$$

For the moment in gram meters, the mass values were multiplied by the distance from the calibration point to the resultant moment point, which is discussed in further detail in section 5.2. The resultant moment was

$$M_R = X_M * a * g \quad (8)$$

where a is the distance from the calibration point to the moment strain gauge center. The calibration masses  $X_L$ ,  $X_D$ , and  $X_M$  were used for all wing and aircraft data analysis.

### 4.3 Initial Testing

The initial setup of the sting apparatus consisted of the sting itself and a mounting plate, which rigidly connected the sting to the wind tunnel. A T-square, level and ruler were used to orient the sting parallel to the test section and to determine there was no roll, pitch or yaw on the sting when rigidly attached. 0.002-0.003 inch thick spacers were used to adjust the sting as necessary for the correct orientation. Initial tests were completed on an 8300 rectangular flexible wing at velocities of 5, 7.5, 10, and 12.5 meters per second and at angles of attack of 0, 3, 6, 9, and 12 degrees. These sample tests helped to determine whether any changes in the apparatus needed to be made, and to assure that the sting could measure forces of the appropriate magnitude.

As some of the flight tests included aircraft with masses of 350 grams, it was determined that a maximum lift force on a wing should be up to 300-600 grams. As lift to drag ratios of around 6 were expected based upon micro air vehicle data from the

University of Florida (Lian et al. 2003), the expected drag was approximately 50-150 grams. NACA 8318 airfoil data shows an aerodynamic moment coefficient of about negative 0.13 (Jacobs and Sherman 1939) and it was assumed that similar results would be likely for the NACA 8300 wings tested.

These tests did confirm that appropriate magnitudes of forces and moments would be measured once a final experimental procedure was determined. However it was realized that several changes needed to be made for more accurate results in the experiment. At the larger test velocities and angles of attack, the sting was subjected to large vibrations, yielding unsteady values in lift, drag, and moment, changes in angle of attack, and possibly deforming it beyond the linear elastic range. The vibrations on the sting and wing were too high for accurate data collection as the leading edge of the wing at high velocities (10-12.5 m/s) was vibrating a quarter of an inch or more. The angle of attack on the wing also changed based upon the speed of the incoming airflow; In effect the angle changed based on the forces the specimen was subjected to. The wing also flexed based upon the incoming velocity, changing the curvature along the wing. These three problems are addressed in the following sections.

#### 4.4 Sting Modifications

Several sting modifications were tried in order to prevent vibrations of the apparatus. By modifying the setup, higher angles of attack could be reached during testing and allowed the test specimens to attain a stall angle.

#### 4.4.1 Rubber Inserts

The first approach to try and prevent the vibrations was to place rubber inserts into the dog-bone cutouts in the sting. These inserts were made of a low stiffness, high damping material (Actual rubber material specifications unknown) such that it would not deform appreciably once placed into the cutouts. This would potentially stiffen the sting in those two sections and reduce vibrations.

Several tests were conducted with an 8300 Rectangular Flexible wing at multiple angles of attack. The inserts however did not prevent vibrations in the sting; rather the lift and drag were unsteady due to the rubber inserts moving slightly in the dog-bone cutout, applying a varying force to the strain gauges mounted directly outside the cutouts. No other rubber inserts were tried as it was likely more tests would yield the same conclusion.

#### 4.4.2 Damper Attached Via Connection Rod

For a second approach a damper was placed into the sting design, attaching it to the base of the sting with a cylindrical bar connecting the damper to the sting, forward of the bending moment strain gauges. The damper was purchased from Airpot (Airpot Corp, Norwalk CT, USA), with a glass on rubber slide for little friction. The bar was designed to be 11 inches long, 3/16 inch diameter with both ends threaded, one 4-40 in order to connect to the damper, and the other 8-32 to connect to a sting mounted screw. A threaded hole was made into the existing sting base plate for attachment of the bottom end of the damper, centered directly under the sting.

Upon further inspection of the design it was realized that the bar connecting the damper to the sting would produce a sizeable amount of drag. In addition, this drag had the possibility of creating more vibrations on the sting, rather than relieving them.

In order to remedy this, symmetric airfoil sections were staggered on top of each other directly below the sting to raise the damper closer to the horizontal section of the sting. The airfoil sections were designed from a NACA 0012 airfoil with a 9 inch chord. The first  $5 \frac{5}{8}$  inches of the airfoil were used for the mounting plates, with back end of the airfoils cut flat. This allowed for a  $\frac{1}{4}$  inch space between the mounts and the sting, such that it did not affect the drag strain gauge readings. Each of the 11 sections made was  $\frac{1}{2}$  inch thick. These airfoil sections cut down the length of bar needed from 8 to 2 inches, and would reduce the drag and vibrations on the apparatus. More airfoil sections could have been used for further drag reduction; however they would impede the ease of assembly for the damper and angle adapters on the sting. The airfoil sections were centered in front of the back vertical bar of the sting for a symmetric flow around the sting. In order for the airfoil sections to be centered, a new mounting plate was machined, making the entire apparatus symmetrical. The new apparatus can be viewed in figure 4.3. Further testing showed that the vibrations seen previously were greatly reduced.

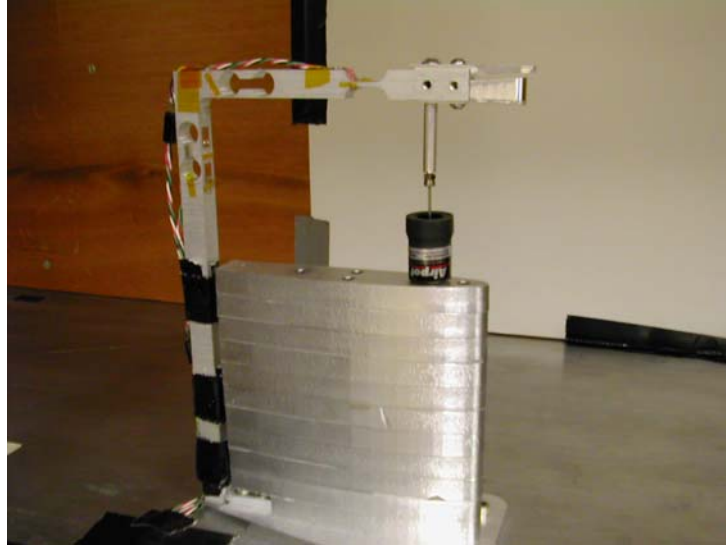


Figure 4.3 – Final Test Apparatus

#### 4.5 Dashpot Testing

With the damper in place, more tests were conducted on the 8300 rectangular flexible wing. These results showed the 5 and 7.5 meter per second test velocity data significantly skewed from all other data when comparing the coefficient of lift.

Although the dashpot was designed with little friction, it was thought that friction within the system would prevent the test specimen to reach its true equilibrium point and thus the true data, skewing the resulting forces. To test this, the dashpot damping coefficient was changed via a screw on the bottom of the dashpot. The coefficient was not specifically known, but the damping force ranged from zero to 1.0 (push direction) and 1.4 (pull direction) pounds (2KS95A0 Model, Airpot Corp.). The dashpot was fully tightened for the maximum damping, then loosened a  $\frac{1}{4}$  turn, and finally fully loosened such that the damping coefficient was nearly zero. Data was taken on the 8300 rectangular flexible wing at 0, 5 and 7.5 meters per second for each of the damping coefficients and the results compared in figure 4.4. Since all of the 10 and 12.5 meter per

second data fit well to the  $C_l$ ,  $C_d$ , and  $C_m$  curves from the testing completed after the damper inclusion, it was determined the dashpot effects for these velocities were negligible.

Plots of balance mass versus relative damping coefficient were made for lift, drag, and moment. As seen below in figure 4.4, the mass of lift does not change appreciably with a varying damping coefficient. In the figure, “0” along the x-axis refers to no damper attached to the sting, while “1” refers to the damper being attached but with very little damping applied. “2” refers to the damper with a  $\frac{1}{4}$  turn from the maximum damping, and “3” refers to the maximum damping coefficient applied in the dashpot. The data showed very little evidence there was any friction within the dashpot itself: The standard deviation in the lift for all the tests was approximately 0.5-1.7 grams, depending on the incoming velocity. All data was within the standard deviation errors for their respective velocity. It was determined that the discrepancy on the wing data between the data for 5 and 7.5 meters per second velocities against all other data came from another factor, or would be within specified error tolerances.

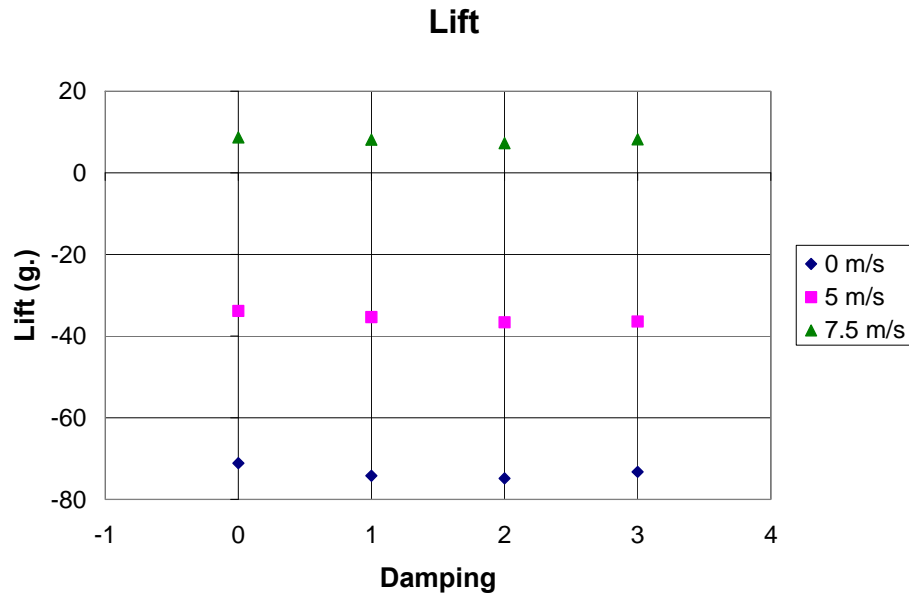


Figure 4.4 – Damping Coefficient vs. Lift Mass

A larger damper with a maximum damping force of 3 (push direction) and 4 (pull direction) pounds (2KS160A0 Model, Airpot Corp.) was used for the aircraft testing and some wing testing for high angles of attack. This damper was later tested to ensure that similar results would be seen as with the first damper. These results confirmed that this damper also did not affect the resulting values of force or moment on any test specimens.

#### 4.6 Wing Curvature Testing

Techniques were developed to test if airflow caused wing bending that would deform the wing center airfoil shape, which should not change during flight. Wings were then stiffened and more techniques tried; this determined that any deflection in the wings would be negligible, making the specimens ready for further testing.

#### 4.6.1 Image Analysis Technique 1

The first set of image analysis techniques was an edge analysis for only qualitative confirmation with the naked eye to determine whether there was a curvature change of the wing with an applied load. Multiple wings were clamped at the trailing edge and oriented upside down such that it would experience a positive lift force. Wings were loaded with a 500 gram mass, placed at the leading edge for the largest bending moment about the wing. This was equivalent to approximately 120% of the maximum bending moment seen from the initial tests on the 8300 rectangular flexible wing. Two pictures were taken for each wing, loaded and unloaded, for the image analysis.

An edge analysis was completed for both, via trials of several types of analysis techniques. For a first option, a Sobel and Canny image analysis was performed on the pictures using Matlab. In this technique, the image was first converted from RGB scale to grayscale and a threshold applied, filtering all pixels and sorting them to white or black values. This edge detection utilizes a gradient method of determining where edges in the picture are located based upon the pixels values (Pratt 2001). A change in the threshold value would thus alter the edges detected by varying the gradient. A threshold value of zero would yield an essentially all white picture, as most pixels are determined to be an edge, while a value of one would yield a pure black picture as no pixels are found to be an edge. This black and white image showed a clearer view of the wing section. The edge analysis picture was then transposed on top of the original image and aligned as well as possible to see if there was any bending qualitatively.

From this analysis, the results were inconclusive as to whether the wings needed to be stiffened further. The Sobel and Canny threshold did not provide enough

constraints on the wing images to make this decision, as the airfoils seen in the picture were anywhere from 3-10 pixels thick instead of a preferred line of 1-3 pixels.

A Hough transformation was then performed on the images. For this technique, the transformation analyzed the black and white picture, selected line segments, and drew horizontal lines of varying lengths that matched up to horizontal lines on the picture.

This transformation however did not yield as much information as necessary as it did not detect the wing curvature well; thus this image analysis technique was abandoned.

#### 4.6.2 Image Analysis Technique 2

Although still qualitative, a more defined image analysis process was used to detect changes in the curvature of the wings. Several wings were clamped to the side of a table at the trailing edge, and a 500 gram mass placed at the leading edge to maximize the bending moment on the wing, as done previously. Two pictures were taken at the same distance away from the wing, one with the load, and one without.

To improve upon the Sobel and Canny edge detection from the first technique, a pixel filtering method was designed and implemented. Once the pictures were imported into Matlab, all pixels with all RGB values lower than 80 were turned white, while any pixel that had even one RGB value above 80 was turned black. This 80 value threshold varied slightly for each R, G, or B value depending on the wing tested, in order to filter a better image. The airfoil thickness in pixels from this technique ranged from 3-6 pixels, slightly better than the Sobel or Canny analysis. The images were rotated and translated on each other to detect any curvature changes.

From these superimposed images it was determined that the wings needed to be stiffened due to fairly large changes in curvature from the 500 gram load. The midsections of each wing were thus stiffened with four more layers of carbon fiber, resulting in 0.080 inch thick sections on the wings.

#### 4.6.3 Image Analysis Technique 3

A quantitative analysis was then completed to detect wing curvature changes. Whereas the first and second techniques were completed on a full wing, this analysis was only concerned with the center section. On an aircraft ready for flight, the center section is the only part of the wing constrained to the predefined wing curvature, as it is tied and glued to the fuselage. The other sections of the wing could deform under flight loads and thus change in curvature. For this reason only the center section was tested through image analysis for wing curvature changes. This center piece section was created for these tests on an 8300 airfoil and can be seen in figure 4.5.



Figure 4.5 – Center wing section used for wing curvature testing

The test piece was clamped onto the sting, as for normal wing testing. Similar to the first tests of qualitative changes to the wing, a 500 gram load was placed at the leading edge, taped on and held by a string. Both wing orientations were tested, right side up and upside down, such that the wing would simulate a negative and positive lift. Wing angles of attack tested included positive and negative 10 degrees as well as 0 degrees.

Two pictures were taken of the wing section, one unloaded and the other loaded with the 500 gram mass. The same image analysis technique was used as above in the 2<sup>nd</sup> technique, using pixel filtering on both pictures to retrieve only a picture of the airfoil section, displayed in white pixels. Sections of each image were deleted (turned black) as necessary to gain a better view of just the wing profile. With only the airfoil left in the loaded and unloaded image, the remaining white pixels were averaged in each column for each picture, such that a maximum of one white pixel remained in each. All other pixels in the pictures were black. These two airfoil lines, one from each image, were then rotated and translated on top of each other in a combined third image (See figure 4.6). This in itself was a qualitative measure of wing curvature change from a bending moment, as with the first sets of image analysis tests.

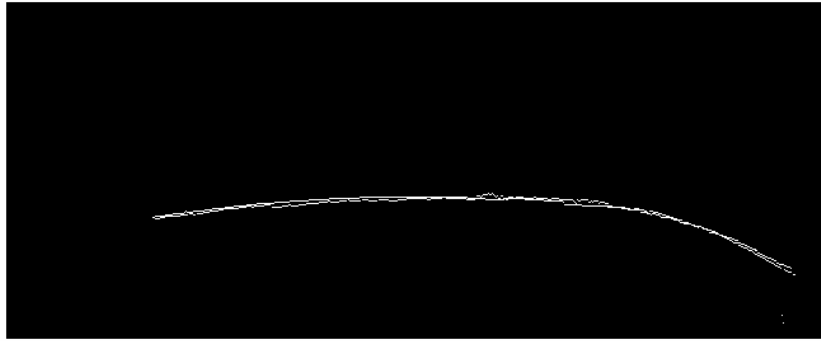


Figure 4.6 – Combined Image for RGB filtering image analysis for a loaded and unloaded wing

It was noted that the LE or TE locations could not be matched up exactly for several reasons. In general if either the TE or LE locations were aligned for the two pictures, the combined picture would not yield the best fit. The camera position may also have moved slightly from picture to picture, as the camera needed to be moved in order to access the wind tunnel apparatus. This would yield slightly different distances to the wing section. This was also seen when the wing was loaded, as the angle of attack of the wing section did change. These varying distances would change the number of pixels detected on the airfoil by the camera therefore not allowing the LE or TE to line up. This amounted to 10-15 pixels of difference for the total number of pixels seen in each picture, compared to an average total of about 150 pixels marking the airfoil line.

Once the two airfoil lines were aligned as well as possible, the pixel locations were compared. If a white pixel existed in the same column for both images, the difference in pixels was calculated between the two. If there was only one white pixel or none in both pictures for a particular column, a difference was not calculated. This was completed for the entire image, with the differences stored in an array. The differences

were then used to calculate a standard deviation of the two pictures to determine the error in the wing curvature.

Once the standard deviation in number of pixels was found, this needed to be converted to inches. The chord length of the wing section was six inches, so the TE and LE were needed for the conversion from pixels to inches. Using the combined image, the TE and LE pixels were selected and the conversion from pixels to inches made. The average deviation for the images was found to be 0.020-0.040 inches, below the thickness of the wing midsection of 0.080 inches. With the standard deviation lower than the thickness of the wing midsection, it was determined that the wing would not bend during wind tunnel testing.

#### 4.7 Picture Testing Methods

Although the damper prevented most of the vibrations on the sting during testing, the sting and adapters did deflect slightly due to the weight and lift on the wing. Therefore pictures were taken of the wings in several lighting conditions to determine the best way for measuring the angle of attack.

##### 4.7.1 Black Light Testing

The first set of conditions consisted of cutting off the ambient light to the wind tunnel test section and placing a black light in various positions inside and outside the wind tunnel to light up the wing. Positions for the black light inside the tunnel included the upper left and right corners as well as the bottom left and right corners, all of which

were adjacent to the sting and specimen. The black light was also tested on top of the wind tunnel through a piece of acrylic.

A UV marker was used on an 8300 rigid wing specimen down the centerline to mark the trailing and leading edge. These tests were also conducted with two varying camera positions, one viewing the side of the wing and the other viewing the bottom section. A color filtering analysis much the same as for the curvature tests was used to determine the angle of attack of the wing. Tests were conducted at zero degree adapter angles for all test velocities (5, 7.5, 10 and 12.5 meters per second), however at high velocities the UV line was blurry due to small vibrations.

A second test allowed a small amount of light into the test section behind the camera; however the UV line on the wing was faint or did not show up at all.

#### 4.7.2 Ambient Light, Perspective Testing

A new approach allowed the ambient light from the room into the test section and did not include the use of the black light. A white poster background was placed into the test section in order to see the wings with more color contrast. A white dot marked the leading edge of the wing such that it was in the same plane as the back tab of the wing on the left side. A head on view with the camera would thus give a perspective view of the wing, and the trailing and leading edge marked locations would yield the angle of attack.

A model of a camera perspective view was created in SolidWorks in order to test and confirm that a perspective view would yield the same wing angle of attack on a 2D image (Fig. 4.7). A tube with a depth of 16 inches was created to represent the view inside the wind tunnel, from the side. A flat plate with dimensions of 6 by 16 inches at a

5 degree angle of attack was placed inside the tube at the center. A perspective view was then applied to the SolidWorks model to recreate that of the camera. A .jpg image was saved of this view for an image analysis to determine the angle of attack on the flat plate. The distance to the edge of the model was then adjusted to give a different perspective view, and another image created. This was done for distances of 0.02, 0.2, 2, 20, and 200 inches away from the model. The position of the flat plate was then changed to the upper right corner, and the process repeated for the same distances. Images were analyzed by manual pixel selection to determine the angle of attack of the flat plate. Through this analysis, all angles of attack were determined to be approximately 5 degrees, as the pixel selection would not yield exact results. This showed that as long as the camera plane was parallel to the wing tip airfoil or two points in the same plane on the wing, it would yield the correct angle of attack.

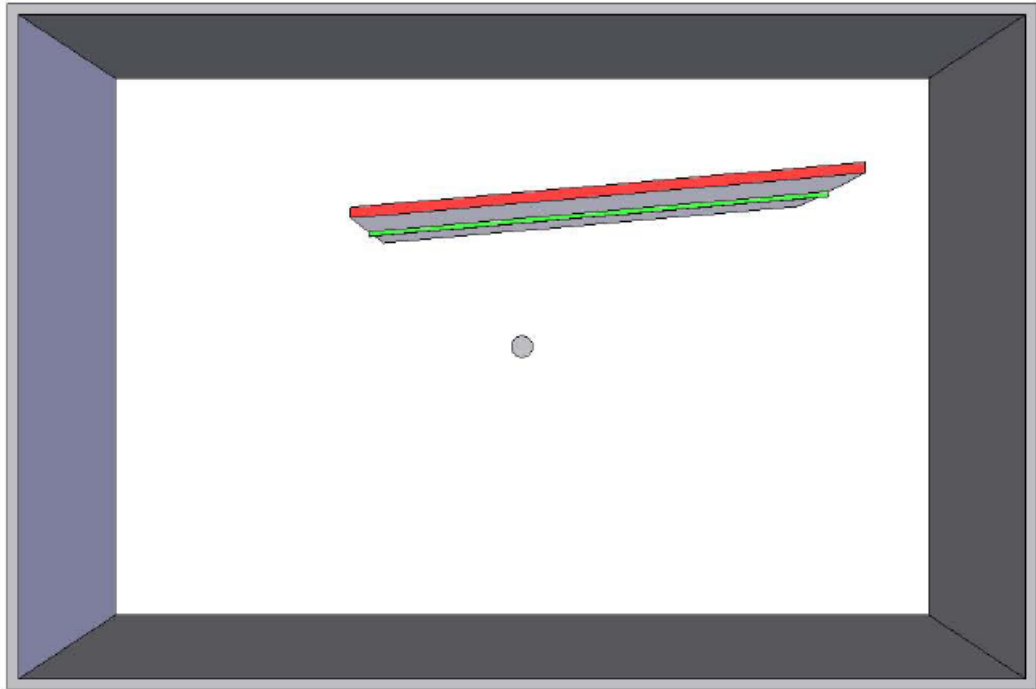


Figure 4.7 – SolidWorks model for perspective view testing

Knowing that the perspective view gave the correct angle of attack measurement, it was determined that the pictures from the ambient light testing yielded the best results, even under small vibrations from either a high angle of attack or high velocity. The pixel locations for the trailing and leading edge were computed by manual pixel selection. Where the wing underwent small vibrations, several pictures were taken so an average angle of attack could be determined. With the angle of attack measurable, the full testing on wings and aircraft could be completed.

#### 4.7 Final Experimental Procedure

A step by step procedure was laid out for all data collection based on the tested methods. With the wind tunnel first powered up, the pressure transducer was calibrated

such that the pressure offset corresponded to zero dynamic pressure, yielding a velocity of zero meters per second. An angle adapter set was attached to the sting along with the damper and test specimen. For negative angles of attack, the adapters were placed upside down onto the sting and the specimen subsequently attached.

Once the apparatus was secured in place, the motor was turned on and set for a velocity of 5 meters per second. After a steady motor rpm was established, a picture was taken of the wing to determine the angle of attack. Data was collected through Labview, by means of a DAQ card that allowed for one channel to be read at a time; the lift strain gauge voltages were read in first, followed by the moment, and finally drag. Data from the strain gauges was read at a frequency of 1000 Hz for 20 seconds each, taken over the course of one minute for all strain gauge set readings. Files were saved according to the specimen used, the velocity tested, the adapter angle used, and whether it was a lift, drag or moment recording. The wind tunnel velocity was then increased to 7.5 meters per second and the process repeated. When all velocities were tested, either the specimen or adapter was switched out and more tests were conducted.

Aircraft data was collected in the same way as for the wing data, except that the angle of attack computed in the picture was for the aircraft fuselage. The angle of attack of the wing with respect to the aircraft was later added to all values for the true angle of attack. As the center of lift of the aircraft was farther away from the sting apparatus, fewer data points could be collected. The angle of attack changes on the aircraft due to the lift were much greater than that of the wings and vibrations in the setup were detected at much lower angles.

## CHAPTER V

### DATA ANALYSIS

#### 5.1 Tested Wings and Aircraft

All wings and aircraft were tested from approximately the zero lift angle of attack to stall in an open circuit, low speed wind tunnel designed and built at Case Western Reserve University (Case Western Reserve University, Cleveland OH, USA). The test section contained a 2x2 foot cross section; no boundary layer effects from the wind tunnel walls would affect the test specimens as there was a minimum of four inches on all sides. Data was collected for five velocities: 0, 5, 7.5, 10, and 12.5 meters per second for the lift, drag, and resultant moment on each specimen. The corresponding Reynolds numbers for the tests conducted were  $5.67 \cdot 10^4$ ,  $8.50 \cdot 10^4$ ,  $1.13 \cdot 10^5$ , and  $1.42 \cdot 10^5$ , and were based on the constant root chord of 6 inches. The ten wings, a flat plate, and four aircraft were tested, where the aircraft were determined based upon the two best performing wings. The wings and flat plate were thus tested and analyzed first before aircraft testing was conducted. The wings and aircraft were designated numbers and acronyms for easier referencing, and are included in table 5.1, below.

| <b>Wing Designation</b>     | <b>Wing Description</b>                                     |
|-----------------------------|---|
| FP                          | Flat Plate  |
| Wing 0                      | 8300 Rectangular Flexible Wing                              |
| Wing 1                      | UF Rectangular Flexible Wing                                |
| Wing 2                      | UF Rectangular Rigid Wing                                   |
| Wing 3                      | 8300 Rectangular Rigid Wing                                 |
| Wing 4                      | 8300 Elliptical Flexible Wing with Winglets                 |
| Wing 5                      | UF Elliptical Flexible Wing with Winglets                   |
| Wing 6                      | UF Tapered Flexible Wing with 1/8" LE Thickness             |
| Wing 7                      | 8300 Rectangular Flexible Wing with 1/8" LE Thickness       |
| Wing 8                      | 8300 Elliptical Flexible Wing                               |
| Wing 9                      | UF Elliptical Flexible Wing                                 |
| <b>Aircraft Designation</b> | <b>Aircraft Description</b>                                 |
| BW0                         | Fuselage B with 8300 Rectangular Flexible Wing              |
| BW4                         | Fuselage B with 8300 Elliptical Flexible Wing with Winglets |
| CW0                         | Fuselage C with 8300 Rectangular Flexible Wing              |
| CW4                         | Fuselage C with 8300 Elliptical Flexible Wing with Winglets |

Table 5.1 – Wing and Aircraft description designations

## 5.2 Data Analysis: Matlab Conversions

Matlab code was used to back out the values for the resultant moment, lift, and drag using the calibration equations established in section 4.1. These equations were solved to find  $X_L$ ,  $X_M$  and  $X_D$ , the effective balance masses of lift, moment and drag on the specimen.

Of further interest were the coefficients of lift, drag, and moment about the  $\frac{1}{4}$  chord point on the wing. In order to find these coefficients, a force body diagram was needed for an analysis of the system to establish the true forces and moments (Fig. 5.1). The lift, drag and moment center were taken about the  $\frac{1}{4}$  chord point, which is the aerodynamic center on a symmetric airfoil (Anderson 2001). It was assumed that this point would be close to the aerodynamic center for all the wings tested. A force body diagram of the wing is shown below with lift and drag acting at the  $\frac{1}{4}$  chord.

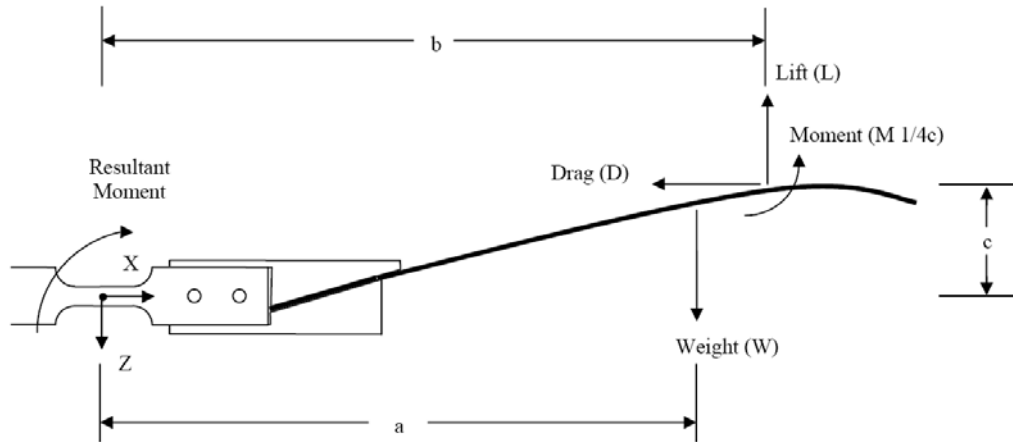


Figure 5.1 - Force body diagram for wing data analysis

A summation of moments about the strain gauge center point for the bending moment resulted in,

$$\sum M_R = 0 = M_R - Dc - Lb - M_{1/4c} + Wa \quad (9)$$

The  $M_{1/4c}$  could then be solved for with further analysis.

The moment arms for lift and drag were calculated based on the geometry of the sting and angle of attack of the wing or aircraft. The drag moment arm varied slightly based on the angle adapter used, and was included in the computations. The resultant moment and the moment due to weight were established in section 4.1 with equation (8). The weight of the wing and adapter was found using the zero meters per second data, as in equation (4), in order to solve for the total lift produced from the test specimen.

The zero meters per second data was factored out for the net drag using

$$D_{\text{net}} = (X_D - X_{D_{v=0}}) * g \quad (10)$$

in case a non-zero drag was found at zero meters per second.

In addition to accounting for the zero value drag, weight, and moment, the apparatus itself had the possibility of adding to the drag, lift, and moment values at each of the velocities tested. Therefore the apparatus was tested alone with the zero degree adapter attached along with the damper. It was found that the lift and drag increased slightly as the velocity increased, while the moment strain gauges experienced virtually no change in resistance. The drag behaved as expected on the sting, increasing proportionally to the velocity squared, while the lift increase on the sting was relatively constant with the exception of the 12.5 meter per second velocity set point. The lift and drag masses were subtracted from the final computed values to yield the correct values of lift and drag in mN. Table 5.2 includes these masses for each velocity on just the sting.

| <b>Velocity (m/s)</b>       | <b>5</b> | <b>7.5</b> | <b>10</b> | <b>12.5</b> |
|-----------------------------|----------|------------|-----------|-------------|
| <b>Drag from sting (g.)</b> | 1.36     | 3.33       | 6.17      | 10.15       |
| <b>Lift from sting (g.)</b> | 0.83     | 1.16       | 1.57      | 5.9         |

Table 5.2 – Sting drag and lift with no other test specimen attached during testing

### 5.3 Data Coefficients

With  $L_{Tot}$ ,  $M_{1/4c}$  and  $D_{net}$  known, the coefficients of lift, drag, and moment were able to be solved using

$$C_L = \frac{2L_{Tot}}{\rho V^2 S} \quad (11)$$

$$C_D = \frac{2D_{net}}{\rho V^2 S} \quad (12)$$

$$C_{M_{1/4c}} = \frac{2M_{1/4c}}{\rho V^2 S c} \quad (13)$$

The coefficient of lift, drag, moment and lift to drag ratio were then plotted versus the angle of attack for all wing data. A coefficient of lift versus angle of attack curve is

shown below, in figure 5.2, for the 8300 elliptical flexible wing with winglets and shows a wing stall at approximately sixteen degrees with a maximum lift coefficient of 1.7. The rest of the wing data can be viewed in appendix A.

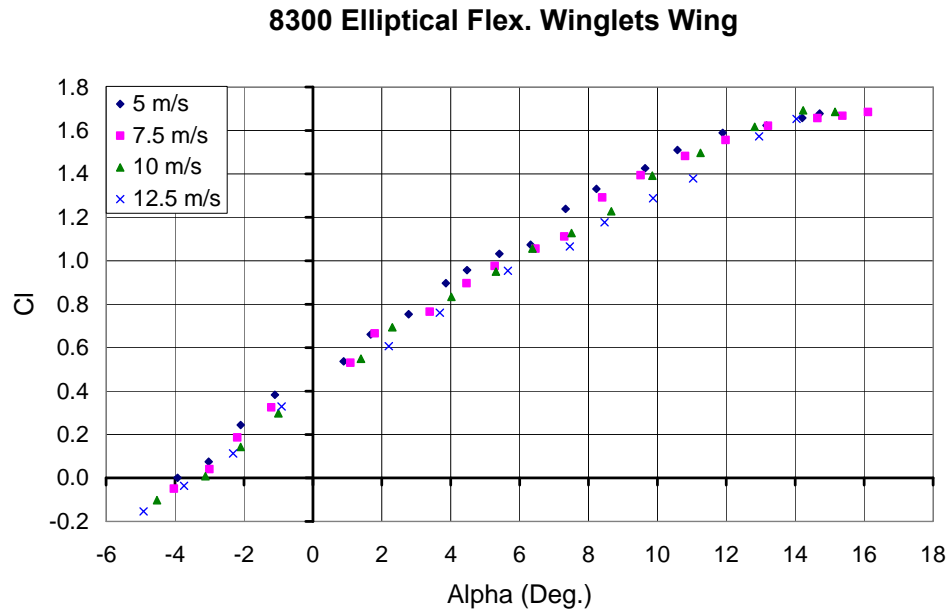


Figure 5.2 – Wing 4,  $C_l$  vs. alpha data

The chosen wings for the aircraft testing were the 8300 elliptical flexible and 8300 rectangular flexible winglets wings (Wings 0 and 4), as these two showed high lift, and lift to drag ratio values. The 8300 rigid rectangular wing showed a higher maximum lift coefficient, but was not used as rigid wings were not used on the micro air vehicles.

Fuselages B and C as well as the one piece tail, shown in figure 3.3, were used for this testing. Figure 5.3 shows fuselage C connected to the 8300 rectangular flexible wing, and was one of the aircraft used in testing.



Figure 5.3 - Final assembled aircraft: Fuselage C, Wing 0 (CW0)

Calculations proceeded in much the same way as that for the wings, with changes only in the moment arm calculations. Similar plots of the coefficient of lift, drag, moment, and lift to drag ratio were plotted versus angle of attack. In two cases aircraft stall was not reached due to vibrations on the apparatus, including aircrafts BW0 and CW0. The coefficient of lift versus angle of attack curve is shown below in figure 5.4 for aircraft BW0, showing that the aircraft approached the stall angle at about 18 degrees.

### Fuselage B, Wing 0

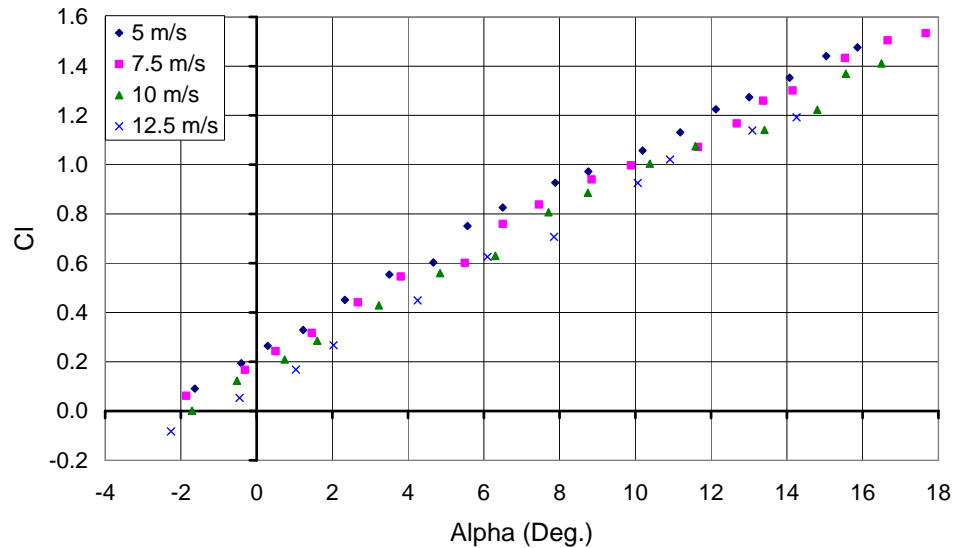


Figure 5.4 - Fuselage B, Wing 0 (BW0),  $C_L$  vs. alpha data

### 5.4 Flat Plate Testing

In addition to wing and aircraft testing, a flat plate with planform dimensions of 16 by 6 inches was made and tested as a comparison to the wing data and theory. The flat plate was constructed out of 0.080 inches thick woven carbon fiber in all areas to prevent bending from aerodynamic loads. As there is no camber to a flat plate, it would act as a symmetric airfoil with respect to lift. The two dimensional theoretical coefficient of lift versus alpha (angle of attack) curve was

$$C_L = 2\pi\alpha \quad (14)$$

where  $\alpha$  is in radians.

As seen in figure 5.5, there were slight differences between the theory and experimental data. A flat plate will also typically stall at around ten degrees (Mueller 1999), whereas this data suggests a stall angle around fourteen degrees. There are other

sources however that show LAR flat plates stalling closer to fourteen degrees (Pelletier and Mueller 2000), indicating that only the slope of the flat plate experimental data was problematic. Reasons as to why the flat plate data varied from the theoretical values are discussed in chapter 7.

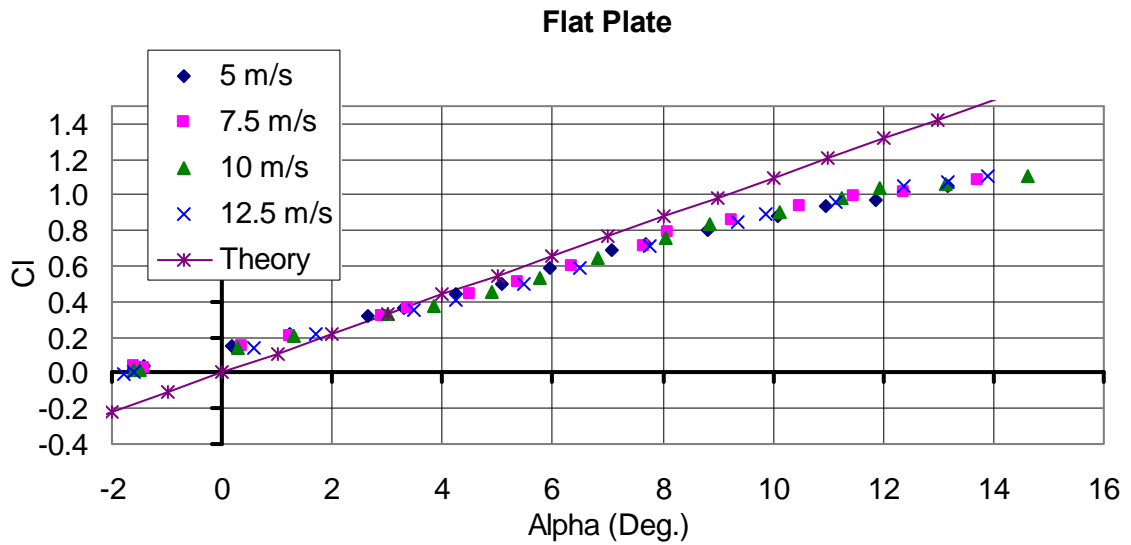


Figure 5.5 - Flat plate (FP),  $C_l$  vs. alpha data, comparison to theory

## CHAPTER VI

### ERROR ANALYSIS

#### 6.1 General

An error analysis was completed on the wind tunnel instrumentation and the coefficients of lift, drag, and moment. Variables with error included the moment arms, strain gauge voltage values, velocity, density, temperature, pressure, and planform area. There was error in the planform area due to the carbon fiber or epoxy spreading during the fabrication and baking process. Density values were seen to slightly fluctuate during the testing due to the changing room conditions, as they were not recorded for each individual test. The velocity was within a specified tolerance such that a steady wind tunnel motor rpm could be maintained while vibrations and electronic noise contributed to the strain gauge errors. For the instrumentation, the pressure transducer had a 0.12% reading error, while the temperature sensor fluctuated by  $\pm 1.5$  degrees Celsius, increasing the error in the velocity and density, respectively. The instrumentation errors were calculated first and added into the total errors of the coefficients as necessary.

#### 6.2 Instrumentation Errors

A pressure transducer and temperature sensor were used to calibrate the wind tunnel velocity, using Bernoulli's equation for a streamline and the ideal gas law. For the pressure transducer error, the highest change in pressure for the specified velocity was assumed, such that the error from the transducer would be greatest for that specified

velocity. Table 6.1 shows the maximum change in pressure for each velocity set-point on the wind tunnel control.

| Velocity (m/s) | $\Delta P$ (torr) | $\Delta P$ (N/m <sup>2</sup> ) | .12% Error (N/m <sup>2</sup> ) |
|----------------|-------------------|--------------------------------|--------------------------------|
| 5.0            | 0.11              | 14.67                          | 0.018                          |
| 7.5            | 0.24              | 32.00                          | 0.038                          |
| 10.0           | 0.445             | 59.39                          | 0.071                          |
| 12.5           | 0.7               | 93.33                          | 0.112                          |

Table 6.1 – Maximum pressure change for specified velocity set-point

For the error in density due to the temperature and pressure, partial derivatives were carried out onto the ideal gas law where

$$\rho = \frac{P}{RT} \quad (15)$$

The total error of the density, below, included the density tolerance based on the changing room conditions throughout the testing. Temperature and pressure errors were included from the instrumentation as well.

$$\delta\rho^2 = \left(\frac{\partial\rho}{\partial T}\right)^2 * (\delta T)^2 + \left(\frac{\partial\rho}{\partial P}\right)^2 * (\delta P)^2 + (\delta\rho_{tol})^2 \quad (16)$$

The velocity error was then calculated using Bernoulli's equation for a streamline, with density, pressure, and velocity tolerance errors. The velocity tolerance for guiding the wind tunnel motor rpm was set at  $\pm 0.1$  meters per second.

$$V = \sqrt{\frac{2\Delta P}{\rho}} \quad (17)$$

The total error for the velocity was then

$$\delta V^2 = \left(\frac{\partial V}{\partial(\Delta P)}\right)^2 * (\delta\Delta P)^2 + \left(\frac{\partial V}{\partial\rho}\right)^2 * (\delta\rho)^2 + (\delta V_{tol})^2 \quad (18)$$

The error in the density due to the instrumentation was calculated to be .001 kilograms per meter cubed, while the velocity error due to the instrumentation varied based on the velocity set point, reaching a maximum error at 12.5 meters per second of  $\pm.049$  meters per second. All equations used to calculate the total error in density and velocity, as well as all error analysis equations can be found in appendix E.

### 6.3 Data Coefficient Errors

With the total errors of density and velocity calculated, the errors in the coefficients of lift, drag, and moment could be computed. Errors that were constant for each wing or aircraft included the planform area and density, while the velocity, moment arms, and strain gauge readings varied for each datum point collected.

The first step in computing these errors was to find the error with respect to the variable considered. In order to do this, partial derivatives were taken of the equations for the coefficients to solve for the errors. The lift coefficient was considered first, as it had no dependency on the moment or drag deviations. Drag was dependent upon the error in the lift due to the coupling while the moment required both the lift and drag errors for the moment error contributions from each. Considering equation (11) for the coefficient of lift, the partial derivatives were

$$\frac{\partial C_L}{\partial L_{Tot}} = \frac{2}{\rho V^2 S} \quad (19)$$

$$\frac{\partial C_L}{\partial \rho} = -\frac{2L_{Tot}}{\rho^2 V^2 S} \quad (20)$$

$$\frac{\partial C_L}{\partial V} = -\frac{4L_{Tot}}{\rho^2 V^3 S} \quad (21)$$

$$\frac{\partial C_L}{\partial S} = -\frac{2L_{Tot}}{\rho V^2 S^2} \quad (22)$$

Since the net lift consisted of both the lift generated and the weight, two errors were applied, as there was an error in the strain gauge at both the velocity tested and the zero velocity value. For lift the general equation used was equation (4), as noted in section 4.1. The partial derivatives in lift were thus

$$\frac{\partial L_{Tot}}{\partial X_L} = g \quad (23)$$

$$\frac{\partial L_{Tot}}{\partial X_{L_{v=0}}} = -g \quad (24)$$

With the assumption that  $\partial x \approx \delta x$  where  $\partial x$  is the partial derivative and  $\delta x$  is the error in  $x$ , then all the partials can be squared and added together to solve for the error in the lift and then the coefficient of lift. This assumption can be made owing to the individually small errors present for each variable.

$$\delta L_{Tot}^2 = \left( \frac{\partial L_{Tot}}{\partial X_L} \right)^2 * (\delta X_L)^2 + \left( \frac{\partial L}{\partial X_{L_{v=0}}} \right)^2 * (\delta X_{L_{v=0}})^2 \quad (25)$$

$$\delta C_L^2 = \left( \frac{\partial C_L}{\partial L_{Tot}} \right)^2 * (\delta L_{Tot})^2 + \left( \frac{\partial C_L}{\partial \rho} \right)^2 * (\delta \rho)^2 + \left( \frac{\partial C_L}{\partial V} \right)^2 * (\delta V)^2 + \left( \frac{\partial C_L}{\partial S} \right)^2 * (\delta S)^2 \quad (26)$$

The coefficient of drag was calculated in a similar way, with the mass of drag defined in section 4.1 with equation (7). Using the same process of partial derivatives, the errors with respect to planform area, velocity, drag, and density were calculated for the coefficient of drag. The error in the drag consisted of the coupled lift, the error in the

drag for the velocity tested, as well as the zero velocity error. The error in the drag was then

$$\delta D_{\text{net}}^2 = \left( \frac{\partial D_{\text{net}}}{\partial V_D} \right)^2 (\delta V_D)^2 + \left( \frac{\partial D_{\text{net}}}{\partial V_{D_{V=0}}} \right)^2 (\delta V_{D_{V=0}})^2 + \left( \frac{\partial D_{\text{net}}}{\partial L_{\text{Tot}}} \right)^2 (\delta L_{\text{Tot}})^2 \quad (27)$$

Using the above error in the drag, the total error in the coefficient of drag was calculated and is included in the appendix as equation (28).

There were four sources of moments on the wings and aircraft at all times. This includes the aerodynamic moment, the moment due to lift and drag, and the moment due to the weight. These moments were evaluated about the moment strain gauge center in order to solve for the moment about the quarter chord. The resulting moment was

$$M_{1/4c} = M_{\text{sg}} - M_L - M_D - M_W \quad (29)$$

where  $M_{\text{sg}}$  was the resultant moment about the strain gauges, while  $M_L$  and  $M_D$  were the moments due to lift and drag at the quarter chord point on the wing. Each of these four moments contained errors due to the strain gauge readings and varying moment arm lengths. The error in the resultant moment was

$$\delta M_{\text{sg}}^2 = \left( \frac{\partial M_{\text{sg}}}{\partial \varphi_{\text{sg}}} \right)^2 (\delta \varphi_{\text{sg}})^2 \quad (30)$$

where  $\varphi_{\text{sg}}$  was the effective weight from the moment strain gauges at the calibration point. Both the resultant moment and the moment due to the weight were calculated using the effective weight which was converted to a moment in further calculations to ensure that the correct calibration distance was applied for the moment. For example, the weight of the wing was a distance “a” away from the moment strain gauges, but since the

calibration point was on the sting at the most forward 8-32 threaded hole, an effective weight was used, as below. The calibrated moment and the actual moment were thus the same.

$$Wa = x_w * W_{eff} \quad (31)$$

The partials of the resultant moment and moment due to weight were thus the distance from the moment strain gauges to the calibration point, a constant moment arm.

The error in the moment due to weight was then

$$\delta M_w^2 = \left( \frac{\partial M_w}{\partial W} \right)^2 * (\delta W)^2 \quad (32)$$

The moments due to lift and drag contained both a varying force and moment arm length, and were calculated as

$$\delta M_L^2 = \left( \frac{\partial M_L}{\partial X_L} \right)^2 * (\delta X_L)^2 + \left( \frac{\partial M_L}{\partial L_{Tot}} \right)^2 * (\delta L_{Tot})^2 \quad (33)$$

and

$$\delta M_D^2 = \left( \frac{\partial M_D}{\partial X_D} \right)^2 * (\delta X_D)^2 + \left( \frac{\partial M_D}{\partial D_{net}} \right)^2 * (\delta D_{net})^2 \quad (34)$$

All the moment errors due to the strain gauge and moment arms were thus calculated, and the total moment about the quarter chord could be computed using equation (29). Since all the partials of the moment about the quarter chord were  $\pm 1$ , as below,

$$\frac{\partial M}{\partial M_{sg}} = \frac{\partial M}{\partial M_w} = \frac{\partial M}{\partial M_L} = \frac{\partial M}{\partial M_D} = \pm 1 \quad (35)$$

the total error in the moment was then

$$\delta M^2 = \delta M_{sg}^2 + \delta M_w^2 + \delta M_L^2 + \delta M_D^2 \quad (36)$$

The error in the coefficient of moment was calculated in a similar manner to that of the coefficients of drag and lift, and is included in the appendix as equation (45). It was assumed that the variation in the chord length,  $c$ , was accounted for in the planform error on the wing and did not add to the error. Therefore the variables were the same as the lift and drag coefficient when completing the analysis.

#### 6.4 Angle of Attack Error

In addition to the error in the coefficients of lift, drag and moment, there was an error in the angle of attack due to several factors. 1. The vibrations on the wing yielded a changing angle of attack throughout the tests, thus two pictures would likely result in different angles of attack. 2. As the angle of attack was determined by manual image processing, there was an error in pixel selection. 3. The angle of attack changed with respect to a weight or lift force applied, due to an AoA change in the sting and adapters.

In order to remedy the first two cases, six pictures were taken of the wing at the same AoA and velocity during testing where vibrations were highest. Vibrations were considered high when the amplitude at the LE was approximately 2-3 mm. Angles were computed and averaged, yielding a more accurate account of the AoA as well as a standard deviation in the angle. This error was then averaged among all testing for wings and aircraft to yield an average error in angle of attack, applied to each datum point.

The standard deviation of these angles of attack was then converted to a pixel standard deviation. For this conversion, a single point was selected for the TE and LE of a wing image, and the “true” angle computed. The pixel above the first LE point was then selected, in order to determine a simulated error for a vertical pixel selection. The

same was done for two and three pixels of error vertically, as well as up to three pixels of error horizontally. These angle of attack changes were then compared to the standard deviation of the actual angle of attack computed. The standard deviation in pixels was determined to be approximately 2-3 for all wings and aircraft at high angles of attack or high velocity. The average error in the angle of attack was between 0.2-0.3 degrees.

The angle of attack change due to the lift or weight on the sting is discussed in section 7.5

## 6.5 Error Results and Contributions

Once error calculations were completed, results were analyzed in terms of the magnitude of error in the coefficients and instrumentation as well as the percentage contributions to each error based on the individual variables. Percentage errors for the instrumentation were calculated based on the actual value used for the variable considered. Percentage errors for the coefficients were compared to the total error in the coefficient considered. There were also errors in the apparatus that were not accounted for, as they could not be readily calculated.

The contributions to the instrumentation error varied widely. The percentage error from the true value in the velocity due to the pressure was around 0.3%, while the density accounted for up to 32.5% of the error at a 12.5 meter per second velocity. This large error in the density is due to the tolerance allowed from varying room conditions throughout testing. The percentage error in the density due to the temperature was 4.1% while the pressure error was 0.26% of the total density. The rest of the contributing errors in velocity and density were the tolerances placed on them; the tolerance of the

velocity was based on the Labview program for the motor rpm. The total density error was 0.021 kilograms per meter cubed while the total velocity errors were 0.109 meters per second for a 5 meter per second tunnel velocity and up to 0.149 meters per second for a 12.5 meter per second velocity.

From the errors in the coefficients of the system, it was noted that the velocity, strain gauge, and moment arm errors were the largest contributions to the error. For the wing data lift coefficient, the total average percentage error of the velocity and strain gauges was 43.8% and 42.0%, respectively, while the other 14% was from density and planform area errors. For the coefficient of drag, the percentage velocity error was 5.4%, while the strain gauges accounted 92.9%. The strain gauge and moment arm errors together accounted for approximately 99.9% of the total error for the moment coefficient for both the wing and aircraft data. The aircraft data errors showed similar results for both the coefficient of lift and drag in terms of percentage contributions. The velocity and strain gauge percentage errors accounted for 52.3% and 29.4% respectively, for the coefficient of lift, while the velocity and strain gauge percentage errors were 6.5% and 91.0% for the coefficient of drag.

The errors in the setup that were not accounted for primarily resided in the error in the wing mounting, whether it was a wing offset, roll, or yaw, but not detectable to the naked eye. Figures 6.1 - 6.3 show some of these inconsistencies that were not accounted for. The wind tunnel test section angle might have varied slightly as the section was mounted on four air pads that required daily air input. The sting, although eyed as well as possible with T-squares, levels, and rulers, might have been slightly off as well. All these errors were however considered small and negligible as the wing and aircraft

placement were adjusted as necessary to be parallel to the incoming airflow. Otherwise, these errors could not be readily calculated.

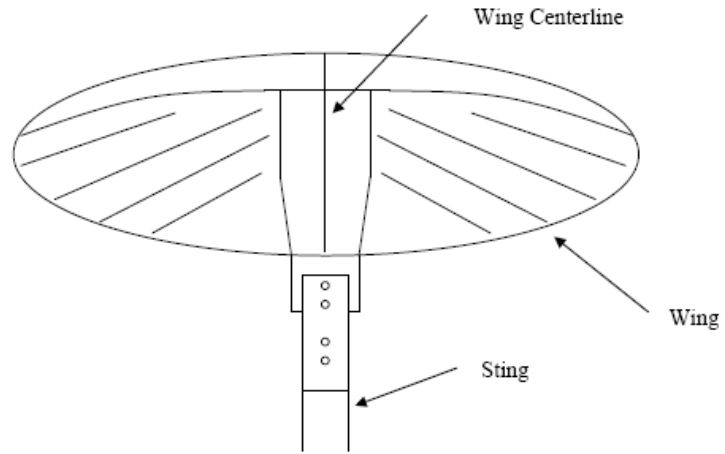


Figure 6.1 – Correctly centered wing on sting apparatus (top view)

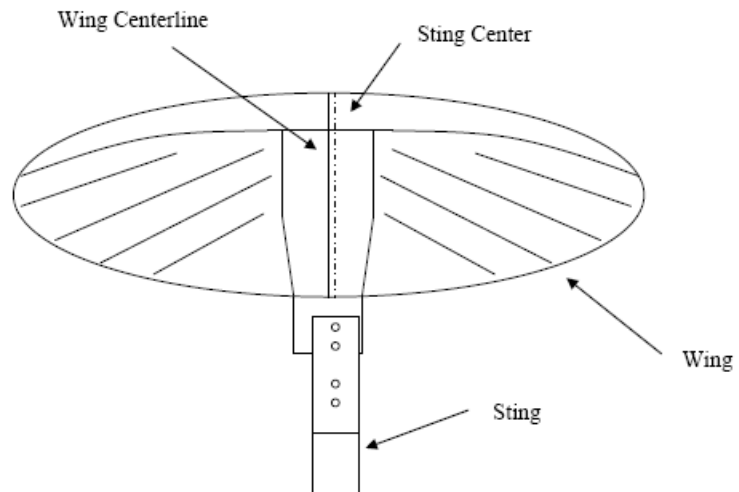


Figure 6.2 – Wing offset on sting apparatus (exaggerated offset)

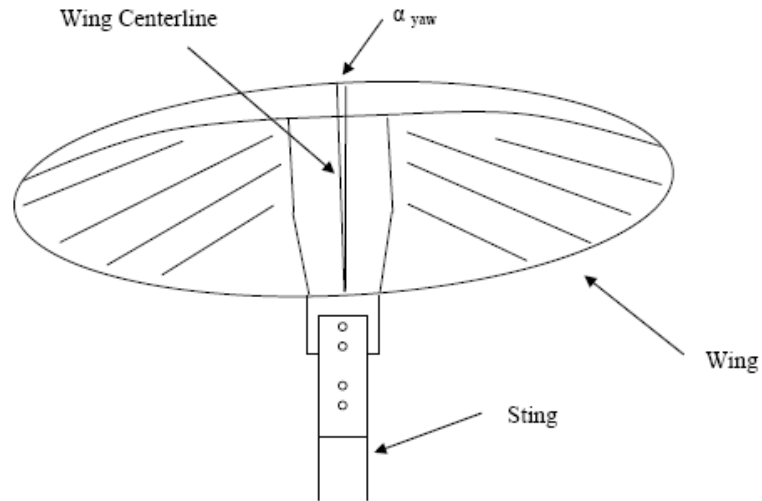


Figure 6.3 – Wing yaw on sting apparatus (exaggerated yaw)

A comparison between the aircraft and wing moment error showed the aircraft error larger than that for the wings. This was primarily due to the larger vibrations on the aircraft; the average moment error for aircraft BW0 moment coefficient was 0.046 while the average error in Wing 0 was only 0.037.

In terms of the overall error for all data, the average angle of attack error ranged from 0.2 degrees at low angles of attack and velocities, to 0.3 degrees at high angles and velocities. For both wings and aircraft, the error in the coefficient of lift, drag and moment ranged from  $\pm 0.01$  to  $\pm 0.02$  at low angles of attack and were as high as  $\pm 0.15$  at high angles of attack. The larger errors seen at higher angles of attack are typical for wind tunnel setups (Rae and Pope 1984) as there is flow separation and turbulence at stall, which may induce vibrations. Several graphs are included in appendix B that show Wing 0 and aircraft BW0 with error bars included.

## CHAPTER VII

### DISCUSSION OF RESULTS

#### 7.1 General Results

The results of the wing and aircraft testing were compiled and inspected to determine any inconsistencies in the data. The data did show trends for each specimen tested: The coefficient of lift varied linearly with angle of attack for all data and the zero lift angle of attack for all wings was also negative by several degrees, which is normal for a positively cambered airfoil. Drag data indicated an exponentially increasing coefficient of drag with respect to angle of attack. This shows the possibility of a drag coefficient proportional to the square of the coefficient of lift.

All moment coefficients were found to be negative, which was also expected based upon the positive wing curvature. In some cases, as for Wing 4, there were regions where the moment coefficient was approximately constant, meaning that the  $\frac{1}{4}$  chord point on the wing was the aerodynamic center. Other data showed a downward sloping moment coefficient, indicating that the aerodynamic center for the wing or aircraft was forward of the  $\frac{1}{4}$  chord point.

All data fell into reasonable values for the coefficients of lift, drag and moment. Maximum coefficients of lift varied from 1.2 to 1.7 on wings and 1.2 to 2.0 for aircraft. The drag coefficients around the stall angle ranged from 0.3 to 0.5 for all data, while the moment coefficients ranged from 0.1 down to -0.5 across all angles of attack tested.

## 7.2 Drag Comparison: Wing and Aircraft

While the basic parabolic trends for the drag coefficient were seen for the wings and aircraft data, the specific comparisons showed some unique characteristics. At low angles of attack, the drag on the aircraft was about 50% more than that on the wing. At high angles of attack however, the coefficient of drag on the wing was higher than that of the aircraft, as seen in figure 7.1. The inflection point where the wing drag was higher than that of the aircraft occurred in the range of 8 to 10 degrees, depending on the wing and aircraft comparison. It was noted that this trend occurred between all comparisons of the aircraft and their respectively attached wing.

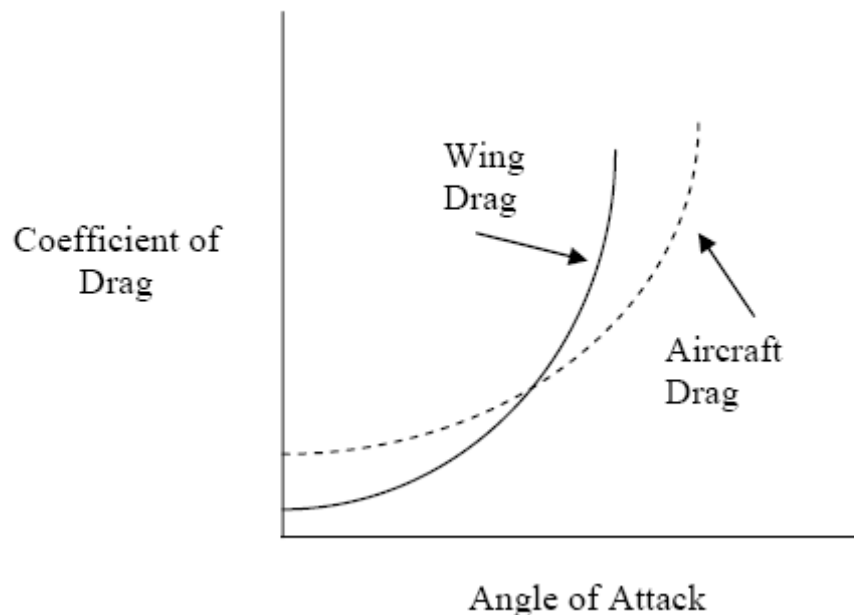


Figure 7.1 – Typical coefficient of drag difference between wing and aircraft data

In general it would be expected that the aircraft drag would be greater than the wing drag for all angles of attack, based upon the blunt fuselage obstructing the airflow around the wing. The form drag on the aircraft should be greater than that of the form

and interference drag on the wing. However it was determined that this difference in the drag was due to an increased flow separation along the wing at the higher angles of attack, whereas for the aircraft the flow was still attached. The fuselage also spanned approximately 10-15% of the wing, covering that portion of the knife-edge leading edge and the rigid midsection. Hypothetically, this type of leading edge may not allow for a clear stagnation point at the front of the wing, and therefore create flow separation that would otherwise not be present on a thicker and well rounded wing. Since this flow separation for the LE and rigid midsection would lead to higher drag, it was concluded that this was the most likely cause for the differences in the aircraft and wing coefficients of drag. Although the fuselage placed a blunt object directly in front of the wing, at higher angles of attack the flow on the sides would be streamlined, not adding to the drag due to flow separation that was seen on the wings.

### 7.3 Video Analysis: UF Data

Throughout the data collection and analysis it was realized that there were certain regions where drag and moment characteristics did not follow the general curve for that particular set of wing data. It was clear that this occurred for all the UF wings in a specific region of angles of attack at low velocities, while no NACA 8300 airfoils were affected by these disparities. Data was first retaken to determine whether these inconsistencies were due to a fault in testing, or represented the true data.

This testing covered the possible scenarios leading to why the data was unexpected in the first place. These scenarios were 1. All the retaken wing data would be the same as it was as with the previous testing and the wings thus went through an

aerodynamic transition for the angle range in question. 2. The wing data that was unexpected would correct itself through further testing, and no more analysis was needed. 3. The data that was deemed correct would change to match that of what was thought to be incorrect, leading to retaking all wing and aircraft data.

Data was retaken for wings 1, 2, and 6 at adapter angles of 2 and 5, corresponding to the data in question, to test for any changes in the large drag coefficients. These wings were also tested at 8 and 10 degree adapter angles, where the data was not in question, to determine if the data that was thought to be correct would change and match the unexpected trends.

The additional testing was completed for all velocities and it was found that the first scenario was true; all data points retaken were relatively the same as before, within error bounds. The coefficient of drag remained at values much higher than that of the rest of the respective data curve, as with the UF Rigid Rectangular wing (See figure 7.2).

## UF Rigid Rectangular Wing

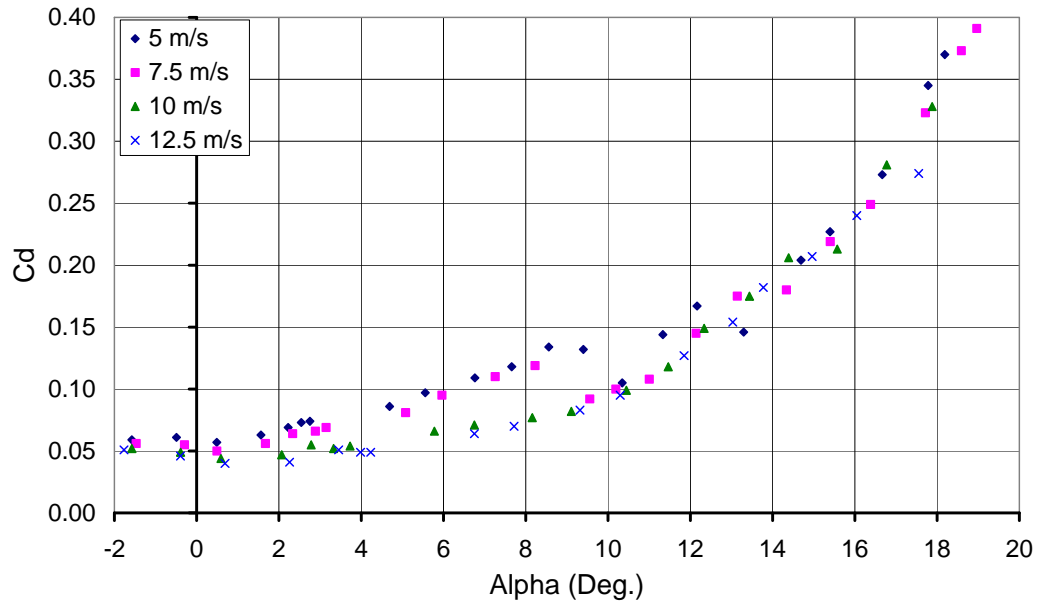


Figure 7.2 – Wing 2,  $C_d$  vs. alpha data; shows unexpected coefficient of drag values for 5, 7.5 meter per second data

A new method was needed to determine why the data did not match up for the UF wings for the 5 and 7.5 meter per second data versus the 10 and 12.5 meter per second data. In order to accomplish this, a qualitative video analysis would show any adverse flow characteristics on these wings. These types of tests are generally done for either normal flow visualization, or with the addition of strings, coatings, or other material, are used for roughness factor tests (Rae and Pope 1984). Two wings were chosen for the analysis; the UF rigid wing with unexpected data at 5 and 7.5 meters per second, and the 8300 rigid wing. Thin threads were glued in systematic locations on the top of both wings (Fig. 7.3). As few threads were attached to the wings, it would show the flow effects but not affect the roughness of the wings. The wind tunnel was covered in black cloth and a black light placed in the upper left corner inside the test section. The threads

on the wings were colored with a UV marker such that they could be seen clearly with the black light on. A video camera was set up outside of the test section, viewing through a one foot by one foot acrylic section, and down onto the wing at a slight angle.

The UF wing was tested at 3 different angles of attack while the 8300 wing was tested at 4. The three angles tested for the UF wing included two angles that would result in the region of unexpected data, at 2 and 5 degree adapters, while the final angle adapter was at 8 degrees, resulting in a region beyond that of the unexpected data. The first three angles used for the 8300 wing corresponded to the resulting angles of the UF wing; adapter angles of 2, 4, and 6 were used. The final adapter used was 13 degrees, in order to reach a stalling angle of attack on the 8300 wing. All angles of attack tested were conducted at all the regular test velocities of 5, 7.5, 10 and 12.5 meters per second. To aid in describing how the threads reacted to the incoming airflow, they were labeled and used for the 8300 and UF wing flow descriptions.

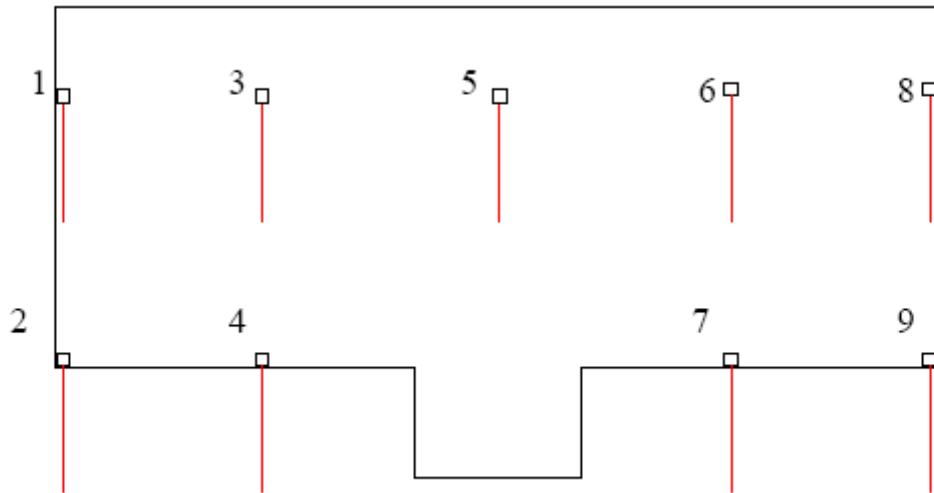


Figure 7.3 – Wings with numbered threads designated for flow analysis

For the UF wing with a two degree adapter angle attached at 5 meters per second, threads 1 and 8 showed the vortices shed off the wing tips. All threads attached at the trailing edge lifted slightly from the flow around the wing but did not shed vortices. Threads 3, 5, and 6 however wrapped forward, toward the leading edge of the wing. This exact scenario occurred for the 7.5 meter per second video as well. The 10 and 12.5 meter per second data however showed a change; threads 3, 5, and 6 all straightened back out like the trailing edge threads. Figure 7.4 shows the reactions to the incoming airflow for the lower velocities while figure 7.3 displays the thread reactions at the higher velocities. Similar reactions occurred using the five degree adapter for the UF wing as with the two degree adapter, both of which covered the unexpected data in the regions of interest for the drag coefficient.

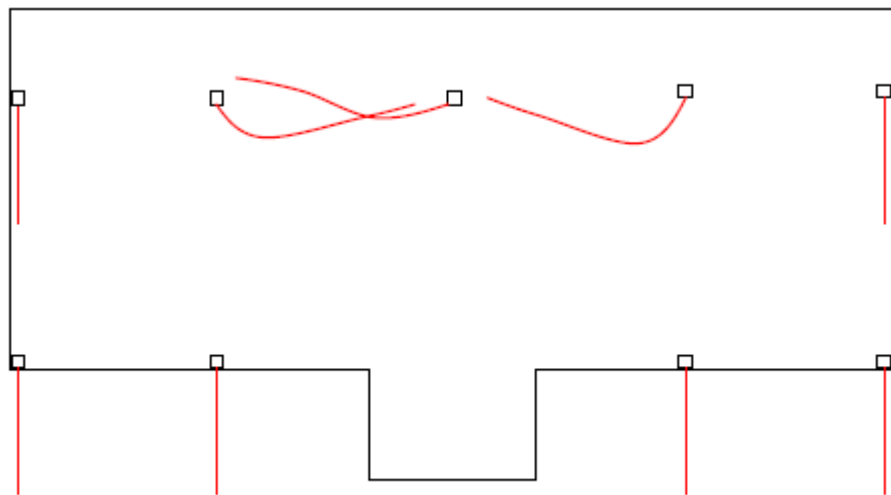


Figure 7.4 – Comparison of airflow around UF wing (5, 7.5 meters per second, low angles of attack)

The video analysis on the UF wing for the eight degree adapter showed different results. For all velocities tested, the wing tip threads shed vortices, however the central

threads, 3, 5, and 6, all fell straight back. This indicated that there was no adverse flow separation or other drag effects in the regions of correct data trends for the drag coefficient. The 12.5 meter per second data results were slightly different in that the central threads, 3, 5, and 6 displayed some signs of flow separation as they fluttered slightly. However this was expected, since the wing was at a stalling point.

The 8300 rigid wing was tested in the same manner as the UF wing. For the 2, 4, and 6 degree adapters all threads fell straight back along the wing at all velocities with the exception of the wing tips, which shed vortices. Since the central threads did not move much at these adapter angles, the higher angle test with the 13 degree adapter ensured that there was nothing wrong with the setup. The results of the 13 degree adapter showed stalling effects along the wing at velocities of 10 and 12.5 meters per second; the central threads exhibited signs of flow separation.

Through the video analysis it was concluded that the unexpected data on all the UF wings was due to three possibilities. 1. Flow separation on the wing. 2. A stagnation point on the top of the wing rather than the leading edge. 3. Laminar separation bubbles forming on the top of the wing at particular angles of attack and Reynolds numbers.

A couple hypotheses were made as to why this occurred on the wing at these low velocities. The curvature on the UF wing was high in the front half of the airfoil. This rapid change in curvature could act as a barrier instead of allowing the airflow to be continuous along the airfoil. The Reynolds number is also in a  $10^4$  region at the lower velocities, where it was likely the wing would be in a transitional flow phase (Nechyba and Ifju 2002; Mueller and DeLaurier 2003). At the higher velocities of 10 and 12.5

meters per second, the Reynolds number would be bumped back to a  $10^5$  region, likely in a more stable flow region. Although in a possibly turbulent region, the flow characteristics would follow that of the rest of the data trends and the assumed correct values.

A moving stagnation point on the wing with respect to the angle of attack and incoming velocity would shift the pressure difference on the wing. The knife-edge leading edge could prevent a clear location affected by a transition in the flow. The stagnation point may be on the top of the wing in the region of high drag, but move to a location below the wing once past a particularly high angle of attack or be subjected to a flow transition.

Along the lines of seeing a flow transition occur, laminar separation bubbles may be developing due to the low Reynolds numbers and high amount of curvature change on the UF wings. These separation bubbles appear when there is boundary layer separation, a flow transition, or turbulent reattachment of the flow, typically at low Reynolds numbers (Mueller and DeLaurier 2003; Rist et al. 1996). They ultimately lead to unsteady forces on the test subject. Within the bubble there exists some recirculation in the flow, and may be the reason for the strings on the UF wing to flip forward to the LE of the wing. They would subsequently be caught in the “dead air” region in the bubble (See figure 7.5).

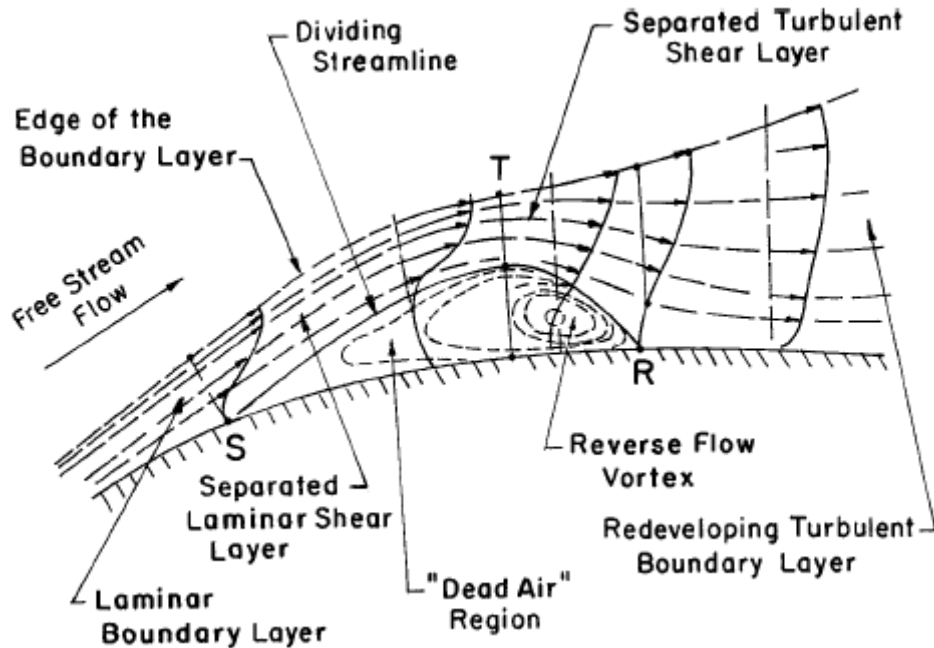


Figure 7.5 – Laminar Separation Bubble for time averaged features (Mueller and DeLaurier 2003)

The results of the video tests indicate the formation of laminar separation bubbles, however more complete tests would be needed to determine whether this was the actual case. More advanced flow techniques such as smoke fields may be required, but were not conducted for this experiment.

#### 7.4 Select Coefficient of Lift versus Alpha Data

Upon further comparison between the flexible wing data and other rigid wings it was seen that the angle of attack stall range on all tested wings was larger than that normally seen (Olson et al. 2005; Ifju et al. 2002). These larger AoA stall effects on all the data may be due to the sting vibrations and subsequent damper effects at these high angles of attack. The adapter angle forces the wing or aircraft into a particular position

and that position changed based on the incoming velocity. The specimen angle of attack was held down by the damper while it reduced the vibrations to allow for a constant applied lift force. The damper in effect allows for a higher angle of attack to be reached while maintaining a high lift force, and thus the larger stall AoA range.

There are many cases however where the AoA range for stall is quite large, negating the large AoA range deficiencies in the lift data. This is typical of wings tested at relatively low Reynolds numbers, around  $10^4$  and  $10^5$  (Ifju et al. 2002; Pelletier and Mueller 2000). Parabolic lift curves are even inherent to LAR wings as suggested by the University of Arizona, among others (Olson et al. 2005; Ifju et al. 2002). There may still be inaccuracies from the vibrations in the system, but due to the multitude of data confirming smooth and long stall curves, the tested wings were determined to have sufficiently good results for this aspect.

It was also seen on several wings, including Wing 0 and 7, that the lift coefficient varied based upon the incoming velocity. The lower velocity yielded a higher coefficient of lift; however the slopes of the lift curves remained approximately the same. The differences between the 5 and 12.5 meter per second lift coefficient data varied by about 0.2 for the same recorded angle of attack for several wings. Wing 0 was one of these test specimens and was tested multiple times to determine there was nothing inconsistent with the setup. The coefficient of lift was the only aerodynamic characteristic that deviated from varying velocity points for these test specimens. Since some of the wings and aircraft had looser flexible fabric wings, the combination of the AoA deflections from the sting and adapter and loose fabric may be the cause for the gaps in the coefficient of lift data. To give a perspective in the changes in the fabric deflections, the wings 0 and 7 had

deflections of  $\pm 1$  inch, while most of the other wings only had  $\pm 1/8$  inch deflections at their most flexible locations along the edges. The changing wing geometry due to the varying velocities thus may have contributed to the large gaps in the lift coefficient. Wings 0 and 7, among other test specimens, thus showed trends for the coefficient of lift, but not a consistent value, with the exception of the slope of the curves.

## 7.5 Sting and Adapter Deflections

Thus far it has been discussed that all the data was affected by the sting and adapter deflections, but it has not determined whether these changes could be factored out. The lift coefficient data for the flat plate indicated unexpected results with the negative zero lift angle of attack. The shallow lift curve however was taken to be correct based upon the LAR, thin flat plate data from Pelletier and Mueller (Pelletier and Mueller 2000). As all other disparities and hysteresis in the data has been discussed, the sting and adapter deflections are the only other sources of unaccounted error.

An attempt was made to account for the error; the known forces on the sting as well as the true angle of attack and the adapter angle of attack were calculated, so all forces and angles could be solved for relating to the lift coefficient versus AoA. However a concern was that by accounting for this deflection, all the forces placed on the apparatus would be accounted for and thus be left with zero data. This case would be true if only the sting deflected based on the forces applied, yet with the adapter changes as well, calculations may have shown otherwise.

The logical path for calculations involved adjusting the angle of attack and recalculating for the correct data, however this followed a circular argument. The change

in deflection from the sting could be accounted for by subtracting or adding the angle of attack out, but this would mean changing the incoming flow angle of attack, and gravity vector. Adjusting the angle of attack back to its original state would yield the results gained in the first place.

The other possible reason for the unexpected data lied within the calibration data used for the forces on the test specimens. As seen from the flat plate lift data, if the slope of the conversion from volts to grams were skewed; the true calibration may yield the correct data. Calibration data was taken again at two positions (See figure 3.4); both the original calibration position and the new one (a point closer to the moment strain gauges) yielded the same results for the calibration data. Since this did not yield any difference in the data, there was no way to factor out these AoA changes from either the weight or lift on the test specimen. The data was therefore able to show the trends for each wing and aircraft tested, but not the correct results as the hysteresis effects of the sting and adapters could not be accounted in the calculations.

## 7.6 Electronics

During the initial setup of the wind tunnel tests, the strain gauge signals were not amplified in the DAQ card. This was not a concern until after all data was collected and the mechanical change in angle of attack could not be accounted for. Although amplifying the signal would do nothing to affect the data, further inspection of other works revealed that balance systems typical amplify the signal from the strain gauges. The strain gauges would be able to detect much smaller deflections in the sting, up to 100 times smaller than what they currently read. The sting and adapter attachments could

have thus been 100 times stiffer and would yield the same results, yet now there would be no mechanical change on the sting. Adapters on the other hand would need to be redesigned such that they did not deflect appreciably when a force was applied.

There were no problems in the electronics used and a list of the specifications for them is provided below in table 7.1.

| Item                   | Manufacturer              | Specifications   |
|------------------------|---------------------------|------------------|
| Strain Gauges          | Vishay Micro-Measurements | CEA-13-125UW-350 |
| Strain Gauge Amplifier | Pacific                   | Model 8250       |
| DAQ Card               | National Instruments      | Model SCXI-1305  |
| Labview                | Labview                   | Version 6.1      |
| Pressure Transducer    | MKS                       | Type 146         |
| Temperature Sensor     | OMEGA                     | Model DP119      |

Table 7.1 – Electronics Specifications for wind tunnel and sting apparatus

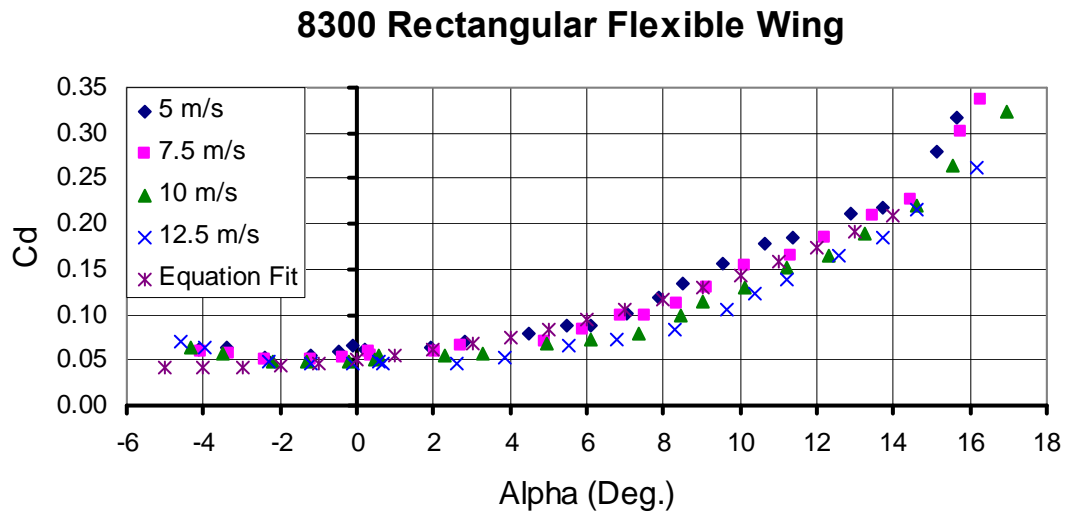
## 7.7 Equation Fits for Results

Linear fits were applied to the coefficient of lift and drag versus angle of attack data. These fits were useful to determine the slopes of the coefficient of lift versus the angle of attack, the zero lift angle of attack, and any relation between the lift and drag coefficient. They may also subsequently be used for aerodynamic performance measurements before flights and to perfect the aircraft construction.

In order to find the relation between lift and drag, it was assumed that the coefficient of drag was proportional to the square of the coefficient of lift. This is a typical way of characterizing this relation (Anderson 1999). The equation thus had the form,

$$C_d = C_{d_0} + K * C_L^2 \quad (37)$$

where  $C_{d_0}$  and  $K$  were the constants to be determined. A least squares fit method was used to determine these constants, using the known coefficients of drag and lift. The equation fit was used for only the regions where the drag coefficient was linear with respect to the square of the lift coefficient; regions near stall were not included. The plot of the coefficient of drag resulting from the equation onto the actual data for Wing 0 showed that these approximations did fit well to the data (See figure 7.6). The equation fits did break down near or at stall as well as near the zero lift angle of attack.



Figures 7.6 –Wing 0,  $C_d$  vs. alpha data with equation fit

The coefficient of lift lines did line up well for most data, with typical correlation coefficient values of 0.90 or higher, indicating a good fit. All equation fits completed were compiled and are included in table 7.2. This data represented the average fits among all velocities tested for each test specimen.

As some of the wings showed parabolic lift curves, such as Wings 4 and 9, they were fitted to a second order equation and are shown in table 7.3. The general equation used for determining these curve fits was

$$C_l = b_0 + b_1 * \alpha + b_2 * \alpha^2 \quad (38)$$

and has been used in previous works for LAR, low Reynolds number wings and aircraft (Olson 2005; Torres and Mueller 2000). R in table 7.3 refers to the correlation coefficient.

|               | <b>Zero Lift AoA (Deg.)</b> | <b>C<sub>l</sub> / Alpha (1/rad.)</b> | <b>C<sub>d0</sub></b> | <b>K</b> |
|---------------|-----------------------------|---------------------------------------|-----------------------|----------|
| <b>FP</b>     | -1.61                       | 0.47                                  | 0.005                 | 0.216    |
| <b>Wing 0</b> | -4.09                       | 0.54                                  | 0.042                 | 0.07     |
| <b>Wing 1</b> | -1.45                       | 0.49                                  | 0.04                  | 0.087    |
| <b>Wing 2</b> | -1.24                       | 0.52                                  | 0.047                 | 0.089    |
| <b>Wing 3</b> | -4.69                       | 0.56                                  | 0.049                 | 0.066    |
| <b>Wing 4</b> | -4.00                       | 0.63                                  | 0.047                 | 0.052    |
| <b>Wing 5</b> | -3.86                       | 0.56                                  | 0.041                 | 0.074    |
| <b>Wing 6</b> | -2.55                       | 0.47                                  | 0.042                 | 0.065    |
| <b>Wing 7</b> | -4.36                       | 0.52                                  | 0.043                 | 0.076    |
| <b>Wing 8</b> | -3.76                       | 0.54                                  | 0.031                 | 0.083    |
| <b>Wing 9</b> | -4.05                       | 0.44                                  | 0.024                 | 0.158    |
| <b>BW0</b>    | -2.40                       | 0.49                                  | 0.05                  | 0.11     |
| <b>BW4</b>    | -2.49                       | 0.48                                  | 0.058                 | 0.084    |
| <b>CW0</b>    | -1.69                       | 0.65                                  | 0.055                 | 0.09     |
| <b>CW4</b>    | -2.74                       | 0.57                                  | 0.067                 | 0.075    |

Table 7.2 – Equation Fits: All wing and aircraft

|               | <b>b0</b> | <b>b1</b> | <b>b2</b> | <b>R</b> |
|---------------|-----------|-----------|-----------|----------|
| <b>Wing 4</b> | 0.426     | 0.113     | -0.002    | 0.999    |
| <b>Wing 9</b> | 0.307     | 0.089     | -0.002    | 0.996    |

Table 7.3 – Parabolic Lift Curve Fits – Select Wings

## CHAPTER VIII

### CONCLUSIONS

#### 8.1 General

All data did not show the correct results for several reasons; the largest factor being the angle of attack change on the aircraft and wings due to the sting and adapter deflection. The method of clamping the test specimen also resulted in several errors in the system. With the wing or aircraft clamped using two screws, a certain amount of clearance was needed to put everything together. With that came errors in yaw, roll, and offsets on the specimen that deviated from the centerline as well as hysteresis during testing.

If the sting and adapters did not deflect to this high magnitude of 2-5 degrees, it was hypothesized that the data and theory for the flat plate would match up more consistently. A zero lift at zero degrees angle of attack would not only validate the flat plate data, but the rest of the wing and aircraft data. Without vibrations in the system, higher angles of attack could be achieved and clearer stall patterns recognized.

Although the data was not correct, it did show specific trends and allowed for an evaluation of MAV performances aerodynamically. Wing changes were made on the aircraft to allow for easier flight control, longer flight duration, and increased payload capacity.

## 8.2 Highlighted Results

The best performing wings were the 8300 elliptical flexible wing with winglets (Wing 4) and the 8300 rectangular flexible wing (Wing 0), with maximum coefficient of lifts at 1.68 and 1.50 respectively. The lift to drag ratio maximum for 8300 elliptical flexible wing with winglets was 12.5 at approximately 5.0 degrees angle of attack, while the maximum for the 8300 rectangular flexible wing was 11.5 at about 5.5 degrees angle of attack. Typical ranges for the maximum coefficient of lift were 1.2 to 1.8 for all wings. The maximum lift to drag ratios were approximately 9 to 12.5 for all wings.

Of the aircraft tested, fuselage C and the 8300 rectangular flexible wing (CW0) resulted in the best combination with a maximum coefficient of lift of 1.85 and lift to drag ratio of 8.2 at approximately 7.0 degrees.

## CHAPTER IX

### FUTURE WORK

#### 9.1 Sting and Testing Considerations

For further considerations on data collection on micro air vehicle platforms, a stiffer sting is required. Angle of attack deflections on the sting of 1-2 degrees with a force of 0.5 kilograms suggests rigidity, EI equivalent, of 3.4 Newton meters squared. This assumed a single load point at the front edge of the sting. The reduction in the angle of attack change by two or three orders of magnitude will result in better results for all further testing, as well as a large reduction in time required to collect the data, as no pictures would need to be taken to determine the angle of attack. Steel was considered an option for sting material, but as it has a modulus of elasticity of only three times as much as 6061 aluminum, a change in the sting dimensions would be needed (Gere 2001). Along the same order of magnitude in angle of attack deflection, the adapter angle changed with respect to the force placed on it. A more rigid connection to the sting and specimen would also be needed for better results.

While a re-machined sting and adapters would provide better results and decreased time for collection, the sting may be redesigned altogether to include yaw, roll, and side force. Full micro air vehicle testing could then be completed, as the moment produced by a propeller could be accounted for. This may be done by incorporating a 6-axis internal strain gauge balance into the design.

Another consideration for ease of data collection would be to redesign the sting to not only account for the added yaw, roll, and side force on a specimen, but to

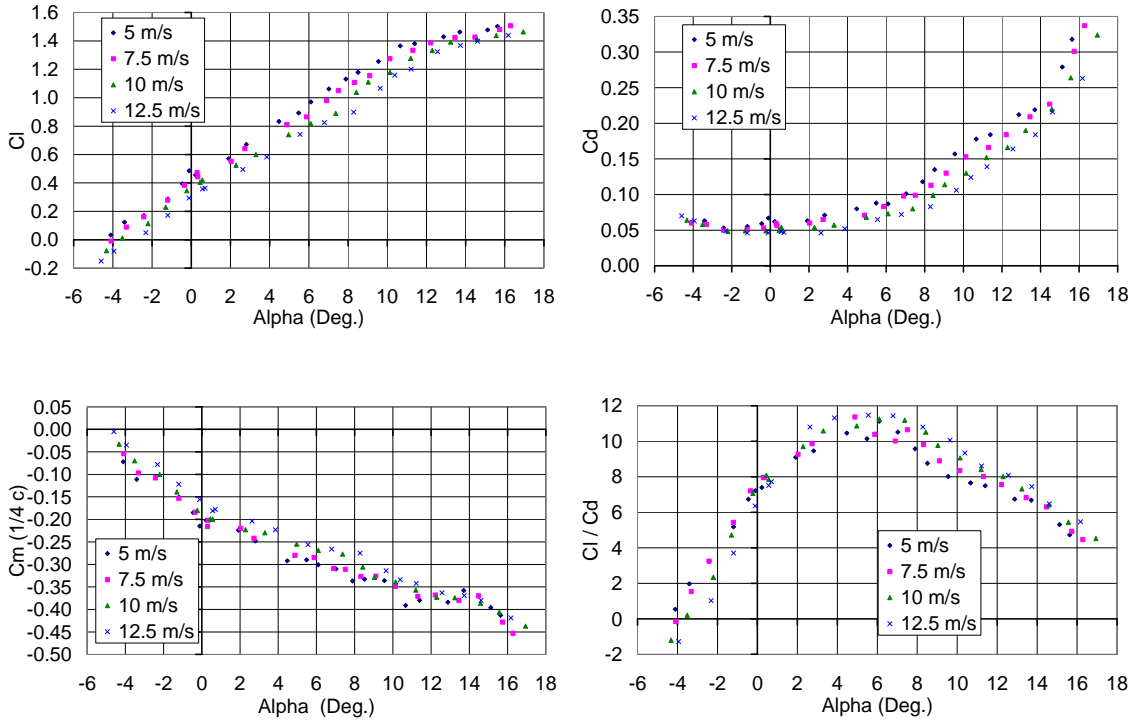
automatically adjust the angle of attack. A stepper motor could attach to a section of the sting that may rotate the entire apparatus. The stepper motor would be controlled by a program outside the wind tunnel, so a specimen can be tested for all ranges of angle of attack necessary before switched out to another.

In addition to the stepper motor, a method of attaching the specimens closer to the aerodynamic center would be very useful. This would reduce the net moment and thus the deflection on the sting while still retaining the aerodynamic moment. A new placement for specimen attachment however would mean finding a method to neglect the sting effects. The primary concern here was how an attachment could be made to a thin flexible specimen.

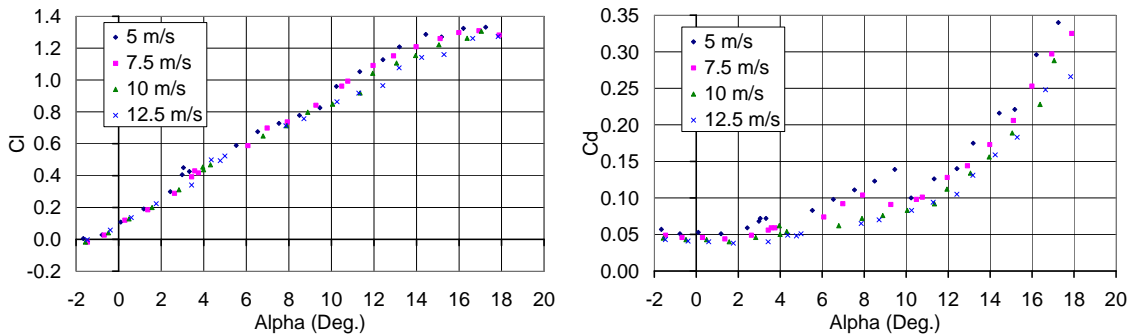
These changes would allow for automatic angle of attack changes, more reliable data, and a faster data collection process that will enhance the quality of the overall system and allow for new experiments of simulated, in flight, micro air vehicles.

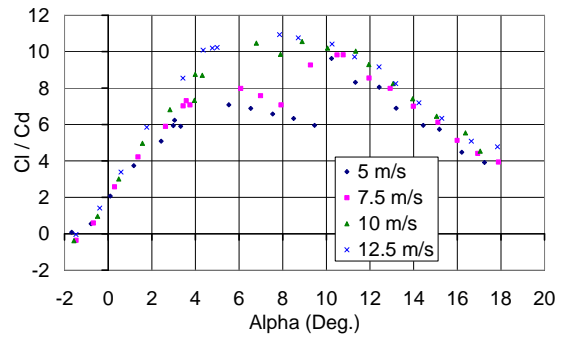
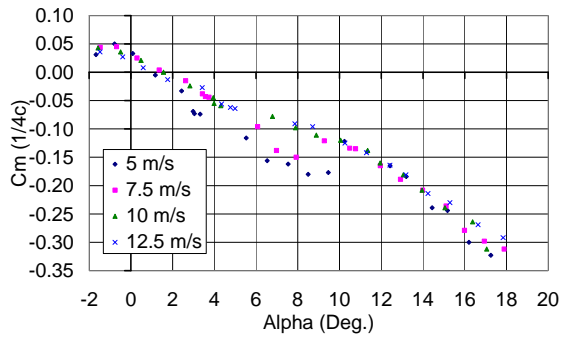
## APPENDIX A: Wing and Aircraft Data

### 1. 8300 Rectangular Flexible Wing (Wing 0)

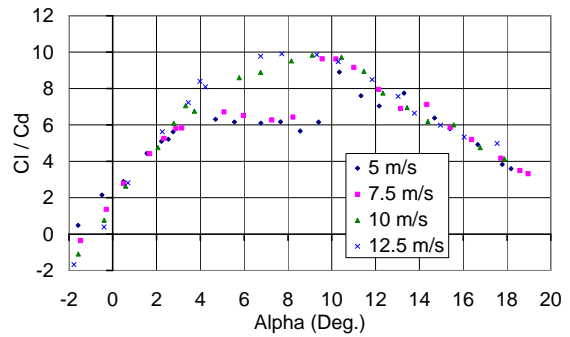
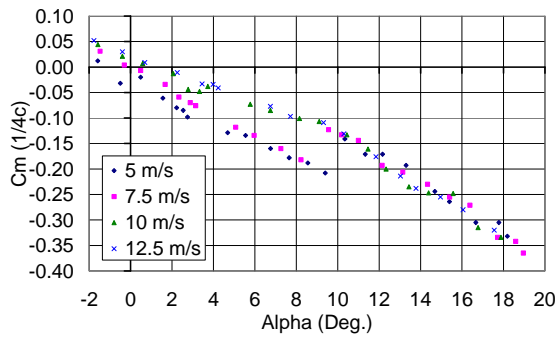
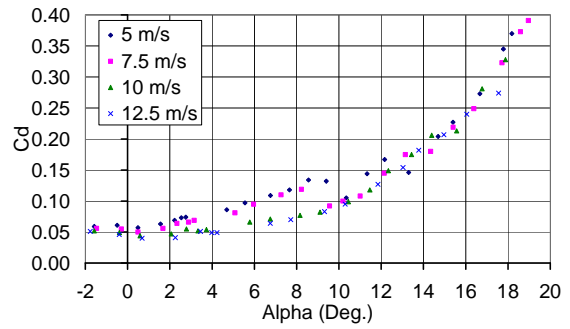
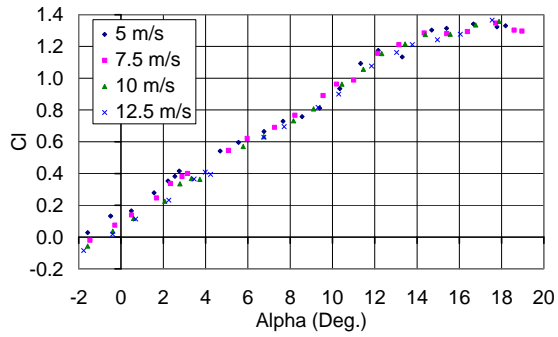


### 2. UF Rectangular Flexible Wing (Wing 1)

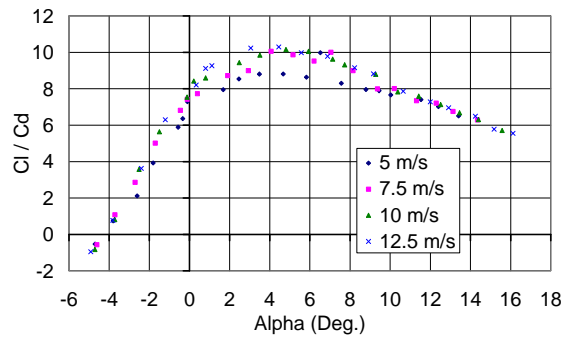
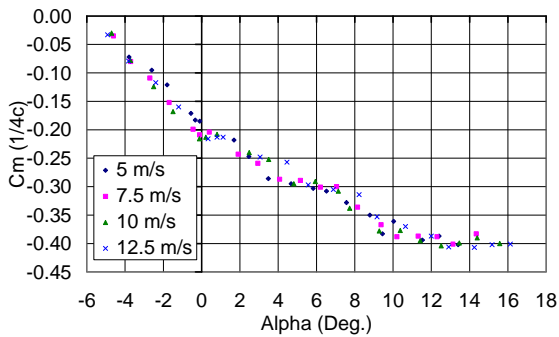
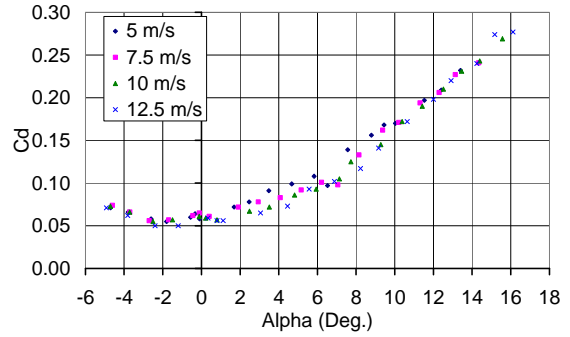
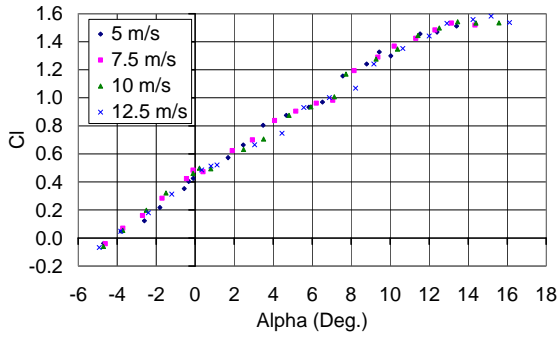




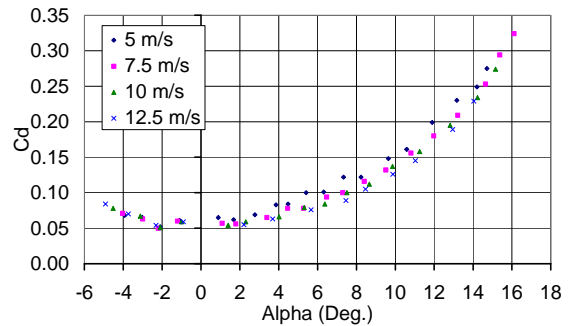
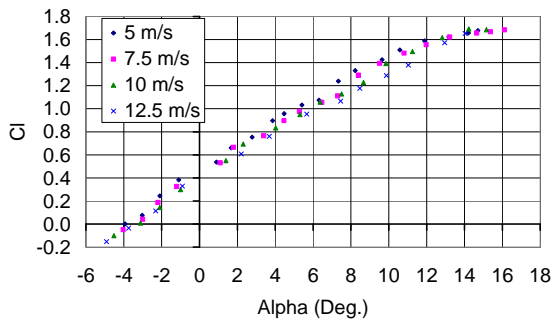
### 3. UF Rectangular Rigid Wing (Wing 2)

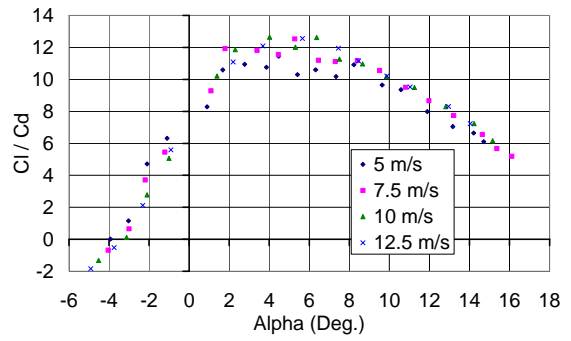
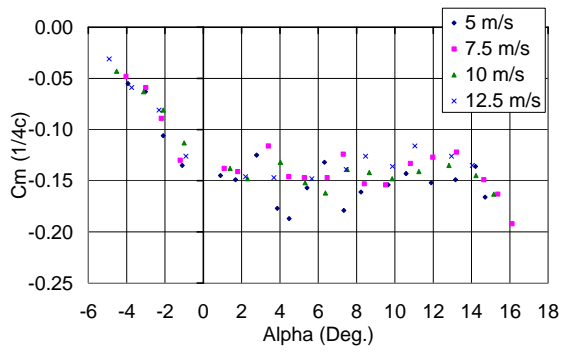


#### 4. 8300 Rectangular Rigid Wing (Wing 3)

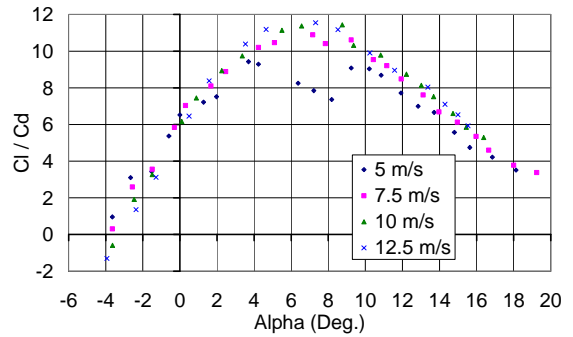
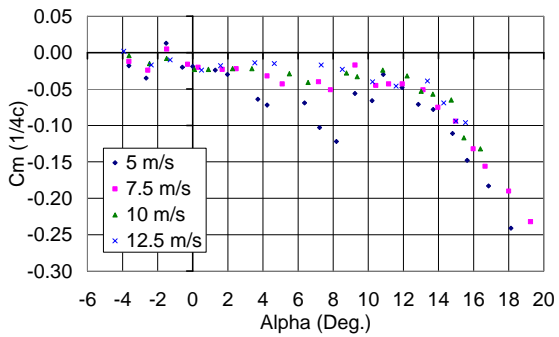
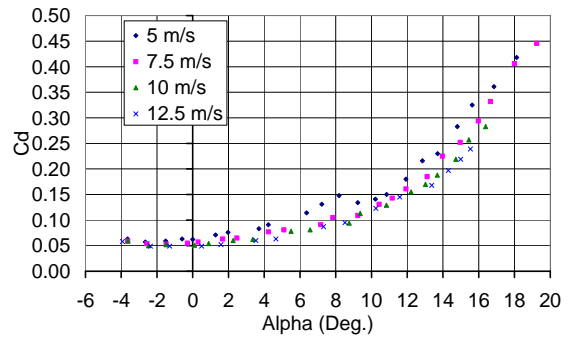
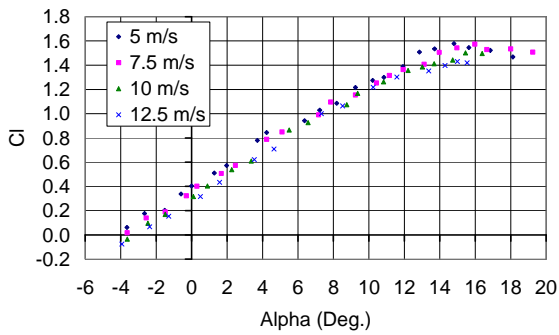


#### 5. 8300 Elliptical Flexible Wing with Winglets (Wing 4)

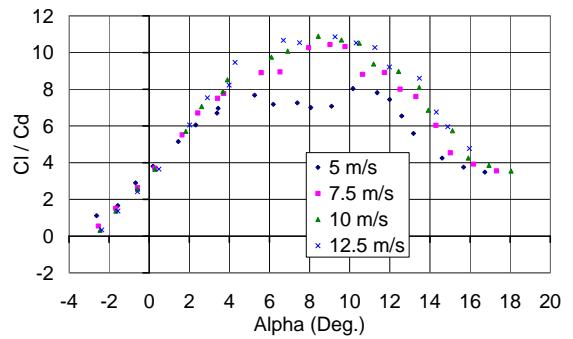
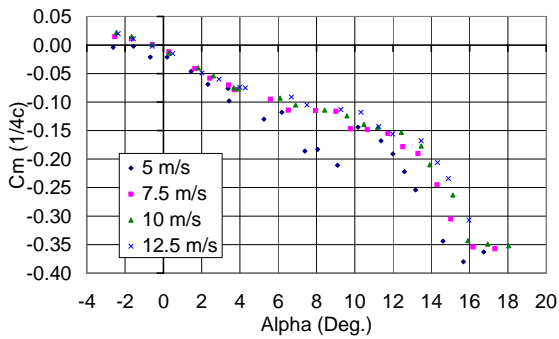
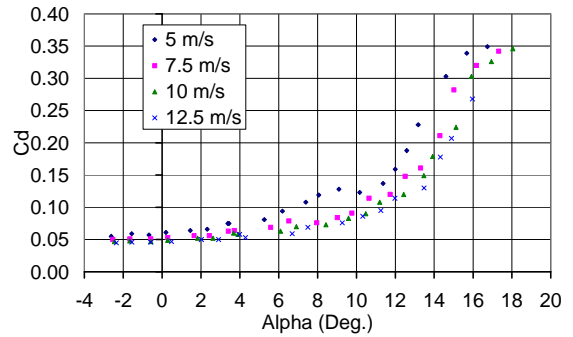
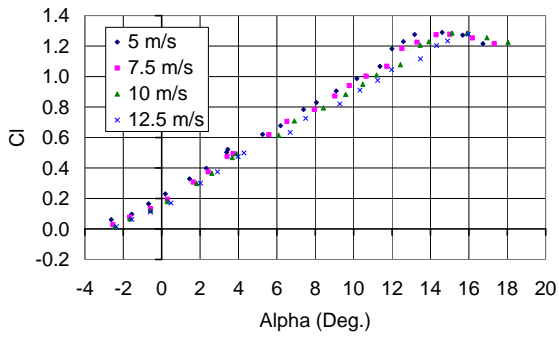




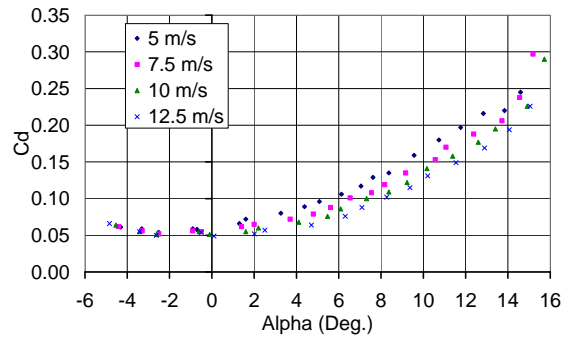
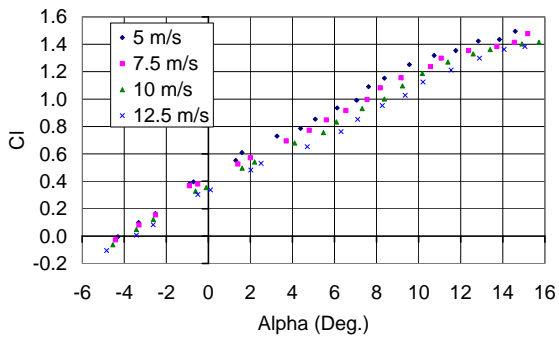
## 6. UF Elliptical Flexible Wing with Winglets (Wing 5)

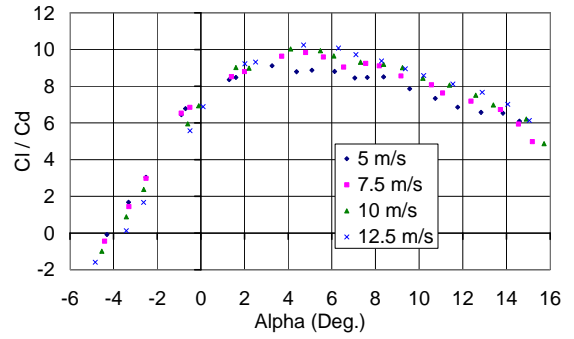
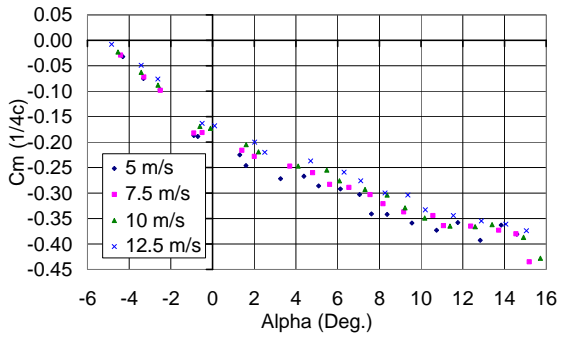


### 7. UF Tapered Flexible Wing with 1/8" LE Thickness (Wing 6)

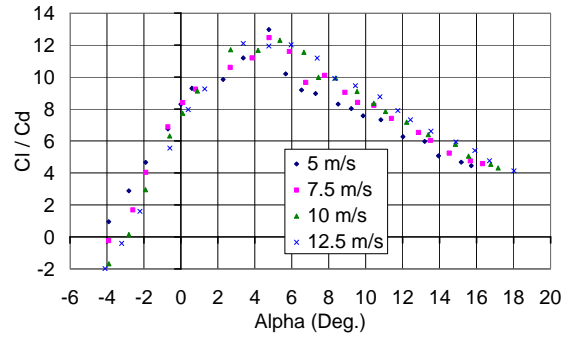
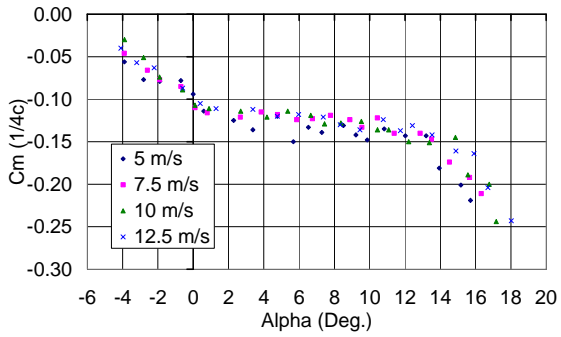
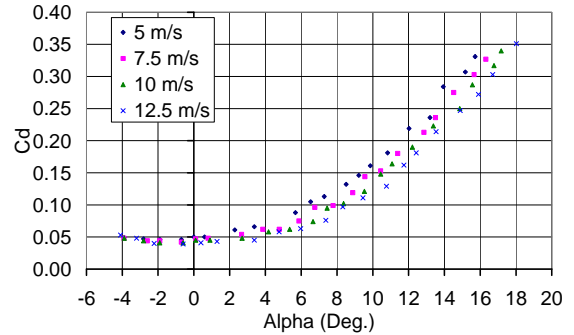
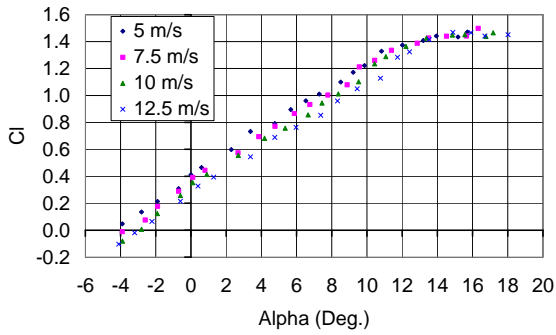


### 8. 8300 Rectangular Flexible Wing with 1/8" LE Thickness (Wing 7)

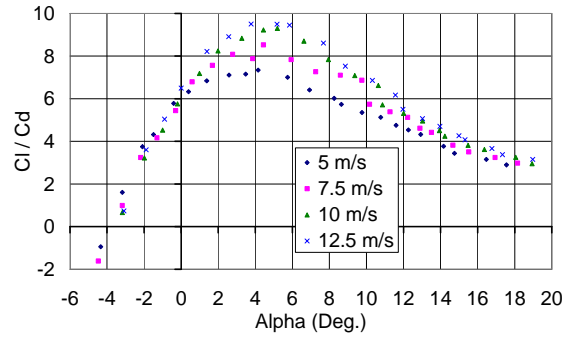
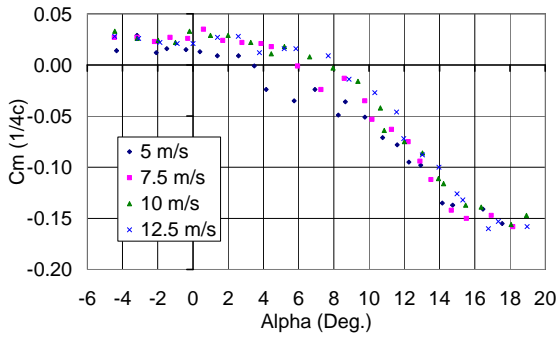
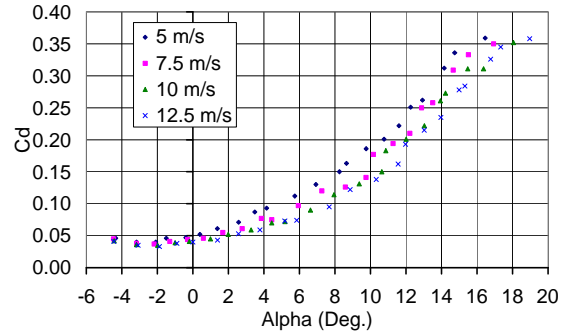
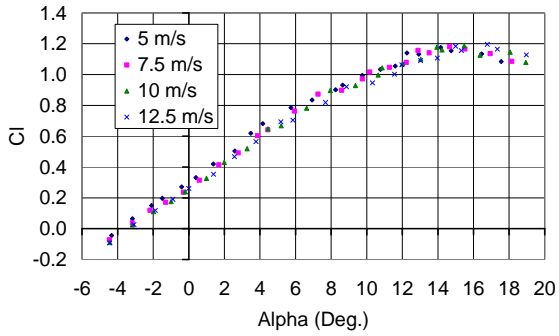




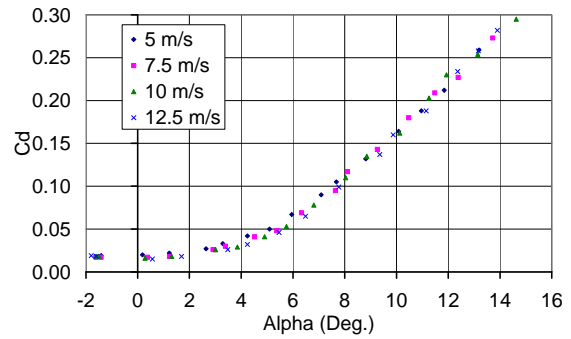
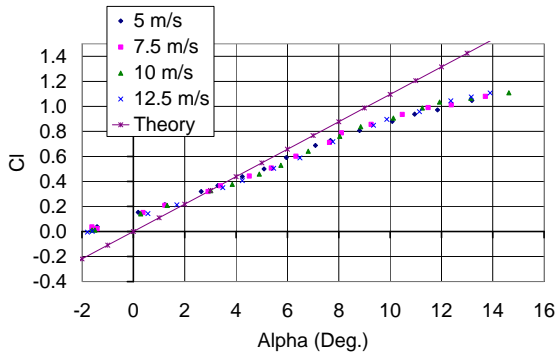
### 9. 8300 Elliptical Flexible Wing (Wing 8)

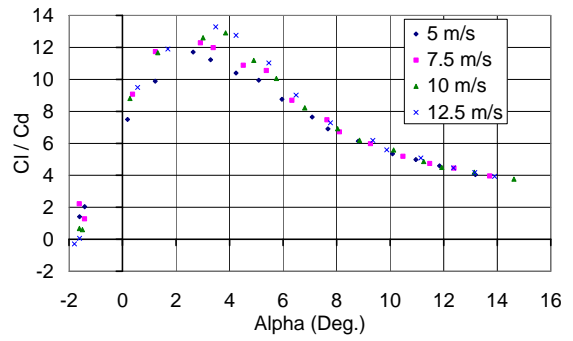
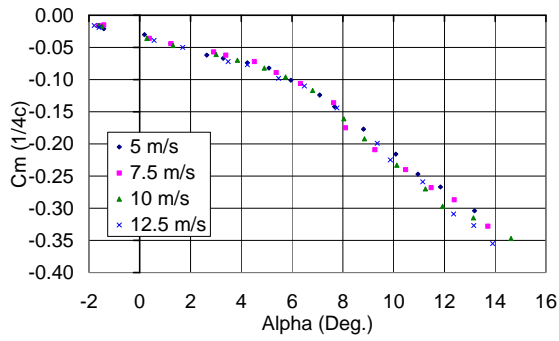


## 10. UF Elliptical Flexible Wing (Wing 9)

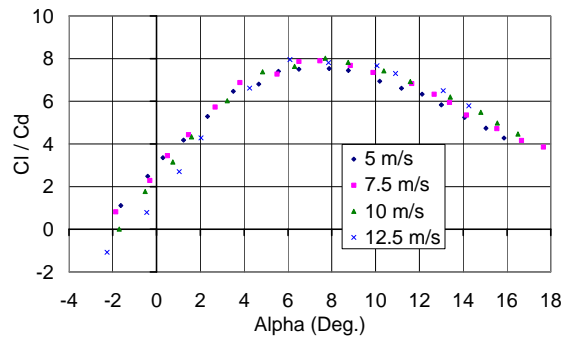
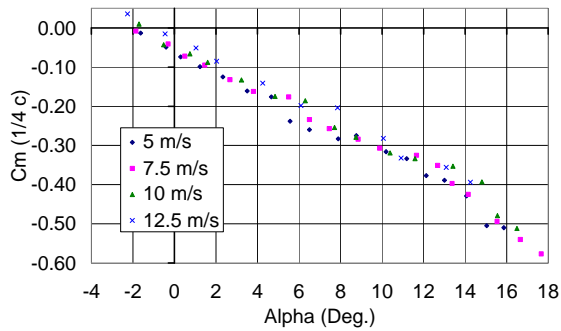
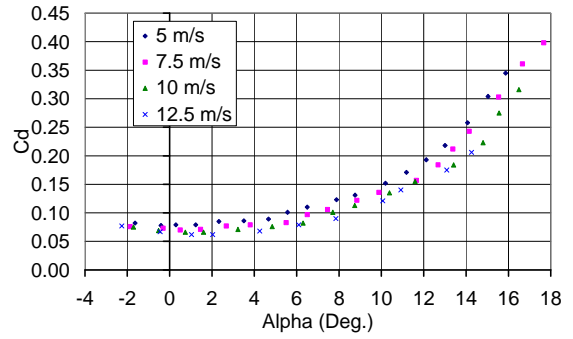
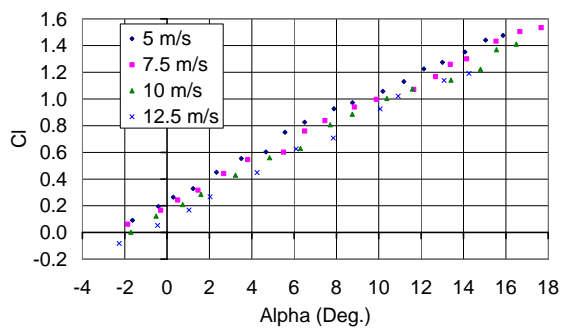


## 11. Flat Plate (FP)

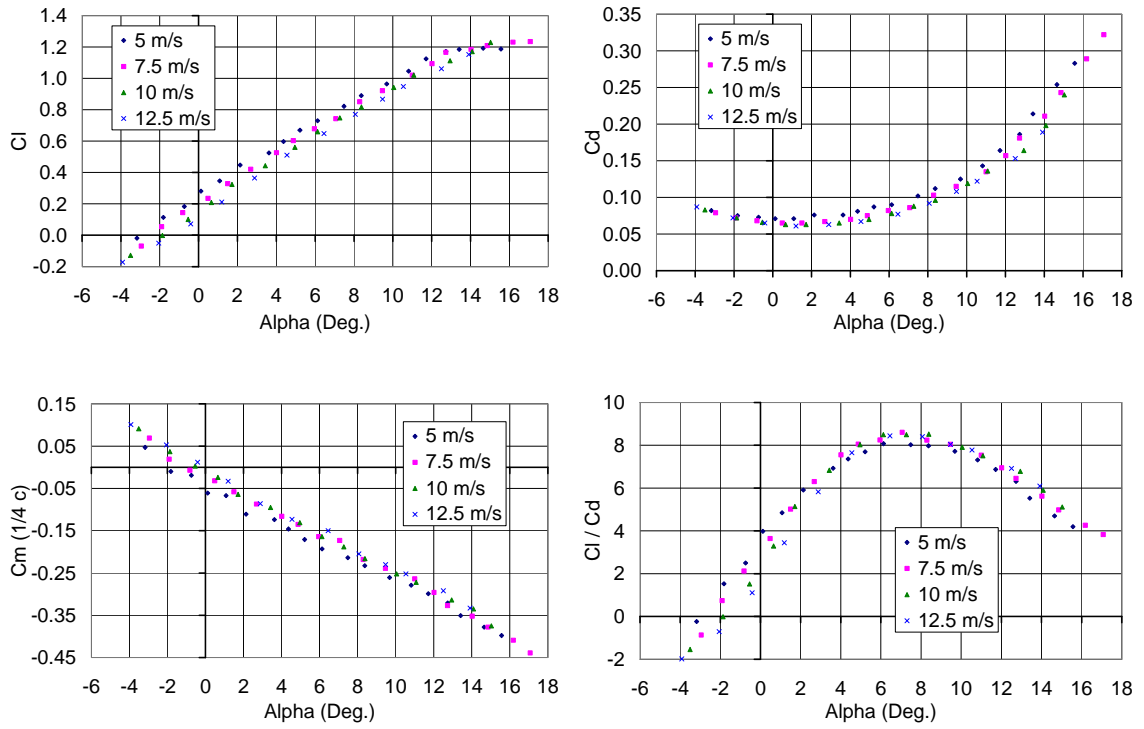




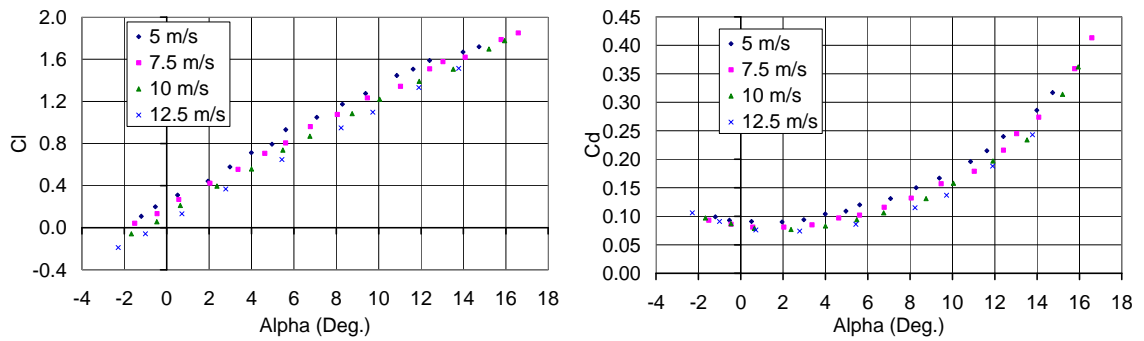
## 12. Fuselage B with 8300 Rectangular Flexible Wing (BW0)

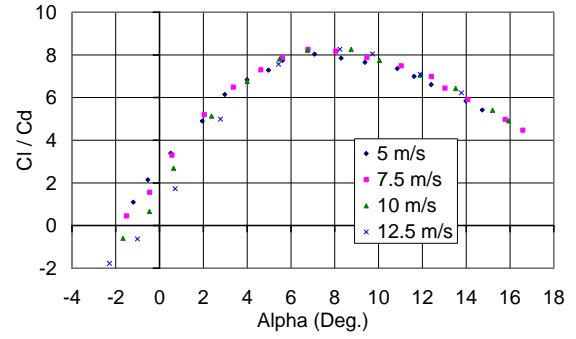
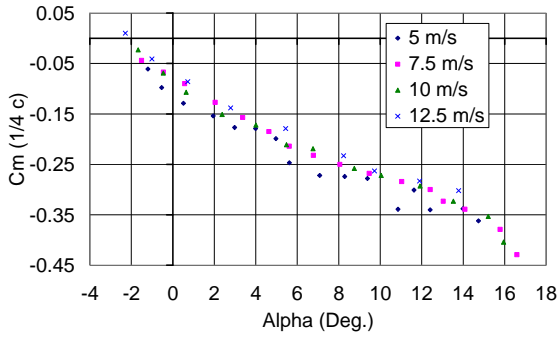


### 13. Fuselage B with 8300 Elliptical Flexible Wing with Winglets (BW4)

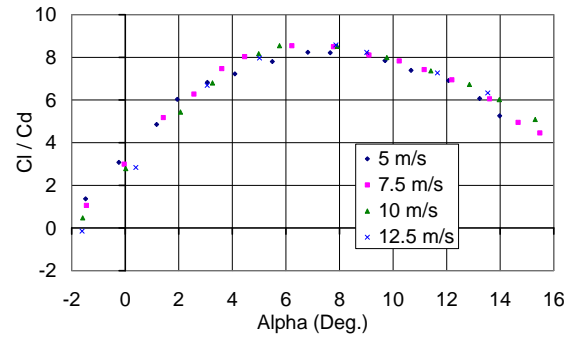
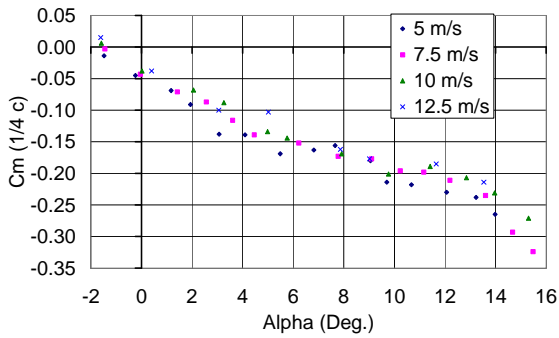
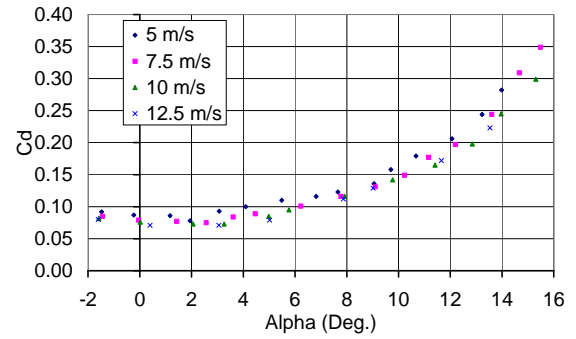
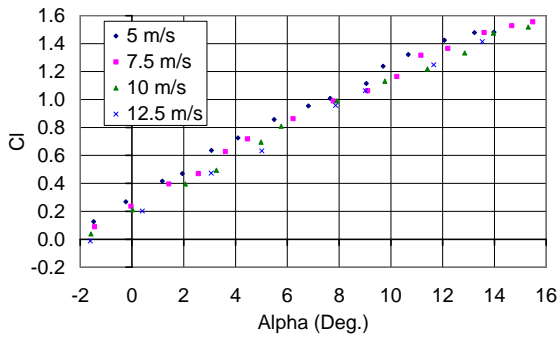


### 14. Fuselage C with 8300 Rectangular Flexible Wing (CW0)



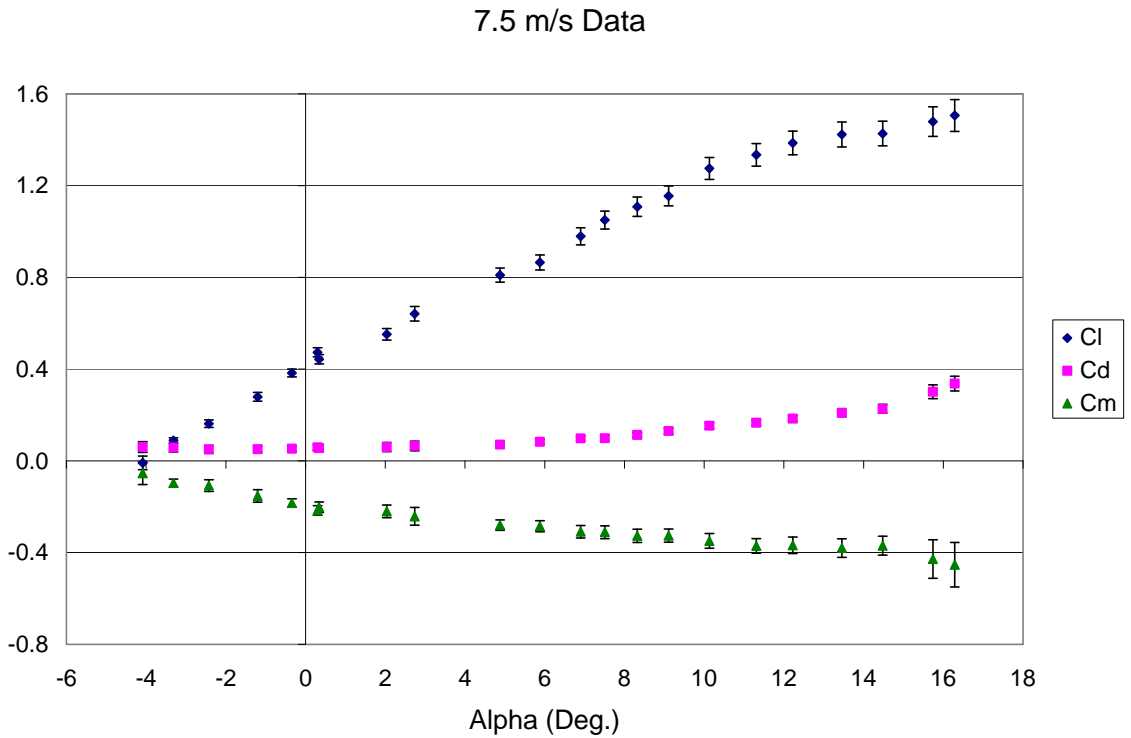
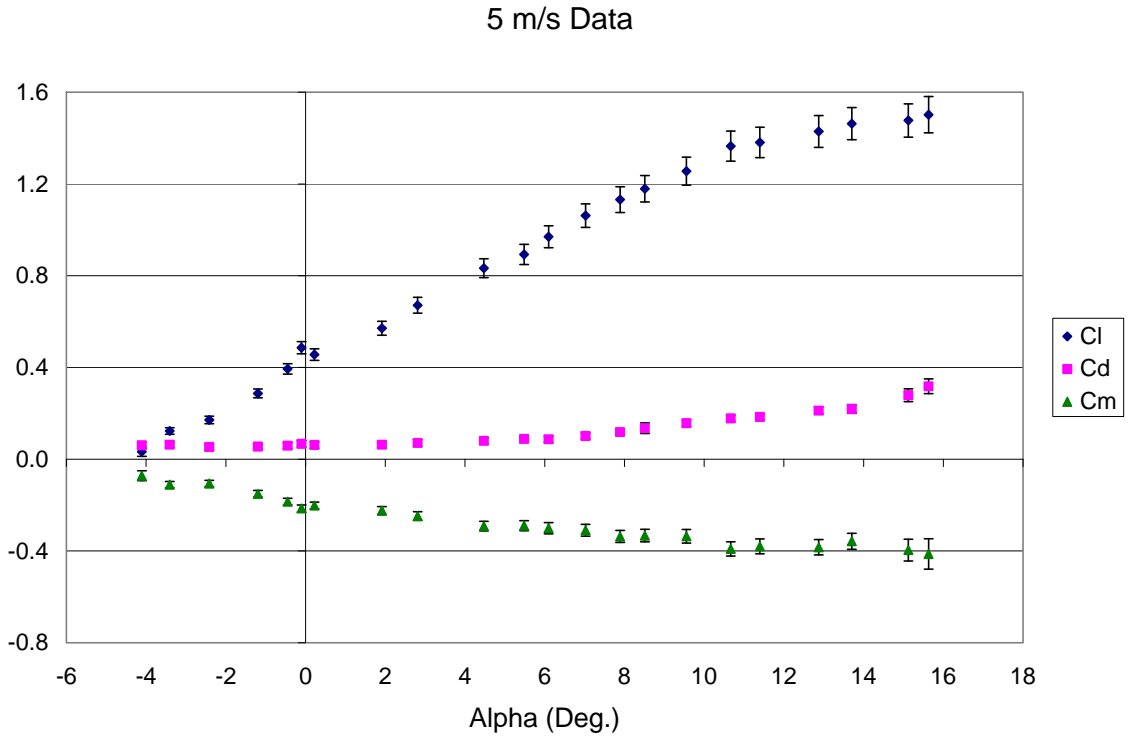


### 15. Fuselage C with 8300 Elliptical Flexible Wing with Winglets (CW4)

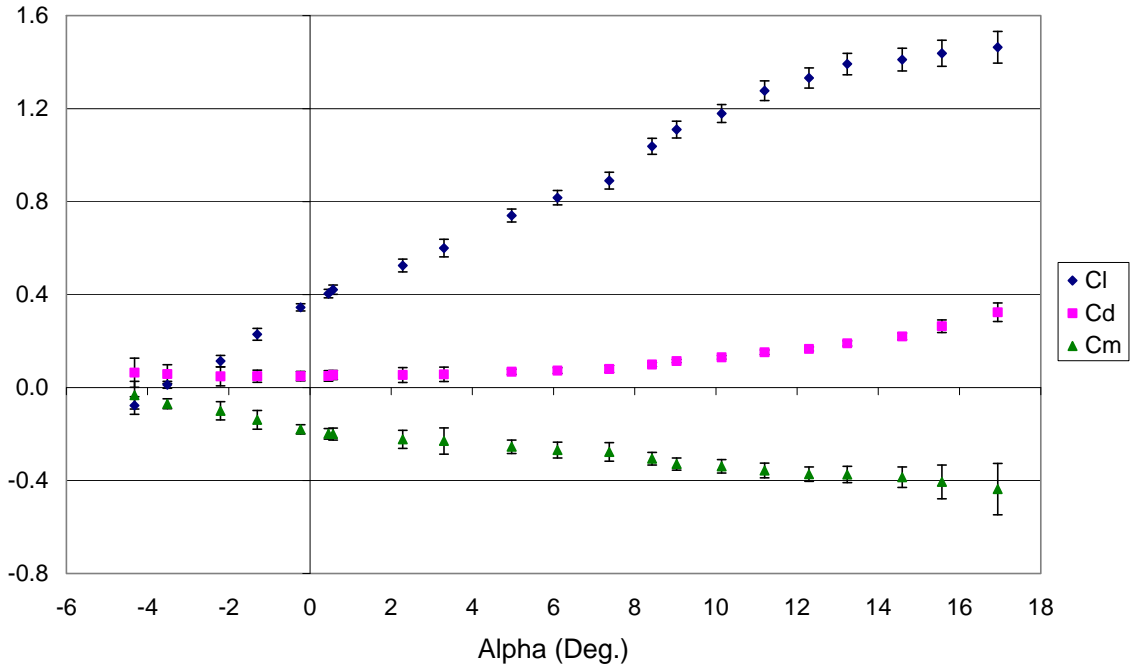


APPENDIX B: Error Analysis Data – WING 0 & BW0

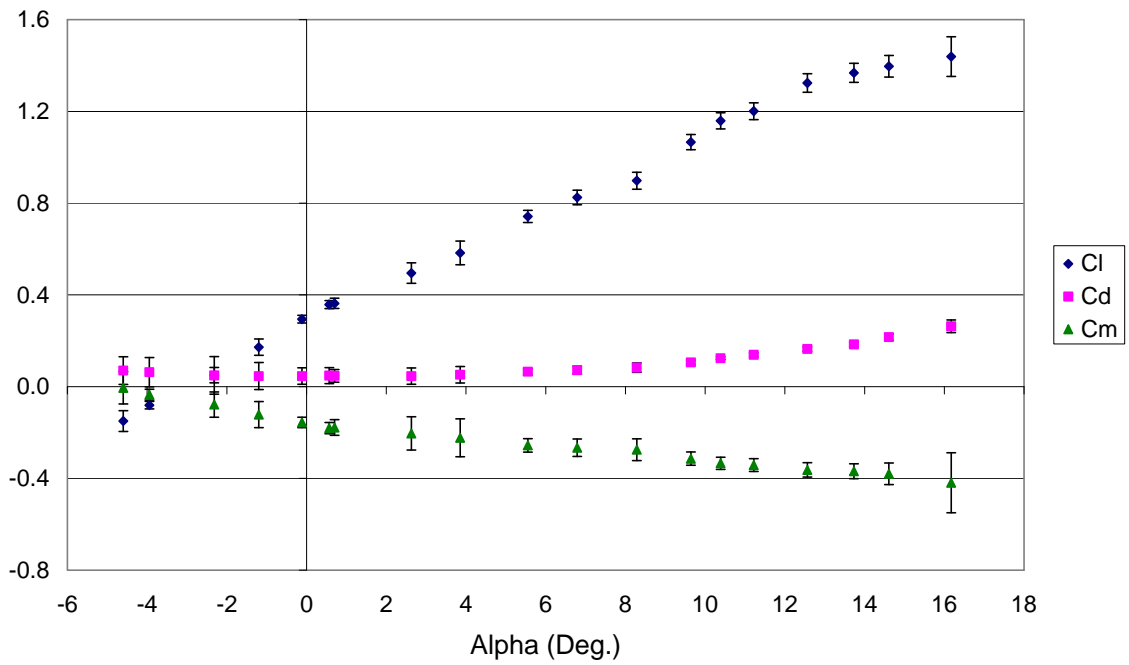
B.1: Wing 0



10 m/s Data

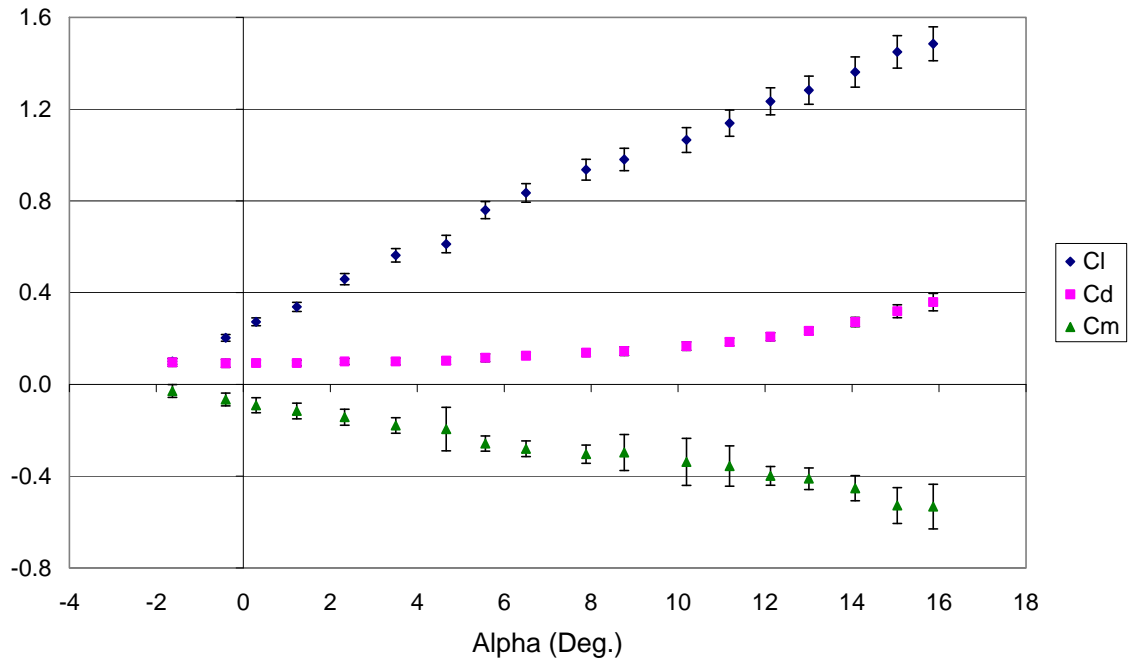


12.5 m/s Data

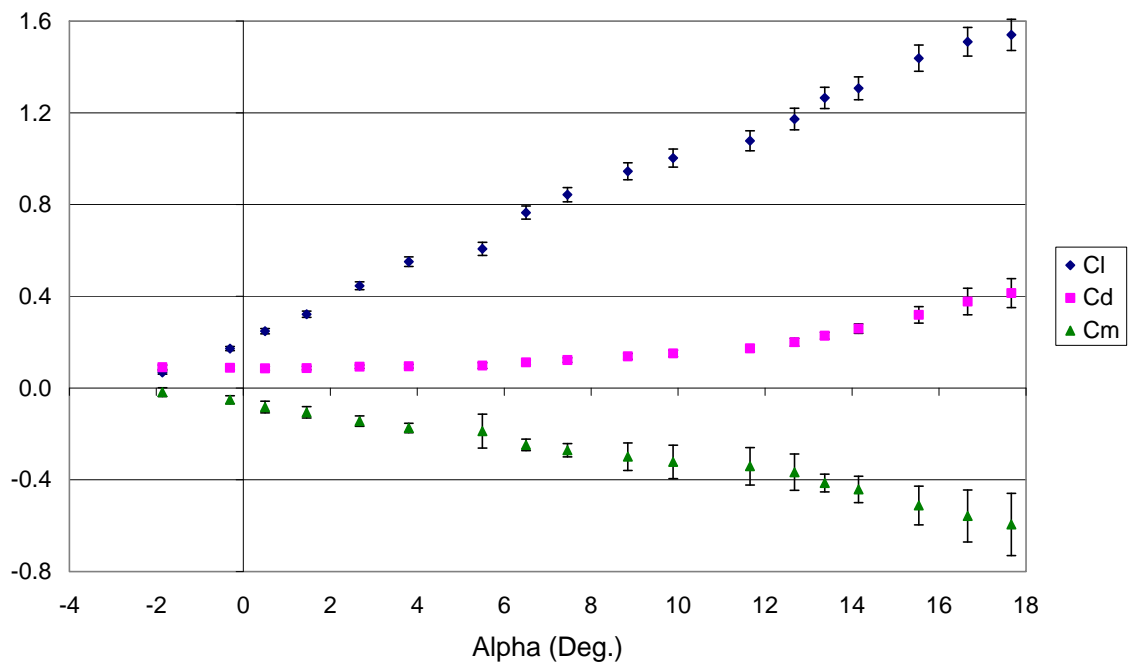


B.2: BW0

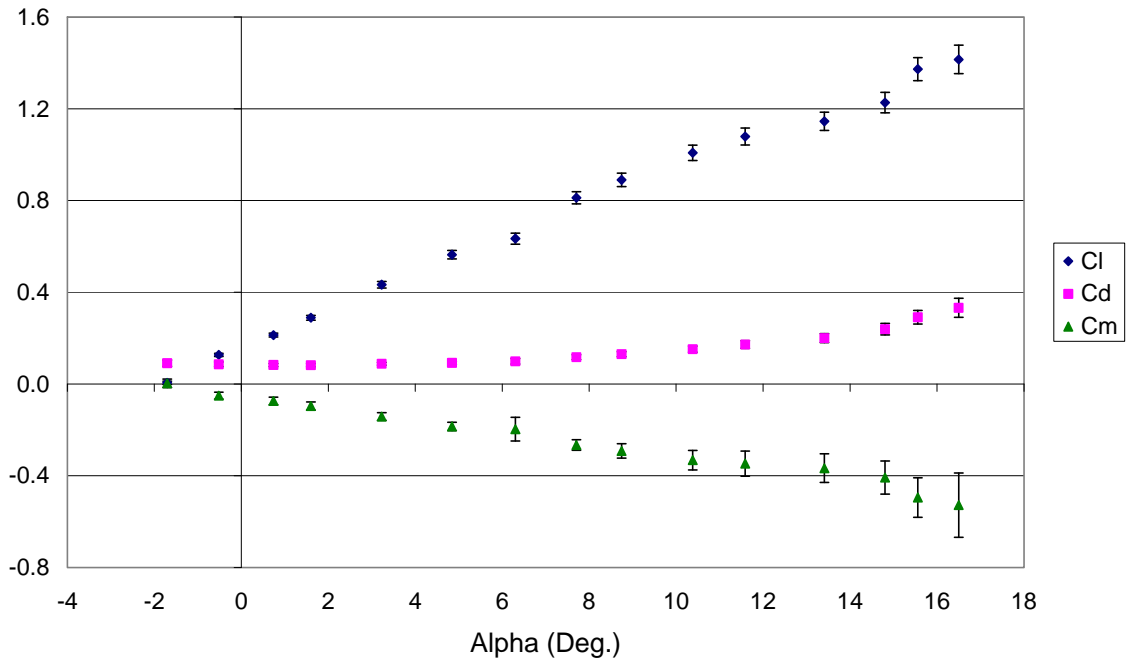
5 m/s Data



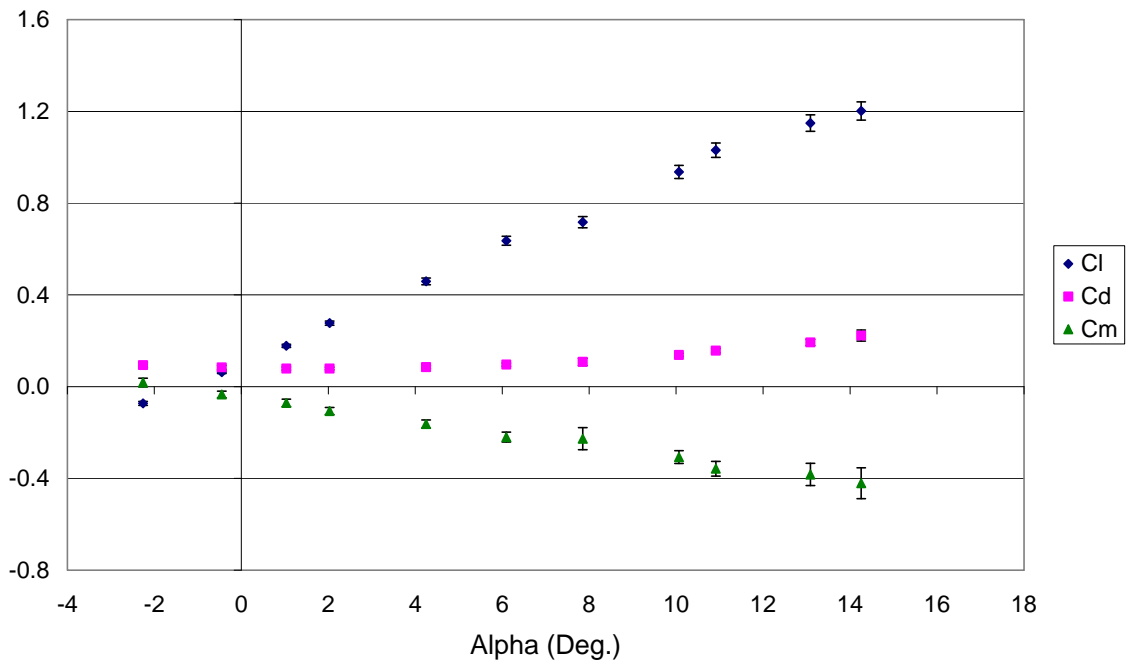
7.5 m/s Data



10 m/s Data



12.5 m/s Data



## APPENDIX C: Matlab Code

### B.1 – CALIBRATION CONVERSION CODE

#### **Part 1: Calibration Data**

```
% General x-axis numbers
a = [-.8 -50.2 -100.9 -200.9 -500.5];
% Lift:
L = [-.778 -.9827 -1.195 -1.612 -2.861];
% Drag:
D = [5.57 5.3614 5.1457 4.7198 3.4436];
% Moment:
M = [1.49 1.5651 1.6241 1.7585 2.1594];
Lift = polyfit(L,a,1);
Drag = polyfit(D,a,1);
Moment=polyfit(M,a,1);
```

#### **Part 2: Conversion to mass**

```
% Written by John Bear, Edited by Tim Witushynsky
% given raw wind tunnel and calibration data, this program outputs averaged
% and the standard deviation for the tunnel (voltage) data as well as
% converted (mass) data from the conversion provided in the calibration file
% into a text file ('stats.txt')
% 'names.txt' file with the file names in a column exists; the file names
% should be listed in drag, lift, moment order b/c the drag calibration data
% is applied to the first 1/3rd of the files, lift to the second 1/3rd, etc.
clear
Calibration_No_Plug; % allows access to variables from Calibration .m file
n=importdata('data.txt');
name=cellstr(n');
data=zeros(20000, length(name));
i=1;
while i <= length(name)
    data(1:20000, i)=load(name{i});
    % put the data from each file listed in the 'name' vector into a
    % column of the 'data' matrix
    i=i+1;
end
avg=mean(data);
stdev=std(data);
% get average and std dev for each column in the 'data' matrix
mass=zeros(1, length(avg));
m=1;
while m <= length(avg)
    if m <= length(avg)/3
        mass(m)=avg(m)*Drag(1)+Drag(2);
```

```

elseif m <= 2*length(avg)/3
    mass(m)=avg(m)*Lift(1)+Lift(2);
else
    mass(m)=avg(m)*Moment(1)+Moment(2);
end
m=m+1;
end
%convert the average voltage data into mass data based on the coefficients
%from the calibration file
answers{1, 1} = '';
answers{2, 1} = 'Average_V';
answers{3, 1} = 'Std_Dev';
answers{4, 1} = 'Mass_g';
%create 1st column labels for the final 'answers' array
k=1;
while k <= length(name)
    answers{1, k+1} = name{k};
    answers{2, k+1} = avg(k);
    answers{3, k+1} = stdev(k);
    answers{4, k+1} = mass(k);
    k=k+1;
end
%fill the other columns of the array with title, average, std dev, and mass
fid=fopen('stats.txt', 'wt');
fprintf(fid, '%c', ' ');
fclose(fid);
diary('stats.txt');
disp(answers);
diary off;
xlswrite('wing_data', answers)

```

## B.2 – WING CURVATURE ANALYSIS CODE

### Part 1: Image Analysis Static Loads Picture 1

```

% White Background Image Analysis, not full wing
K = input('Enter Picture 1 name, including extension: ','s');
I = imread(K);
figure(1)
imshow(I);
crop = input('Crop image? [y/n]: ','s');
if crop == 'y'
    [x,y,P] = impixel;
    %Select upper left and lower right side of pic
    x=x';
    y=y';
    x2=x(2)-x(1);

```

```

    y2=y(2)-y(1);
    rect = [x(1) y(1) x2 y2];
    C_Image = imcrop(I,rect);
end
%Filter Image by color:
xy = size(C_Image);
y1 = xy(1);
x1 = xy(2);
for i = 1:y1
    for j = 1:x1
        if C_Image(i,j,1) <= 100 %Red
            if C_Image(i,j,2) <= 100 %Green
                if C_Image(i,j,3) <= 80 %Blue
                    C_Image2(i,j) = 1;
                else C_Image2(i,j) = 0;
            end
        else C_Image2(i,j) = 0;
        end
    else C_Image2(i,j) = 0;
    end
end
end
end
%Filtered Image:
figure(1)
imshow(C_Image2)
%Delete Extraneous Regions:
i = 1;
while i == 1
    %Get two data points (for delete region box)
    [x,y,P] = impixel; %Upper Left to Lower Right
    x = x';
    y = y';
    for l = x(1):x(2)
        for m = y(1):y(2)
            C_Image2(m,l) = 0;
        end
    end
end
%Show Refined Image:
figure(2)
imshow(C_Image2);
Delete_Region = input('Delete another region? [n/y]: ','s');
if Delete_Region == 'y'
    i = 1;
else i = 0;
end
end
end

```

```

%Show Image (reference)
figure(3)
imshow(C_Image2)
%Average the airfoil line now:
%Find average y value of white pixels on C_Image2 for each column
for j = 1:x1
    h = 0;
    h_avg = 0;
    for i = 1:y1
        if C_Image2(i,j) == 1;
            h_avg = h_avg + i;
            h = h+1;
        end
    end
    if h == 0
        pixel_h = 0;
    else
        pixel_h = h_avg/h;
    end
    pixel_height(j) = round(pixel_h);
end
%Recompile picture with avg pixel line of wing:
for j = 1:x1
    for i = 1:y1
        for k = 1:3
            C_Image2_Overlay(i,j,k) = C_Image(i,j,k);
        end
    end
end
for j = 1:x1
    if pixel_height(j) ~= 0
        for k = 1:3
            C_Image2_Overlay(pixel_height(j),j,k) = 255;
        end
    end
end
%Show recompiled image:
figure(4)
imshow(C_Image2_Overlay);
%Make this image black and white:
I2 = rgb2gray(C_Image2_Overlay);
for j = 1:x1
    for i = 1:y1
        if I2(i,j) < 255
            I2(i,j) = 0;
        end
    end
end

```

```

    end
end
%Show edited picture:
figure(5)
imshow(I2);

```

## Part 2: Image Analysis Static Loads Picture 2

See Part 1: Image Analysis Static Loads Picture 1

Part 2 is the same code as Part 1; analysis is completed for a second picture and labeled differently (I3, shown below in Part 3).

## Part 3: Image Curvature Change

```

%Image compilation
%Rotate image 1 onto image 2
%Make a curvature comparison
%Crop image if necessary:
figure(1);
imshow(I2);
crop = input('Crop image? [y/n]: ','s');
if crop == 'y'
    [x,y,P] = impixel;
    %Select upper left and lower right side of pic
    x=x';
    y=y';
    x2=x(2)-x(1);
    y2=y(2)-y(1);
    rect = [x(1) y(1) x2 y2];
    I2 = imcrop(I2,rect);
    I3 = imcrop(I3,rect);
end
xy = size(I2);
x1 = xy(2);
y1 = xy(1);
%Combine I2 and I3 into IC
for i = 1:x1
    for j = 1:y1
        if I2(j,i) == 255 || I3(j,i) == 255
            IC(j,i) = 255;
        else
            IC(j,i) = 0;
        end
    end
end
end
%Show combined image:

```

```

figure(1)
imshow(IC);
k = 1;
while k == 1
    %User input to rotate image 1:
    rotate = input('Angle to rotate: ','s');
    rotate = str2num(rotate);
    I2 = imrotate(I2,rotate,'crop');
    %User input to translate image 1:
    LR = input('Move left (neg) or right (pos), image 1: ','s');
    LR = str2num(LR);
    UD = input('Move up (neg) or down (pos), image 1: ','s');
    UD = str2num(UD);
    %Create a blank picture
    for i = 1:x1
        for j = 1:y1
            I2_copy(j,i) = 0;
        end
    end
    %Add and move all white pixels
    for i = 1:x1
        for j = 1:y1
            if I2(j,i) == 255
                I2_copy(j+UD,i+LR) = 255;
            end
        end
    end
    %Sub back to original:
    I2 = I2_copy;

    %Combine I2 and I3 into IC
    for i = 1:x1
        for j = 1:y1
            if I2(j,i) == 255 || I3(j,i) == 255
                IC(j,i) = 255;
            else
                IC(j,i) = 0;
            end
        end
    end
    %Show combined image:
    figure(1)
    imshow(IC);
    %Continue to adjust combined image:
    adjust = input('Continue adjustment? [y/n]: ','s');

```

```

    if adjust ~= 'y'
        k = 0;
        break;
    end
end
%Take adjusted image 1 and 2 and compare pixel deviations
figure(1)
imshow(IC);
diff = []; %Concatination for difference in pixels
N = 0;
for i = 1:x1 %Each column
    %Reset j_I2 and j_I3
    j_I2 = -1;
    j_I3 = -1;
    for j = 1:y1 %going through each row of column i
        if I2(j,i) == 255
            j_I2 = j;
        end
        if I3(j,i) == 255
            j_I3 = j;
        end
    end
    %If both j_I2 and j_I3 are positive, find the difference and abs
    %value of them
    if j_I2 > 0 && j_I3 > 0
        diff = [diff abs(j_I2 - j_I3)];
        N = N+1;
    end
end
end

% Using diff and N, calculate the image standard deviation
for i = 1:length(diff)
    diff_squared(i) = diff(i)*diff(i);
end
sum_diff_sq = sum(diff_squared);
std_dev = sqrt(sum_diff_sq/N);
disp('Standard Deviation in Pixels: ')
disp(std_dev)

Part 4: Conversion to inches
%Conversion from pixels to inches for std_dev
%Call up IC, find TE and LE
figure(6)
imshow(IC)
%First select region for TE, then LE and find pixel for exact placement.
%TE:

```

```

[x,y,P] = impixel; %Upper left to lower right
x=x';
y=y';
k = 0;
for i = x(1):x(2)
    for j = y(1):y(2)
        if IC(j,i) == 1
            k = 1;
            break;
        end
    end
    if k == 1
        break;
    end
end
TE = [j i];
%LE:
[x,y,P] = impixel; %Upper left to lower right
x=x';
y=y';
k = 0;
l = x(2)-x(1);
m = y(2)-y(1);
for i = 1:l
    for j = 1:m
        if IC(y(2)-j+1,x(2)-i+1) == 1
            k = 1;
            break;
        end
    end
    if k == 1
        break;
    end
end
LE = [y(2)-j+1 x(2)-i+1];
%Calculate the pixel distance from the TE to LE:
a = abs(LE(2)-TE(2));
b = abs(LE(1)-TE(1));
c = sqrt(a*a+b*b);
pixel_length = round(c);
std_dev_in = std_dev*6/pixel_length;
disp('Standard Deviation in inches: ')
disp(std_dev_in)

```

### **Part 5: Compilation**

%Combine and use all three m-files for image analysis:

%Image analysis, picture 1:

Image\_Analysis\_Static\_Loads\_pic1 %I2

disp('pause')

pause

%Image analysis, picture 2:

Image\_Analysis\_Static\_Loads\_pic2 % I3

disp('pause')

pause

%Cuvature change:

Image\_Curvature\_Change %Gives std\_dev in #pixels

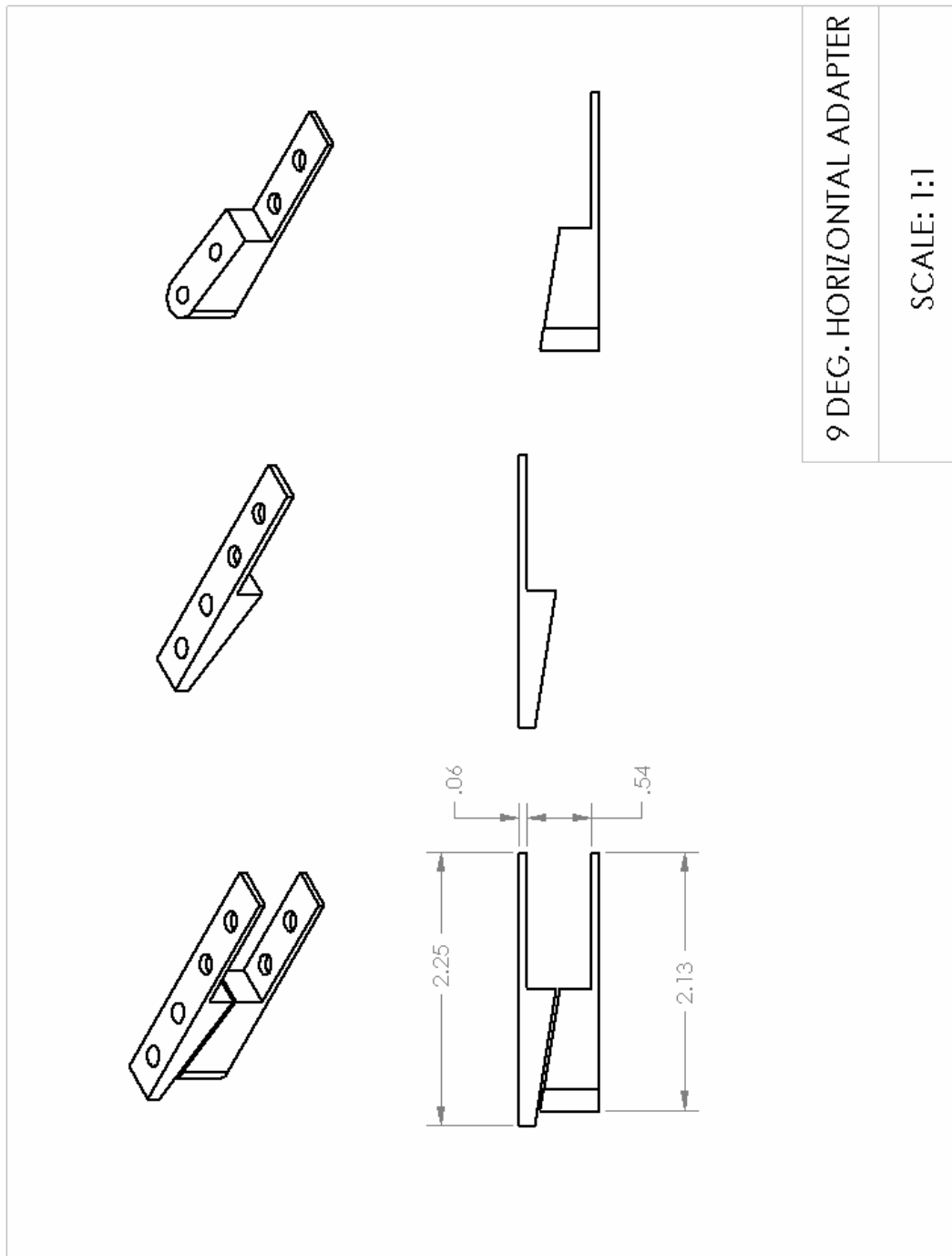
disp('pause')

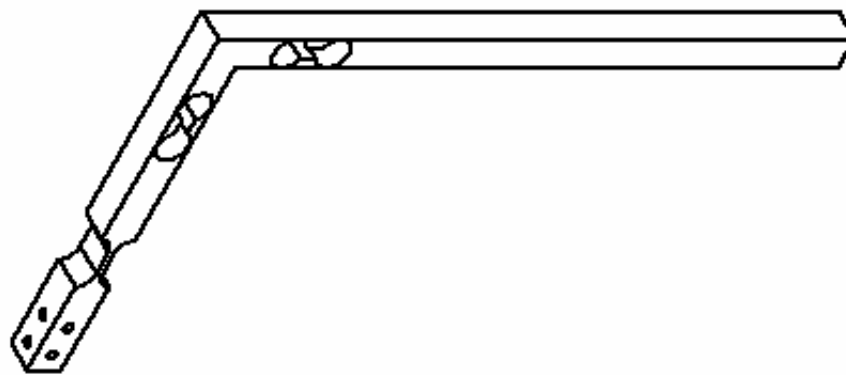
pause

%Conversion to std\_dev in inches:

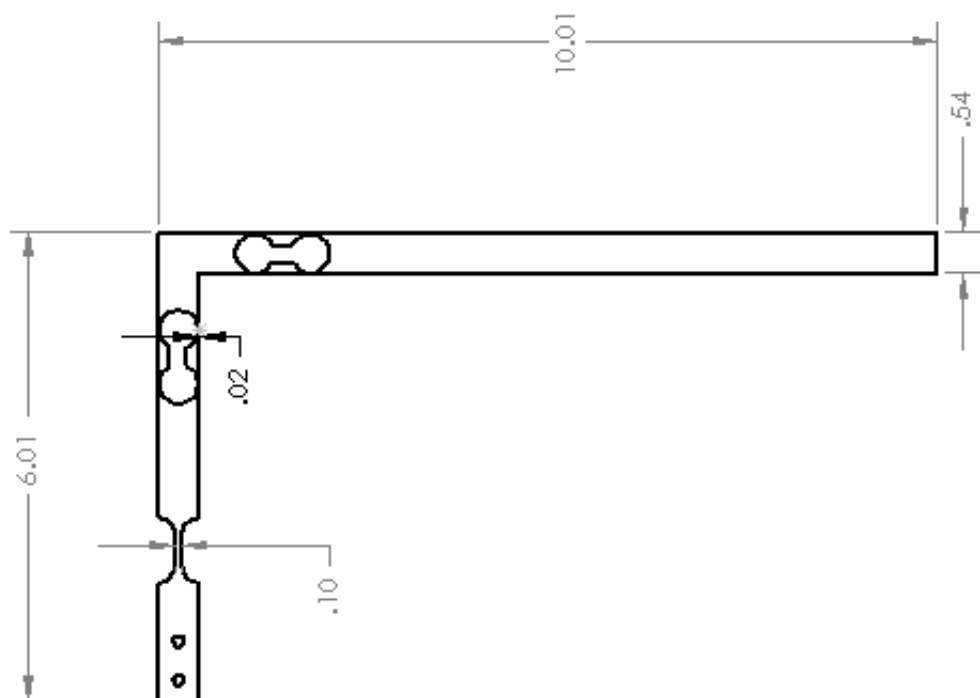
Conversion

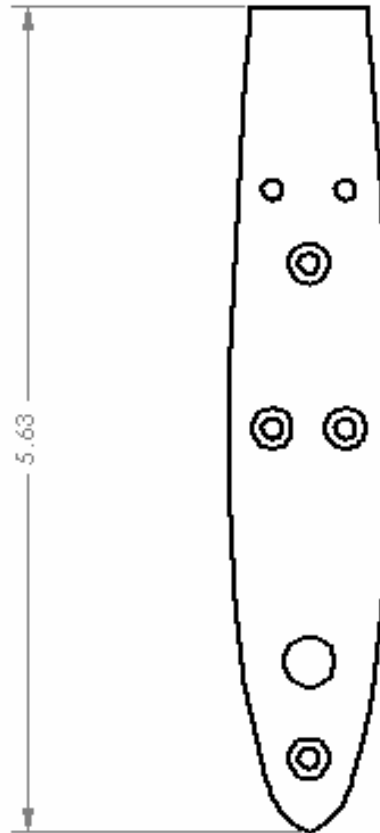
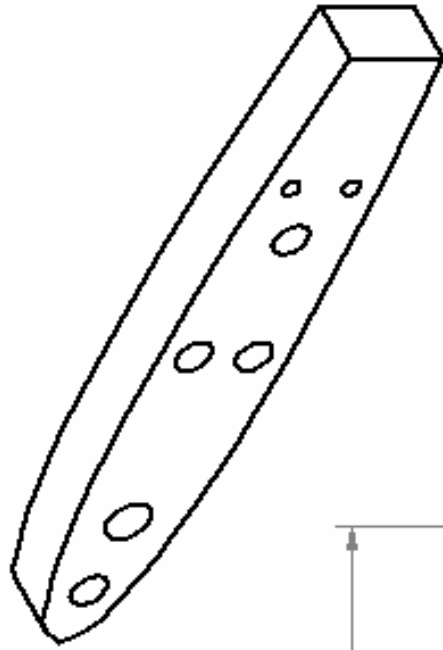
APPENDIX D: Technical Drawings





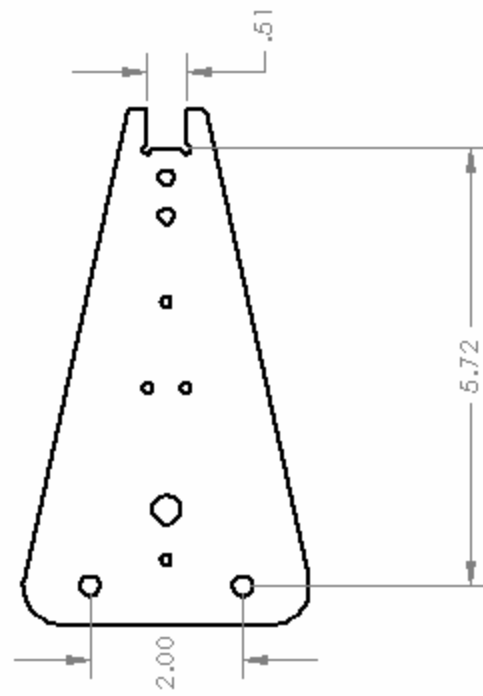
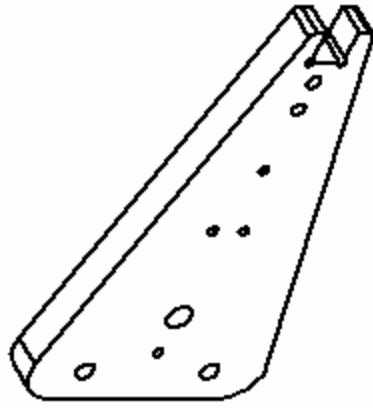
|            |
|------------|
| STING      |
| SCALE: 1:2 |





NACA 0012 AIRFOIL MOUNT

SCALE: 1:1



MOUNTING PLATE

SCALE: 1:2

## APPENDIX E: Equations

$$1. V_L = X_L * .0042 - .7771$$

$$2. V_M = X_M * (-.0013) + 1.4929$$

$$3. V_D = (X_D * .0043) + 5.8424 - \left( .0001 * \frac{L_{Tot}}{g} \right)$$

$$4. L_{Tot} = (X_L - X_{L_{V=0}}) * g$$

$$5. X_L = \left( \frac{V_L + .7771}{.0042} \right)$$

$$6. X_M = - \left( \frac{V_M - 1.4929}{.0013} \right)$$

$$7. X_D = \left( \frac{V_D - 5.8424 + .0001 * \frac{L_{Tot}}{g}}{.0043} \right)$$

$$8. M_R = X_M * a * g \text{ (Also Equation 27)}$$

$$9. \sum M_R = 0 = M_R - D_{net} * c - L_{Tot} * b - M_{1/4c} + Wa$$

$$10. D_{net} = (X_D - X_{D_{V=0}}) * g$$

$$11. C_L = \frac{2L_{Tot}}{\rho V^2 S}$$

$$12. C_D = \frac{2D_{net}}{\rho V^2 S}$$

$$13. C_{M_{1/4c}} = \frac{2M_{1/4c}}{\rho V^2 S c}$$

$$14. C_L = 2\pi\alpha$$

$$15. \rho = \frac{P}{RT}$$

$$16. \delta\rho^2 = \left(\frac{\partial\rho}{\partial T}\right)^2 * (\delta T)^2 + \left(\frac{\partial\rho}{\partial P}\right)^2 * (\delta P)^2 + (\delta\rho_{tol})^2$$

$$17. V = \sqrt{\frac{2\Delta P}{\rho}}$$

$$18. \delta V^2 = \left(\frac{\partial V}{\partial(\Delta P)}\right)^2 * (\delta\Delta P)^2 + \left(\frac{\partial V}{\partial\rho}\right)^2 * (\delta\rho)^2 + (\delta V_{tol})^2$$

$$19. \frac{\partial C_L}{\partial L_{Tot}} = \frac{2}{\rho V^2 S}$$

$$20. \frac{\partial C_L}{\partial\rho} = -\frac{2L_{Tot}}{\rho^2 V^2 S}$$

$$21. \frac{\partial C_L}{\partial V} = -\frac{4L_{Tot}}{\rho^2 V^3 S}$$

$$22. \frac{\partial C_L}{\partial S} = -\frac{2L_{Tot}}{\rho V^2 S^2}$$

$$23. \frac{\partial L_{Tot}}{\partial X_L} = g$$

$$24. \frac{\partial L_{Tot}}{\partial X_{L_{V=0}}} = -g$$

$$25. \delta L_{Tot}^2 = \left(\frac{\partial L_{Tot}}{\partial X_L}\right)^2 * (\delta X_L)^2 + \left(\frac{\partial L_{Tot}}{\partial X_{L_{V=0}}}\right)^2 * (\delta X_{L_{V=0}})^2$$

$$26. \delta C_L^2 = \left(\frac{\partial C_L}{\partial L_{Tot}}\right)^2 * (\delta L_{Tot})^2 + \left(\frac{\partial C_L}{\partial\rho}\right)^2 * (\delta\rho)^2 + \left(\frac{\partial C_L}{\partial V}\right)^2 * (\delta V)^2 + \left(\frac{\partial C_L}{\partial S}\right)^2 * (\delta S)^2$$

27.  $\delta D_{\text{net}}^2 = \left( \frac{\partial D_{\text{net}}}{\partial V_D} \right)^2 * (\delta V_D)^2 + \left( \frac{\partial D_{\text{net}}}{\partial V_{D_{v=0}}} \right)^2 * (\delta V_{D_{v=0}})^2 + \left( \frac{\partial D_{\text{net}}}{\partial L_{\text{Tot}}} \right)^2 * (\delta L_{\text{Tot}})^2$
28.  $\delta C_D^2 = \left( \frac{\partial C_D}{\partial D_{\text{net}}} \right)^2 * (\delta D_{\text{net}})^2 + \left( \frac{\partial C_D}{\partial \rho} \right)^2 * (\delta \rho)^2 + \left( \frac{\partial C_D}{\partial V} \right)^2 * (\delta V)^2 + \left( \frac{\partial C_D}{\partial S} \right)^2 * (\delta S)^2$
29.  $M_{1/4c} = M_{\text{sg}} - M_L - M_D - M_W$
30.  $\delta M_{\text{sg}}^2 = \left( \frac{\partial M_{\text{sg}}}{\partial \varphi_{\text{sg}}} \right)^2 * (\delta \varphi_{\text{sg}})^2$
31.  $Wa = x_w * W_{\text{eff}}$
32.  $\delta M_W^2 = \left( \frac{\partial M_W}{\partial W} \right)^2 * (\delta W)^2$
33.  $\delta M_L^2 = \left( \frac{\partial M_L}{\partial X_L} \right)^2 * (\delta X_L)^2 + \left( \frac{\partial M_L}{\partial L_{\text{Tot}}} \right)^2 * (\delta L_{\text{Tot}})^2$
34.  $\delta M_D^2 = \left( \frac{\partial M_D}{\partial X_D} \right)^2 * (\delta X_D)^2 + \left( \frac{\partial M_D}{\partial D_{\text{net}}} \right)^2 * (\delta D_{\text{net}})^2$
35.  $\frac{\partial M}{\partial M_{\text{sg}}} = \frac{\partial M}{\partial M_W} = \frac{\partial M}{\partial M_L} = \frac{\partial M}{\partial M_D} = \pm 1$
36.  $\delta M_{1/4c}^2 = \delta M_{\text{sg}}^2 + \delta M_W^2 + \delta M_L^2 + \delta M_D^2$
37.  $C_d = C_{d_0} + K * C_L^2$
38.  $C_l = b_0 + b_1 * \alpha + b_2 * \alpha^2$

Other Equations used but not included in the body of the thesis:

39.  $M_{1/4c} = M_R - D_{\text{net}} * c - L_{\text{Tot}} * b + Wa$
40.  $L_{\text{Tot}} = L - W$

$$41. D_{\text{net}} = D - D_{V=0}$$

$$42. M_{\text{sg}} = x_{\text{sg}} * \varphi_{\text{sg}}$$

$$43. M_L = x_L * L_{\text{Tot}}$$

$$44. M_D = x_D * D_{\text{net}}$$

$$45. M_W = x_W * W$$

46.

$$\delta C_{M_{1/4c}}^2 = \left( \frac{\partial C_{M_{1/4c}}}{\partial M_{1/4c}} \right)^2 * (\delta M_{1/4c})^2 + \left( \frac{\partial C_{M_{1/4c}}}{\partial \rho} \right)^2 * (\delta \rho)^2 + \left( \frac{\partial C_{M_{1/4c}}}{\partial V} \right)^2 * (\delta V)^2 + \left( \frac{\partial C_{M_{1/4c}}}{\partial S} \right)^2 * (\delta S)^2$$

$$47. \frac{\partial V}{\partial (\Delta P)} = \left( \frac{1}{2} \right) * \sqrt{\frac{2}{\Delta P * \rho}}$$

$$48. \frac{\partial V}{\partial \rho} = \left( -\frac{1}{2} \right) * \sqrt{2 \Delta P} * \rho^{-1.5}$$

$$49. \frac{\partial \rho}{\partial T} = \frac{-P}{RT^2}$$

$$50. \frac{\partial \rho}{\partial P} = \left( \frac{1}{RT} \right)$$

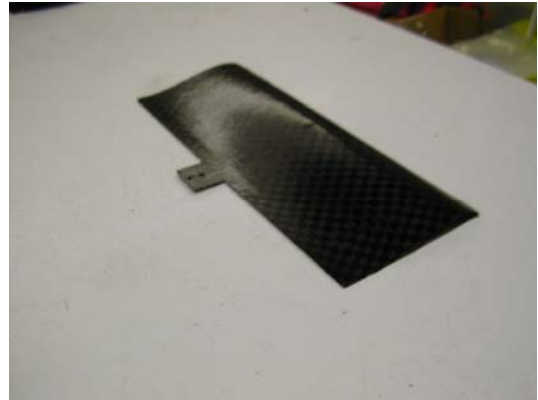
$$51. \theta_B = \frac{PL^2}{2EI}$$

APPENDIX F: Wing Pictures

Flat Plate:



Wing 2: UF Rectangular Rigid Wing



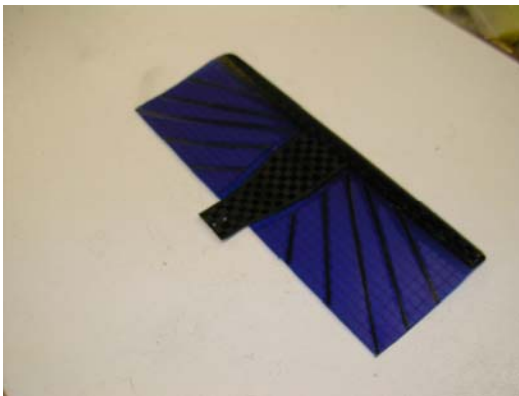
Wing 0: 8300 Rectangular Flexible Wing



Wing 3: 8300 Rectangular Rigid Wing



Wing 1: UF Rectangular Flexible Wing



Wing 4: 8300 Elliptical Flexible Wing with Winglets



Wing 5: UF Elliptical Flexible Wing with Winglets



Wing 7: 8300 Rectangular Flexible Wing with 1/8 inch thick LE



Wing 6: UF Tapered Flexible Wing with 1/8 inch thick LE



Wing 8: 8300 Elliptical Flexible Wing



Wing 9: UF Elliptical Flexible Wing



## References

- Advanced Ceramics Research, "Unmanned Vehicle Systems, Silver Fox UAV," World Wide Web, <http://www.acrtucson.com/UAV/silverfox/index.htm>, 2006
- Albertani, Roberto, et al., "The University of Florida Autonomous Micro Air Vehicle," *International Micro Air Vehicle Competition*, Gainesville, Florida, 2005
- Anderson, John D. Jr. Aircraft Performance and Design. Maryland: University of Maryland, 1999.
- Anderson, John D. Jr. Fundamentals of Aerodynamics 3<sup>rd</sup> Edition. Maryland: University of Maryland, 2001.
- Department of Mechanical and Aerospace Engineering, University of Florida, *Development of a Composite Bendable-Wing Micro Air Vehicle*. University of Florida, Gainesville Florida, 2006
- Drouin, Gedeon, and Girard, Bertrand, "A Stiff Monopiece Wind Tunnel Balance," *First International Symposium on Strain Gauge Balances*, Hampton Virginia, October 22-25, pgs. 467 - 479, 1996
- Eppler, R., "Induced Drag and Winglets," *Journal of Aerospace Science and Technology*, n° 1, 3-15, 1997
- Ferguson, Lauren A., *A Computational Model for Flexible Wing Based Micro Air Vehicles*, S. M. Thesis, Department of Mathematics, Texas Tech University, Lubbock, TX, USA, 2006
- Gatlin, Gregory M., and McGrath, Brian E., "Low-Speed Longitudinal Aerodynamic Characteristics Through Poststall for Twenty-One Novel Planform Shapes,"

- Technical Report, NASA Langley Research Center, TR – 3503, Hampton, VA, 1995
- General Atomics Aeronautical Systems, “Predator B UAV,” World Wide Web, [http://www.ga-asi.com/products/predator\\_b.php](http://www.ga-asi.com/products/predator_b.php), 2008
- Gere, James M. Mechanics of Materials 5<sup>th</sup> Edition. California: Stanford University, 2001.
- Grasmeyer, Joel M., and Keennon, Matthew T, *Development of the Black Widow Micro Air Vehicle*. AeroVironment, Inc. Simi Valley, California, 2001
- Holt, Ashley. Engineering Analysis of Flight Mechanics. California: Stanford University, 1972.
- Ifju, Peter G., et al., *Flexible-Wing-Based Micro Air Vehicles*, University of Florida, Gainesville, Florida, 2002
- Jacobs, Eastman N., and Sherman, Albert, “Airfoil Section Characteristics as Affected by Variations of the Reynolds Number,” NACA Technical Report, Langley Memorial Aeronautical Laboratory, TR – 586, Hampton, VA, 1939
- Lian, Yongsheng, et al., “Membrane wing aerodynamics for micro air vehicles,” *Progress in Aerospace Sciences*, Vol. 39, 425-465, 2003
- Mathworks Inc., “Matlab, the Language of Technical Computing,” Matlab Version 7.0.4, 2005
- Morris, Dr. Stephen J., and Holden, Dr. Michael, *Design of Micro Air Vehicles and Flight Test Validation*. MLB Company. Palo Alto, California, 2000
- Morris, Dr. Stephen J., *Miniature Spy Planes: The Next Generation of Flying Robots*. MLB Company. Palo Alto, California, 2002

- Mueller, Thomas J., “Aerodynamic Measurements at Low Reynolds Numbers for Fixed Wing Micro-Air Vehicles,” to be presented at the VKI Special Course on *Development and Operation of UAVs for Military and Civil Applications*, VKI, Belgium, September 13-17, 1999
- Mueller, Thomas J., and DeLaurier, James D., “Aerodynamics of Small Vehicles,” *Annual Review of Fluid Mechanics*, Vol. 35, 89-111, 2003
- Nechyba, Michael, and Ifju, Dr. Peter, “Towards Autonomous Flight for Micro Air Vehicles: Vision-Guided Flight Stability and Control,” *Power Point Presentation for University of Florida*, Gainesville, Florida, 2002
- Null, W., and Shkarayev S., “Effect of Camber on the Aerodynamics of Adaptive-Wing Micro Air Vehicles,” *Journal of Aircraft*, Vol. 42, No. 6, 1537-1542, Nov.-Dec. 2005
- Olson, D. H., et al, *Wind Tunnel Testing and Design of Fixed and Flapping Wing Micro Air Vehicle at the University of Arizona*. University of Arizona, Tuscan Arizona, 2005
- Pelletier, Alain, and Mueller, Thomas J., “Low Reynolds Number Aerodynamics of Low-Aspect-Ratio, Thin/Flat/Cambered-Plate Wings,” *Journal of Aircraft*, Vol. 37, No. 5, September – October Edition, 825-832, 2000
- Pornsirak, T. Nick, et al., *Microbat: A Palm-Sized Electrically Powered Ornithopter*, California Institute of Technology, Pasadena, California, 1999
- Pratt, William K. Digital Image Processing 3<sup>rd</sup> Edition. California: Los Altos, 2001.
- Rae, William H. Jr., and Alan Pope. Low-Speed Wind Tunnel Testing. Washington: Seattle, 1984.

- Rist, Ulrich, Maucher, Ulrich, and Wagner, Siegfried, *Direct Numerical Simulation of Some Fundamental Problems Related to Transition in Laminar Separation Bubbles*, Stuttgart, Germany, 1996
- Savage, M. G., and Larose, G. L., "An experimental study of the aerodynamic influence of a pair of winglets on a flat plate model," *Journal of Wind Engineering and Industrial Aerodynamics*, Vol. 91, 113-126, 2003
- Torres, Gabriel, and Mueller, Thomas J., *Micro Aerial Vehicle Development: Design, Components, Fabrication, and Flight-Testing*. University of Notre Dame, IN, 2000
- Viieru, Dragos, et al., *Investigation of Tip Vortex on Aerodynamic Performance of a Micro Air Vehicle*, University of Florida, Gainesville, Florida, 2003
- Waszak, Martin R., Jenkins, Luther N., and Ifju, Dr. Peter, "Stability and Control Properties of an Aeroelastic Fixed Wing Micro Aerial Vehicle," *AIAA Atmospheric Flight Mechanics Conference*, Montreal, Canada, August 6-9, 2001